Titre: Title:	Electromagnetics of Uniform-Velocity Space-Time Structures
Auteur: Author:	Zoé-Lise Deck-Léger
Date:	2024
Type:	Mémoire ou thèse / Dissertation or Thesis
Référence: Citation:	Deck-Léger, Z.-L. (2024). Electromagnetics of Uniform-Velocity Space-Time Structures [Thèse de doctorat, Polytechnique Montréal]. PolyPublie. https://publications.polymtl.ca/58015/

URL de PolyPublie: PolyPublie URL:	https://publications.polymtl.ca/58015/
Directeurs de recherche: Advisors:	Denis Seletskiy, & Christophe Caloz
Programme: Program:	génie électrique

POLYTECHNIQUE MONTRÉAL
affiliée à l'Université de Montréal

Electromagnetics of Uniform-Velocity Space-Time Structures

ZOÉ-LISE DECK-LÉGER
Département de génie électrique

Thèse présentée en vue de l'obtention du diplôme de *Philosophiæ Doctor*
Génie électrique

Février 2024

POLYTECHNIQUE MONTRÉAL
affiliée à l'Université de Montréal

Cette thèse intitulée :

Electromagnetics of Uniform-Velocity Space-Time Structures

présentée par **Zoé-Lise DECK-LÉGER**
en vue de l'obtention du diplôme de *Philosophiæ Doctor*
a été dûment acceptée par le jury d'examen constitué de :

Ke WU, président
Denis SELETSKIY, membre et directeur de recherche
Christophe CALOZ, membre et codirecteur de recherche
Yakir HADAD, membre externe
Victor PACHECO-PEÑA, membre externe

ACKNOWLEDGEMENTS

I would first like to thank Christophe for sharing his broad knowledge with all the members of his team and thus creating a stimulating environment. I am also thankful for his availability related to all the steps in the preparation of conference presentations manuscripts, and to his attention to both the broad picture and the minute details. Finally, I thank him for his unwavering and enthusiastic encouragement and support.

I would like to thank Denis for his assistance in ensuring a smooth completion of this thesis and for the two engaging classes I took with him.

Finally I would like to thank my collegues Nima, Xiaoyi, Guillaume, Oscar, Amir and Zhiyu for all the discussions, for their consistently sound and judicious feedback, and for their enthusiasm for our research. I consider myself privileged to have been part of such an excellent team.

RÉSUMÉ

Cette thèse porte sur l'étude de la propagation et la diffraction d'ondes électromagnétiques sur des structures spatiotemporelles à vitesse constante. Les structures spatiotemporelles sont des entités dont les propriétés varient à la fois dans l'espace et dans le temps, présentant ainsi une incroyable diversité. Nous les classifions en deux catégories: les structures dont la matière, un fluide ou un dielectrique par exemple, se déplace à une vitesse constante, et les structures qui sont modulées par une onde, acoustique ou optique par exemple, se propageant à une vitesse constante.

La première catégorie de structures, celle des structures en mouvement, a été étuidée depuis plus de deux siècles, commençant par les travaux de Bradley et Doppler, qui ont décrit la déviation et le changement de fréquence de la lumière émise par des étoiles en mouvement par rapport à la Terre, ainsi que les travaux ultérieurs de Fizeau, qui a mesuré la vitesse de la lumière dans un fluide en mouvement. Puisque les milieux en mouvement altèrent les propriétés de la lumière (déviations, changements de fréquence et de vitesse), ils sont aujourd'hui étudiés dans le contexte du contrôle des ondes électromagnétiques.

La deuxième catégorie de structures, les structures modulées, a été découverte et étudiée plus récemment, notamment dans le contexte de l'amplification paramétrique et de l'ionisation des plasmas. Tout comme leurs homologues en mouvement, ces structures altèrent les propriétés de la lumière en menant à des sauts de fréquences, des déviations, et des changements de vitesse. Parce qu'elles ne sont pas en mouvement, ces structures sont plus simples à réaliser que celles en mouvement. De plus, elles ne sont pas soumises aux mêmes contraintes: leur vitesse peut dépasser celle de la lumière, et on peut les accélérer sans appliquer de force. Elle connaissent aujourd'hui un regain d'intérêt dans le contexte du contrôle des ondes électromagnétiques.

Dans ce travail, nous nous intéressons d'abord à la première catégorie de structures. En premier lieu, nous développons un diagramme d'impédance pour des milieux en mouvement uniforme. Ensuite, nous utilisons ce diagramme pour déterminer graphiquement l'impédance des ondes transmises dans un milieu en mouvement tronqué par une interface stationnaire. Pour établir un lien avec la suite the la thèse, qui aborde la deuxième catégories de structures, nous démontrons ensuite comment ces catégories sont reliées par une simple transformée de Lorentz.

Le reste de la thèse se consacre à la deuxième catégorie de structures. Nous présentons les propriétés des ondes réfléchies et transmises par une interface modulée à vitesse uniforme, puis par deux interfaces, et enfin par une structure périodique, le tout de manière analytique. Au passage, nous proposons une généralization du théorème de Stokes et nous fournissons une approximation du diagramme de bande des structures périodiques. Ensuite, nous développons une généralization de la méthode des différences finies dans le domaine temporel pour modéliser ces structures de manière numérique.

ABSTRACT

This thesis explores the scattering of electromagnetic waves from uniform-velocity spacetime structures. These structures may be moving-matter structures, like a moving fluid or dielectric, or moving-perturbation structures, which are modulated by an external wave, such as an acoustic or optical wave.

The first category of structures, moving-matter structures, have been the subject of extensive study for over two centuries. The studies began with the works of Bradley and Doppler, who investigated the deviations and the frequency changes of light emitted by moving stars, and were followed by the works of Fresnel and Fizeau, who investigated the speed of light in moving media. These works ultimately led to the development of the theory of relativity. Given that moving structures influence the propagation of electromagnetic waves through Bradley deflections, Doppler frequency shifts and Fresnel-Fizeau wave dragging, they are now studied in the context of wave control.

The second category of structures, moving-perturbation structures, was initially investigated in the context of parametric traveling-wave amplification and plasma ionization. Like their moving-matter counterparts, they offer the capability to control waves through frequency-shifting, deflections, and effective wave dragging. However, they transcend moving-matter systems as their velocity can exceed the speed of light, and they can be accelerated without the application of force. Therefore, there is a significant interest in gaining a deeper understanding of these structures for wave control.

In this thesis, we first explore the first category of structures, the moving-matter structures. We develop an impedance diagram for moving media and use it to graphically determine the impedance of the waves transmitted from a stationary interface. To establish a connection with the rest of the thesis, which covers moving-perturbation structures, we then demonstrate how these two categories are linked by a simple Lorentz transformation.

The rest of the thesis explores the second category of structures. We present the properties of waves scattered from a modulated interface, a modulated slab, and a modulated crystal. Along the way, we introduce a generalization of the Stokes theorem and provide an approximation for the band diagram of a periodic crystal. Finally, we generalize the conventional FDTD scheme to accurately handle modulated structures.

TABLE OF CONTENTS

LIST OF TABLES

LIST OF FIGURES

LIST OF APPENDICES

CHAPTER 1 INTRODUCTION

Space-time structures, in their broadest sense, encompass all structures that vary in space and time, and are therefore incredibly diverse. Here, we first classify and provide some background information on various space-time structures. We then present an overview of the thesis contents.

1.1 Classification and Background

1.1.1 Moving-matter structures

The most widely known space-time structures are undoubtedly *moving-matter structures*, which consist of matter, such as dielectrics or fluids, in motion relative to an observer. The study of the electrodynamics of these structures started with the key discoveries in the 18th and 19th centuries which are the Bradley aberration [4], the Fresnel-Fizeau drag [5, 6] and the Doppler effect [7, 8]. These findings led to Einstein's formulation of the theory of special relativity [9, 10], and Minkowksi's formulation of the constitutive relations of moving dielectrics [11, 12]. Temporally dispersive moving structures exhibit enhanced Fizeau drag, as predicted by Lorentz [13] and confirmed experimentally by Zeeman [14].

Based on the theory of relativity, canonical problems related to scattering from *uniform-velocity* dielectric interfaces or half-spaces were shown to lead to deflections, frequency shifts, and amplification [15–17]. More recently, additional effects such as modified Goos-Hänchen shifts [18] and negative refraction [19] have been reported. In addition, experiments with highly dispersive moving media have shown large Fizeau drags, offering applications in velocimetry [20, 21].

When dealing with structures that exhibit *nonuniform-velocity*, the principles of special relativity are no longer adequate, and the broader theory of general relativity must be used [22, 23]. As moving matter induces wave "drag" through the Fresnel-Fizeau effect, nonuniform velocities can result in very exotic wave trajectories. The formulation of wave propagation in such structures is provided in [24].

1.1.2 Moving-perturbation structures

Moving-perturbation structures involve a perturbation in motion relative to an observer. This perturbation results in the modulation of a parameter of the structure, for instance the refractive index, n, without any net transfer of matter. We categorize modulated structures into three classes, ranging from the most specific–purely temporal modulations– to the most general, nonuniform-velocity modulations.

Purely temporal modulations

When the modulation is purely temporal, the structure as a whole only varies in time, i.e. $n(\mathbf{r}, t) = n(t)$. The canonical problem of the scattering from a pure temporal step was solved in 1958 [25]. One of the striking effects of time interfaces is the generation of a time reversed wave, as was beautifully shown in an acoustic experiment in [26]. By replacing a sharp time step with a more temporal gradient, different wave profiles are observed [27], and these gradients may be synthesized for various filtering responses, similarly to the synthesis of purely spatial profiles [28].

A periodic succession of purely temporal steps is referred to as a time crystal (which are not to be confused with the time crystals of Wilczek [29], which are a spontaneous oscillation in time in the absence of external modulation). Time crystals exhibit momentum bandgaps, in contrast to the frequency bandgaps found in photonic crystals, and they involve bandgap amplification [30–32] rather than the bandgap reflection of photonic crystals [33].

Uniform-velocity structures

Another category of modulated structures is that of uniform-velocity structures, where $n(\mathbf{r}, t) = n(\mathbf{r} - \mathbf{v}t)$. We distinguish three velocity regimes: the subluminal ($v < c/n$), the interluminal ($v \approx c/n$), and the superluminal ($v > c/n$) regimes. A more rigorous classification will be provided in Chs. 2 and 3.

For *subluminal* velocities, canonical problems related to the scattering from polarization fronts [34] and ionization fronts [35, 36] were successfully addressed in the 1960s. These fronts lead to wave scattering akin to that from moving-matter fronts, involving Bradley-like aberration, Doppler-like frequency shifting, and wave amplification. A periodic succession of these traveling fronts forms a traveling-wave periodic structure, which exibits oblique bandgaps [37], with complex wavenumber and frequency, leading to nonreciprocity [38, 39]. In the homogenized large-wavelength regime, effective drag [3] leads to beam deflections [40].

In the *interluminal* regime, where the modulation velocity approaches the speed of light, waves theoretically experience unlimited amplification and an infinite frequency shift [41, 42] in the case of a gradient interface. However, for sharp interfaces, this problem remains unresolved, as the interface should lead to either a single scattered wave or multiple scattered waves, and the problem is thus either under- or over-determined [43]. Periodic modulations lead to traveling-wave amplification [44, 45].

In the *superluminal* velocity regime, the modulation velocity exceeds the speed of light. This is possible since no motion of matter is associated with the moving front. Scattering from superluminal fronts exhibits wave reversal, similarly to time interfaces. Furthermore, superluminal crystals lead to oblique bandgaps [46], with complex wavenumber and frequency. In the limit where $v \to \infty$, we retrieve a temporal structure. We shall see in this structure that superluminal structures can be analyzed in a frame where they appear to be purely temporal [47].

In the presence of dispersion, additional effects emerge, such as space-time focusing [48], the generation of additional scattered waves [49], and wave freezing [50].

Nonuniform-velocity structures

Finally, some nonuniform-velocity structures include standing-wave spacetime crystals [51,52] (as opposed to the traveling-wave periodic structures described above), accelerating walls [53, 54], cavities made of accelerating walls [55], all of which lead to a host of effects not encountered in uniform-velocity structures.

1.2 Thesis Contents

The goal of this thesis is to explore wave scattering and propagation in space-time structures. The next four Chapters (Ch. 2-5) each contain a peer-reviewed paper.

In Ch. 2, the paper *Electromagnetic Wave Scattering from a Moving Medium with Stationary Interface across the Interluminal Regime* presents the scattering from a bulk moving medium bounded by a stationary interface. In it, we revisit the electromagnetic formulation of wave propagation in moving media, and we develop, in parallel to the well-known isofrequency diagrams, equally useful impedance diagrams. We then proceed to solve the scattering from a stationary interface bounding such a moving medium. This is the only work on moving structures, and a connection with spacetime-modulated structures is provided (Sec. 2.8).

In Ch. 3, the paper *Uniform-Velocity Spacetime Crystals* methodically examines the scattering from spacetime crystals, by first examining the scattering from a single modulated interface, then a slab, and finally a periodic structure, or crystal. All the tools and methods, both mathematical and graphical, are provided in the introduction, such that this paper is completely self-contained. Spanning 55 pages, it represents a major portion of this thesis and includes many contributions throughout.

Chapter 4 consists of the letter *Orthogonal Analysis of Space-Time Crystals*, which solves space-time crystals in an alternative manner to that of Sec. 3.5, and hence can be seen as an addendum to Ch. 3. This alternative, orthogonal method leads to a symmetric, more insightful description of these crystals.

Chapter 5 contains the paper *Generalized FDTD Scheme for the Simulation of Electromagnetic Scattering in Moving Structures*. It presents an FDTD scheme that naturally enforces the correct boundary conditions at a moving interface, and thus provides a previously unavailable numerical tool to solve the structures presented in Chs. 3 and 4.

Finally, Ch. 6 presents some future directions.

CHAPTER 2 ARTICLE 1: ELECTROMAGNETIC WAVE SCATTERING FROM A MOVING MEDIUM WITH STATIONARY INTERFACE ACROSS THE INTERLUMINAL REGIME

Zoé-Lise Deck-Léger, Xuezhi Zheng and Christophe Caloz

Published in Photonics, Volume 8, Number 202, June 5, 2021

Abstract

This paper extends current knowledge on electromagnetic wave scattering from bounded moving media in several regards. First, it complements the usual dispersion relation of moving media, $\omega(\theta_{\mathbf{k}})$ ($\theta_{\mathbf{k}}$: phase velocity direction, associated with the wave vector, $\mathbf{k}$), with the equally important impedance relation, $\eta(\theta_{\mathbf{S}})$ ($\theta_{\mathbf{S}}$: group velocity direction, associated with the Poynting vector, $\mathbf{S}$). Second, it explains the interluminal-regime phenomenon of double-downstream wave transmission across a stationary interface between a regular medium and the moving medium, assuming motion perpendicular to the interface, and shows that the related waves are symmetric in terms of the energy refraction angle, while being asymmetric in terms of the phase refraction angle, with one of the waves subject to negative refraction, and shows that the wave impedances of the two transmitted waves are equal. Third, it generalizes the problem to the case where the medium moves obliquely with respect to the interface. Finally, it highlights the connection between this problem and a spacetime modulated medium.

2.1 Introduction

The problem of light radiation and scattering from moving media has been abundantly studied. The first studies pertained to radiation from stars and led to the discoveries of related frequency shifts by Doppler [7] and velocity aberrations by Bradley [4]. Then Einstein generalized the Doppler-shift, Bradely-aberration and Fresnel-reflection formulas to relativistic velocities [9]. Next Minkowski, leveraging the tools of relativity, derived electromagnetic equations describing light scattering phenomena observed in moving media, in particular the transformation of isotropic media, such as simple dielectrics, into 'bianisotropic' media [56] when set into motion [11]. Upon this basis, many investigations on scattering in and from moving dielectrics have been reported since the early twentieth century, e.g., [57–59].

The vast majority of the research on moving media has concerned objects that move as a whole, with their edges co-moving with the medium. But moving media can also be bounded by stationary interfaces. Such a situation is very common when the motion is parallel to the interfaces, as is the case for instance of the water flow of a river parallel to its banks. Wave scattering from this type of interface involves effects such as velocity-dependent positive or negative refraction [19] and modified Goos-Hänchen shifting [18]. Less common is the situation where the motion of the medium is perpendicular to a stationary interface, such as is the case for a conveyor belt with fixed ends [60]. This type of boundary, although of even greater interest, as shall be shown, has been much less studied. The corresponding scattering coefficients were derived for the subluminal regime in [17] and the interluminal-regime phenomenon of double-wave transmission was described for the case of normal incidence in [60], but much of the related physics remains to be unveiled.

Here, we extend the established knowledge on moving media with stationary boundaries. We first recall the bianisotropic nature and properties of unbounded moving media. Upon this basis, we then re-derive their isofrequency relation and establish their impedance relation. We next study the properties of waves scattered from such media when bounded by stationary interfaces. Specifically, we describe the deflection angle of the phase and group velocities for the whole range of medium velocities, from $-c$ to c, and calculate the corresponding wave impedance, for medium motion perpendicular to the interface. Moreover, we graphically solve velocities and the impedance of waves scattered at the interface when the medium motion is at an oblique angle with respect to the interface and show that this configuration can involve negative refraction. Finally, we provide a connection between the studied moving medium problem and the related problem of a spacetime-modulated medium.

2.2 Description of the Problem

Figure 2.1 depicts the problem of interest, namely the scattering of electromagnetic waves at a stationary interface between a simple stationary medium, such as air or a simple dielectric, and a moving medium. The moving medium is here assumed to be a fluid flowing at a uniform velocity through a double-bend structure, so that the interfaces at the the bends are stationary with the medium moving perpendicularly to them. Electromagnetic waves are obliquely incident at the interface formed by one of the bends, refract into the moving fluid, and exit the fluid at the other interface. The setup of Fig. 1 is inspired by the Fizeau experiment [6][1], but it is to be mostly considered as a thought experiment insofar as the

[1] In this experiment, Fizeau measured the speed of light in moving fluid and hence confirmed the 1818 prediction of Fresnel [5] that light was dragged by a moving medium. In contrast to the case of Fig. 1, his experiment, using circular hoses as opposed to elongated containers (as here) to support the fluid, was restricted to normal incidence and ignored the effect of scattering at the interface between the incoming-wave

some of the fluid velocities of interest would be difficult to attain in practice.

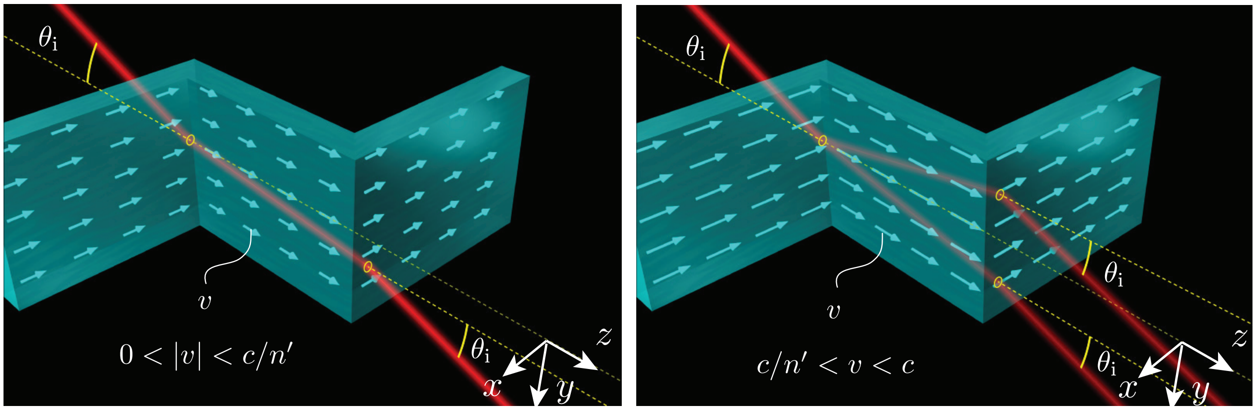

(a) (b)

Figure 2.1 Wave scattering at a stationary interface between a simple (isotropic, dispersionless and linear) medium, such as air or a standard dielectric fluid, and a moving medium with uniform motion of velocity v perpendicular to the interface and rest refractive index (refractive index if the medium were at rest) n'. (a) Subluminal regime ($|v| \leq c/n'$). (b) Interluminal regime ($|v| \geq c/n'$).

The medium is assumed to be moving at the constant and uniform velocity v with respect to the laboratory frame, and we use the relativity convention of the unprimed and primed variables to denote quantities that are measured in the laboratory frame and in the moving-medium frame, respectively. We distinguish the following two regimes:

$$\left\{ \begin{array}{l} |v| \in [0, v'_{\mathrm{w}}] : \text{ subluminal regime} \\ |v| \in [v'_{\mathrm{w}}, c] : \text{ interluminal regime} \end{array} \right\}, \quad \text{with} \quad v'_{\mathrm{w}} = \frac{c}{n'} \tag{2.1}$$

being the wave velocity measured in the frame of the moving medium, where the fluid is at rest and has the refractive index n'. According to the definition (2.1), the subluminal regime corresponds to medium velocities that are smaller than both the wave velocity in the medium at rest (v'_{w}) and the wave velocity in free space (c), while the interluminal regime corresponds to medium velocities that are still smaller than the wave velocity in free space – the maximal velocity for matter – but larger than the wave velocity in the medium at rest[2].

Figures 2.1(a) and 2.1(b) describe the scattering phenomenology of the system in the subluminal and interluminal regimes, respectively. As will be shown in Sec. 2.6, a single wave

air region and the fluid medium.

[2]In the case of a moving charged particle, as opposed to that of a moving medium considered here, the interluminal regime corresponds to the Cherenkov regime, where the particle radiates energy because it moves faster than the wave velocity in the medium (e.g., heavy water) [61, 62].

is transmitted in the moving medium in the subluminal regime, while two waves, with symmetric group velocities, are transmitted in the moving medium in the interluminal regime.

2.3 Moving-Medium Bianisotropy

Assuming time-harmonic plane waves of the form

$$\mathbf{A} = \mathbf{A}_0 e^{i(\mathbf{k}\cdot\mathbf{r}-\omega t)}, \tag{2.2}$$

where $\mathbf{A} = \mathbf{E}$, $\mathbf{H}$, $\mathbf{D}$, $\mathbf{B}$ are the usual electromagnetic fields, and $\mathbf{k}$ and ω are the spatial frequency (or wave vector) and temporal frequency, respectively, the Maxwell equations in a source-free region of space take the form

$$\mathbf{k}\times\mathbf{E}_0 = \omega\mathbf{B}_0, \quad \mathbf{k}\times\mathbf{H}_0 = -\omega\mathbf{D}_0, \quad \mathbf{k}\cdot\mathbf{B}_0 = 0, \quad \mathbf{k}\cdot\mathbf{D}_0 = 0. \tag{2.3}$$

In the frame of the moving medium, the constitutive relations are

$$\mathbf{D}_0' = \epsilon'\mathbf{E}_0', \qquad \mathbf{B}_0' = \mu'\mathbf{H}_0', \tag{2.4}$$

where ϵ' and μ' are scalar constants under the assumption that the medium at rest is isotropic, dispersionless and linear. The corresponding relations in the frame of the laboratory are found by applying the Lorentz transformations [63] to the fields in (2.4) and rearranging the result so as to express $\mathbf{D}$ and $\mathbf{B}$ in terms of $\mathbf{E}$ and $\mathbf{H}$. This leads to the bianisotropic constitutive relations [56, 64]

$$\mathbf{D}_0 = \bar{\bar{\epsilon}}\cdot\mathbf{E}_0 + \bar{\bar{\xi}}\cdot\mathbf{H}_0, \tag{2.5a}$$

$$\mathbf{B}_0 = \bar{\bar{\mu}}\cdot\mathbf{H}_0 + \bar{\bar{\zeta}}\cdot\mathbf{E}_0, \tag{2.5b}$$

where

$$\bar{\bar{\epsilon}} = \epsilon'\begin{bmatrix}\alpha & 0 & 0\\ 0 & \alpha & 0\\ 0 & 0 & 1\end{bmatrix}, \quad \bar{\bar{\mu}} = \mu'\begin{bmatrix}\alpha & 0 & 0\\ 0 & \alpha & 0\\ 0 & 0 & 1\end{bmatrix}, \quad \bar{\bar{\xi}} = \begin{bmatrix}0 & \chi/c & 0\\ -\chi/c & 0 & 0\\ 0 & 0 & 0\end{bmatrix}, \quad \bar{\bar{\zeta}} = \bar{\bar{\xi}}^T, \tag{2.6a}$$

with

$$\alpha = \frac{1-\beta^2}{1-\beta^2 n'^2}, \qquad \chi = \beta\frac{1-n'^2}{1-\beta^2 n'^2}, \tag{2.6b}$$

where $\beta = v/c$. In these relations, the signs of α and χ are opposite in the subluminal and the interluminal regime. This change in sign leads to drastically different physics in the two regimes, as we shall see. The parameters α and χ are relativistic (v/c-dependent), with χ being in addition time-reversal asymmetric, i.e., $\chi(-v) = -\chi(v)$, and thus inducing nonreciprocity, also manifested by the violation of the reciprocity condition $\overline{\overline{\zeta}} = -\overline{\overline{\xi}}^T$ [64,65].

According to the last two equations in (2.3), we have $\mathbf{k} \perp \mathbf{D}_0$ and $\mathbf{k} \perp \mathbf{B}_0$, so that $\mathbf{k} \| (\mathbf{D}_0 \times \mathbf{B}_0)$. In contrast, $\mathbf{E}_0$ and $\mathbf{H}_0$ are generally not parallel to $\mathbf{D}_0$ and $\mathbf{B}_0$, respectively, and therefore $\mathbf{S}_0 = \mathbf{E}_0 \times \mathbf{H}_0$ is not parallel to $\mathbf{k}$, in a bianisotropic medium. The angle of $\mathbf{k}$ with respect to the direction of motion, or the phase angle, is defined as $\theta_\mathbf{k} = \arctan(k_x/k_z)$, while the angle of $\mathbf{S}_0$ with respect to the direction of motion, or the energy angle, must be computed separately for the p- and s-polarizations.

Applying the identity $\mathbf{k} \times \mathbf{A} = \overline{\overline{\mathbf{k}}} \cdot \mathbf{A}$ with

$$\overline{\overline{\mathbf{k}}} = \begin{bmatrix} 0 & -k_z & k_y \\ k_z & 0 & -k_x \\ -k_y & k_x & 0 \end{bmatrix}, \tag{2.7}$$

to the first two equations in (2.3) and substituting the constitutive relations (2.5) in the resulting equations leads to the dyadic relations

$$\overline{\overline{\mathbf{k}}} \cdot \mathbf{E_0} = \omega \left(\overline{\overline{\mu}} \cdot \mathbf{H}_0 + \overline{\overline{\zeta}} \cdot \mathbf{E}_0 \right), \quad \overline{\overline{\mathbf{k}}} \cdot \mathbf{H}_0 = -\omega \left(\overline{\overline{\epsilon}} \cdot \mathbf{E}_0 + \overline{\overline{\xi}} \cdot \mathbf{H}_0 \right), \tag{2.8}$$

and solving these equations for $\mathbf{H}_0$ and $\mathbf{E}_0$ yields

$$\mathbf{H}_0 = \frac{1}{\omega} \overline{\overline{\mu}}^{-1} \cdot \left(\overline{\overline{\mathbf{k}}} - \omega \overline{\overline{\zeta}} \right) \cdot \mathbf{E}_0, \quad \mathbf{E}_0 = -\frac{1}{\omega} \overline{\overline{\epsilon}}^{-1} \cdot \left(\overline{\overline{\mathbf{k}}} + \omega \overline{\overline{\xi}} \right) \cdot \mathbf{H}_0. \tag{2.9}$$

Assuming then, without loss of generality, that scattering occurs in the xz-plane, so that $k_y = 0$ in (2.7), these relations become, upon substitution of the so-reduced tensor $\overline{\overline{\mathbf{k}}}$ and of the constitutive tensors in (2.6),

$$\mathbf{H}_0 = \frac{1}{\omega \mu' \alpha} \begin{bmatrix} 0 & -(k_z - \omega\chi/c) & 0 \\ k_z - \omega\chi/c & 0 & -k_x \\ 0 & \alpha k_x & 0 \end{bmatrix} \mathbf{E}_0 \tag{2.10a}$$

$$\mathbf{E}_0 = -\frac{1}{\omega \epsilon' \alpha} \begin{bmatrix} 0 & -(k_z - \omega\chi/c) & 0 \\ k_z - \omega\chi/c & 0 & -k_x \\ 0 & \alpha k_x & 0 \end{bmatrix} \mathbf{H}_0. \tag{2.10b}$$

Since the medium is achiral, according to the expression of $\overline{\overline{\xi}}$ in (5.6), it does not induce any polarization rotation [66, 67], and the problem decouples therefore into p- and s-polarized waves. For p-polarized waves, we have $\mathbf{H}_0 = H_{0y}\hat{\mathbf{y}}$, and we find from (2.10b) the $\mathbf{E}_0$ field components

$$E_{0x} = \frac{k_z - \omega\chi/c}{\omega\epsilon'\alpha} H_{0y}, \quad E_{0z} = -\frac{k_x}{\omega\epsilon'} H_{0y}. \tag{2.11a}$$

For later use, we also note from (2.10a) that

$$H_{0y} = \frac{1}{\omega\mu'\alpha}\left[(k_z - \omega\chi/c)\, E_{0x} - k_x E_{0z}\right]. \tag{2.11b}$$

Inserting relations (2.11a) into the expression of the Poynting vector $\mathbf{S}_0 = -(E_{0z}\hat{\mathbf{x}} - E_{0x}\hat{\mathbf{z}})H_{0y}$ yields then the angle of this vector with respect to the medium motion direction (z) as

$$\theta_{\mathbf{S}} = \arctan\left(\frac{-E_{0z}}{E_{0x}}\right) = \arctan\left(\frac{\alpha k_x}{k_z - \omega\chi/c}\right). \tag{2.12}$$

For s-polarized waves, we have $\mathbf{E}_0 = E_{0y}\hat{\mathbf{y}}$, and we find from (2.10a) the $\mathbf{H}_0$ components

$$H_{0x} = -\frac{k_z - \omega\chi/c}{\omega\mu'\alpha} E_{0y}, \quad H_{0z} = \frac{k_x}{\omega\mu'} E_{0y}, \tag{2.13a}$$

and, again for later use, we note from (2.10b) that

$$E_{0y} = \frac{-1}{\omega\epsilon'\alpha}\left[(k_z - \omega\chi/c)\, H_{0x} - k_x H_{0z}\right]. \tag{2.13b}$$

Inserting relations (2.13a) into the expression of the Poynting vector, which is now $\mathbf{S}_0 = (H_{0z}\hat{\mathbf{x}} - H_{0x}\hat{\mathbf{z}})E_{0y}$, yields then the same Poynting angle as that of the p-polarized wave, given by the second equality of (2.12).

Figure 2.2 shows the vector configurations for two wave polarizations. For the p-polarization, there is a splitting of the $\mathbf{D}_0$ and $\mathbf{E}_0$ fields, while for the s-polarization, the splitting is between the $\mathbf{B}_0$ and $\mathbf{H}_0$ fields.

2.4 Dispersion Relation and Isofrequency Diagram

The dispersion relation is obtained by eliminating the field quantities in the set of equations (2.10) (inserting (2.10b) into (2.10a)), and setting the determinant of the resulting system to zero, which yields [64]

$$\left(k_z - \frac{\omega}{c}\chi\right)^2 + \alpha k_x^2 = \left(\alpha n'\frac{\omega}{c}\right)^2. \tag{2.14}$$

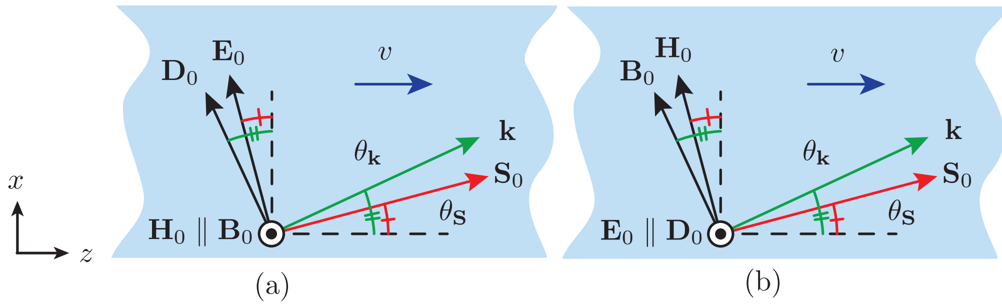

Figure 2.2 Electromagnetic vector configurations in the moving medium. (a) p-polarization. (b) s-polarization.

This may alternatively be written in polar form, upon substituting $k_z = k\cos\theta_\mathbf{k}$ and $k_x = k\sin\theta_\mathbf{k}$ with $k = \sqrt{k_z^2 + k_x^2} = n(\theta_\mathbf{k})\omega/c$ in this relation, as

$$\left(n(\theta_\mathbf{k})\cos\theta_\mathbf{k} - \chi\right)^2 + \alpha\left(n(\theta_\mathbf{k})\sin\theta_\mathbf{k}\right)^2 = \left(\alpha n'\right)^2, \tag{2.15}$$

where n, the refractive index of the medium as seen in the laboratory frame, is a function of $\theta_\mathbf{k}$ and should not be confused with n', the refractive index seen in the moving frame. The independence of the refractive index from ω in (2.15) indicates that the medium remains temporally nondispersive ($n \neq n(\omega)$) when it is set in motion. In contrast, the dependence of the refractive index on the propagation angle ($n = n(\theta_\mathbf{k})$) indicates that the velocity of the medium induces anisotropy. This is due to the drag of the medium on the wave. The anisotropy is elliptical for $\alpha > 0$ (subluminal regime) or hyperbolic for $\alpha < 0$ (interluminal regime), and the relation is off-centered, with the center at $(k_z, k_x) = (\chi\omega/c, 0)$[3].

We then compute, from the dispersion relation (2.14), the phase and group velocities. The phase velocity vector $\mathbf{v}_\mathrm{p}$ is found by solving $n(\theta_\mathbf{k})$ in (2.14), which yields [68]

$$\mathbf{v}_\mathrm{p} = \frac{c}{n(\theta_\mathbf{k})}\hat{\mathbf{k}} = \frac{c\left(\cos^2\theta_\mathbf{k} + \alpha\sin^2\theta_\mathbf{k}\right)}{\chi\cos(\theta_\mathbf{k}) \pm \sqrt{\chi^2\cos^2\theta_\mathbf{k} - (\cos^2\theta_\mathbf{k} + \alpha\sin^2\theta_\mathbf{k})(\chi^2 - \alpha^2 n'^2)}}\hat{\mathbf{k}}, \tag{2.16}$$

where $\hat{\mathbf{k}} = \mathbf{k}/k$. The phase velocity is hence directed along the radial vector $\hat{\mathbf{k}}$, subtended by the polar angle $\theta_\mathbf{k}$. The group velocity vector is found by differentiating (2.14) with respect to k_x and k_z, and grouping the two results, which leads to [68]

$$\mathbf{v}_\mathrm{g} = \nabla_\mathbf{k}\omega(\mathbf{k}) = \frac{\alpha k_x\hat{\mathbf{x}} + (k_z - \omega\chi/c)\hat{\mathbf{z}}}{\omega(\alpha^2 n'^2/c^2) + \chi/c(k_z - \omega\chi/c)}. \tag{2.17}$$

[3]The rest-medium relations are retrieved by setting $v = 0$. We obtain then $\alpha = 1$ and $\chi = 0$ from (2.6b), and hence circular refractive index curves with radius $n'\omega/c$.

It can be shown that the phase velocity does not correspond to the velocity addition rule derived by Einstein, whereas the group velocity does [69].

The angles for the the phase and group velocities are found from the phase and group velocity expressions (2.16) and (2.17) as

$$\theta_{\mathbf{k}} = \arctan\left(\frac{k_x}{k_z}\right), \tag{2.18a}$$

$$\theta_{\mathbf{S}} = \arctan\left(\frac{\alpha k_x}{k_z - \omega\chi/c}\right). \tag{2.18b}$$

The group velocity vector $\mathbf{v}_{\mathrm{g}}$, as a gradient, is perpendicular to the frequency contour curves $\omega(k_z, k_x)$ evaluated at a given frequency $\omega = \omega_0$. The Poynting vector is also perpendicular to the contour curves [64], and thus the vectors $\mathbf{v}_{\mathrm{g}}$ and $\mathbf{S}$ share the same polar angle, $\theta_{\mathbf{S}}$. For the specific case of moving media, this is verified by comparing the second equation of (2.18) with the angle of the Poynting vector calculated in (2.12).

Figure 2.3 plots the dispersion relations (2.14), with $\bar{k}_{x,z} = k_{x,z}/k_0$, and the phase and group velocity vectors (2.16) and (2.17). Figure 2.3(a) corresponds to the subluminal regime and Fig. 2.3(b) corresponds to the interluminal regime. In the subluminal regime (Fig. 2.3(a)),

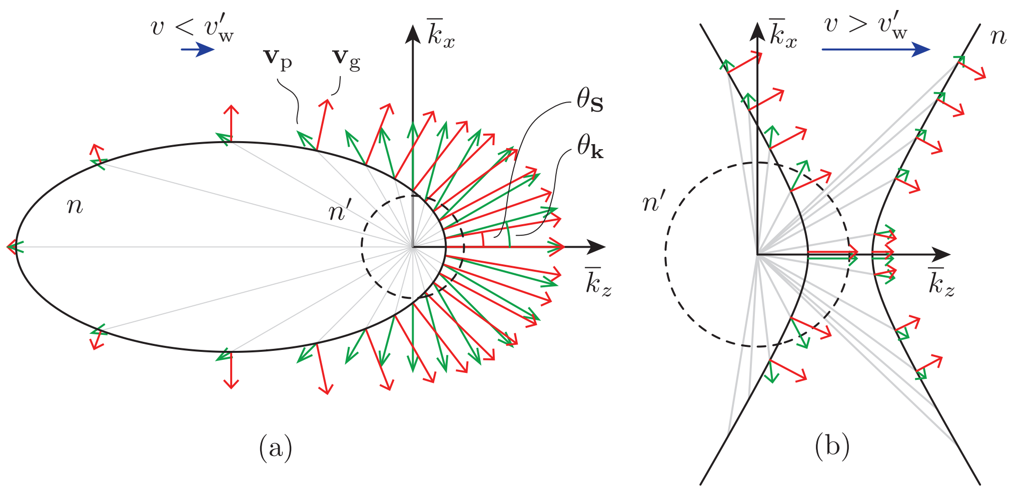

Figure 2.3 Dispersion relation, with phase and group velocity vectors for a moving dielectric (fluid) medium with refractive index $n' = 2$ (wave velocity in the rest medium: $v'_{\mathrm{w}} = c/2$). (a) Subluminal regime, with velocity $v = 0.9v'_{\mathrm{w}} < v'_{\mathrm{w}}$. (b) Interluminal regime, with $v = 1.6v'_{\mathrm{w}} > v'_{\mathrm{w}}$. The dashed circles correspond to the isotropic curves at $v = 0$.

the velocity is less for purely upstream propagation, $\theta_{\mathbf{k}} = \pi$, than for purely downstream propagation, $\theta_{\mathbf{k}} = 0$[4]. When the phase velocity is perpendicular to the motion, the group

[4]The exact wave velocity for propagation parallel to the motion was found by Einstein as $v_{\mathrm{w}} = [(c/n') \pm$

velocity is deflected by the stream, a result of the drag. In the interluminal regime (Fig 2.3(b)) there is no purely upstream solution (no solution for $\theta_{\mathbf{k}} = \pi$) but two purely downstream solutions ($\theta_{\mathbf{k}} = 0$) with different but aligned velocities. In the asymptotic limit $\bar{k}_z, \bar{k}_x \to \infty$, the hyperbola (2.14) degenerates into the straight lines $\bar{k}_x = \pm(\bar{k}_z - \chi)/\sqrt{|\alpha|}$. In this limit the group velocity angle is maximal. Its slope is $\pm\sqrt{|\alpha|}$, since it is perpendicular to the asymptote, and therefore wave propagation is restricted to the angular sector delimited by the angles $\theta_{\mathbf{S}} = \arctan(\pm\sqrt{|\alpha|})$.

2.5 Impedance Relation and Diagram

In contrast to the dispersion relation, the impedance relation depends on the polarization of the wave, as does the Poynting vector.

For the p-polarization, the impedance relation is obtained by substituting (2.11a) into (2.11b), so as to eliminate the wavevector quantities. This yields

$$\frac{E_{0x}^2}{H_{0y}^2} + \frac{1}{\alpha}\frac{E_{0z}^2}{H_{0y}^2} = \frac{\mu'}{\epsilon'}. \tag{2.19a}$$

This relation may be rewritten in terms of the wave impedance components $\eta_{\mathrm{p}z} = E_{0x}/H_{0y}$, $\eta_{\mathrm{p}x} = -E_{0z}/H_{0y}$ and $\eta' = |\mathbf{E}_0'|/|\mathbf{H}_0'| = \sqrt{\mu'/\epsilon'}$ as

$$\alpha\eta_{\mathrm{p}z}^2 + \eta_{\mathrm{p}x}^2 = \alpha\eta'^2, \tag{2.19b}$$

or, alternatively, in polar form upon substituting $E_{0x}/H_{0y} = |\mathbf{E}_0|\cos\theta_{\mathbf{S}}/|\mathbf{H}_0|$, $E_{0z}/H_{0y} = |\mathbf{E}_0|\sin\theta_{\mathbf{S}}/|\mathbf{H}_0|$ (see geometrical decomposition in Fig. 2.2(a)), and $\eta = |\mathbf{E}_0|/|\mathbf{H}_0|$ in (2.19a), as

$$\eta_{\mathrm{p}}^2\left(\alpha\cos^2\theta_{\mathbf{S}} + \sin^2\theta_{\mathbf{S}}\right) = \eta'^2\alpha. \tag{2.19c}$$

The relevant angle for the impedance diagram, given by this relation, is thus the Poynting vector angle, whereas the relevant angle for the dispersion relation, given by (2.15), was the wave vector angle, consistently with the field configuration in Fig. 2.2(a). The relations (2.19) are the equations of an ellipse for $\alpha > 0$ (subluminal regime) and of a hyperbola for $\alpha < 0$ (interluminal regime), both centered at $(\eta_{\mathrm{p}z}, \eta_{\mathrm{p}x}) = (0, 0)$.

For the s-polarization, the impedance relation is similarly obtained from (2.13) as

$$\frac{H_{0x}^2}{E_{0y}^2} + \frac{1}{\alpha}\frac{H_{0z}^2}{E_{0y}^2} = \frac{\epsilon'}{\mu'}. \tag{2.20a}$$

$v]/[1 + (v/n')/c]$, which reduces to the Fresnel-Fizeau result when $v \ll c$, using $1/(1+x) \approx 1 - x$ for $x \ll 1$.

This relation may be best rewritten in terms of the wave admittance (as opposed to impedance), with the admittance components $\eta_{\mathrm{s}z}^{-2} = H_{0x}^2/E_{0y}^2$ and $\eta_{\mathrm{s}x}^{-2} = H_{0z}^2/E_{0y}^2$, as

$$\alpha\eta_{\mathrm{s}z}^{-2} + \eta_{\mathrm{s}x}^{-2} = \alpha\eta'^{-2}, \tag{2.20b}$$

or, in polar form, as

$$\eta_{\mathrm{s}}^{-2}\left(\alpha\cos^2\theta_{\mathbf{S}} + \sin^2\theta_{\mathbf{S}}\right) = \eta'^{-2}\alpha, \tag{2.20c}$$

which also involves the Poynting vector angle instead of the wave vector angle. The admittance relations (2.20) are the equations of an ellipse for $\alpha > 0$ (subluminal regime) and of a hyperbola for $\alpha < 0$ (interluminal regime), both centered at $(\eta_{\mathrm{s}z}^{-1}, \eta_{\mathrm{s}x}^{-1}) = (0, 0)$.

The following notes are here in order. First, the p- and s-polarization impedances, resp. given in (2.19) and (2.20), are inversely proportional to each other, specifically $\eta_{\mathrm{p}}/\eta' = \eta'/\eta_{\mathrm{s}}$. Second, their components along the direction of motion found from (2.11a) and (2.13a) as

$$\eta_{\mathrm{p}z} = \frac{E_{0x}}{H_{0y}} = \frac{k_z - \omega\chi/c}{\omega\epsilon'\alpha}, \quad \eta_{\mathrm{s}z} = \frac{E_{0y}}{H_{0x}} = -\frac{\omega\mu'\alpha}{k_z - \omega\chi/c} \tag{2.21}$$

are in agreement with the transverse impedance expression in [70, 71].

Figure 2.4 plots typical impedance diagrams. Figure 2.4(a) corresponds to the subluminal regime. The p-polarization impedance curve is an ellipse, while the s-polarization impedance curve is the inverse of an ellipse, an elliptic limaçon. The figure shows that the impedance is unaffected by motion for pure-downstream and pure-upstream propagation, i.e., $\eta_{\mathrm{s,p}}(0°) = \eta_{\mathrm{s,p}}(180°) = \eta'$ [5], while for all the other angles $\eta_{\mathrm{p}} > \eta'$ and $\eta_{\mathrm{s}} < \eta'$. Note that the p-polarization impedance $x-$ and $z-$ components are found by simple orthogonal projections, whereas the s-polarization $x-$ and $z-$ impedance components, which are mathematically expressed as $\eta_{\mathrm{s}x} = \eta_{\mathrm{s}}/\sin\theta_{\mathbf{S}}$ and $\eta_{\mathrm{s}z} = \eta_{\mathrm{s}}/\cos\theta_{\mathbf{S}}$, as seen by comparing (2.20b) to (2.20c), are not found using orthogonal projections, but are rather found as illustrated in Fig. 2.4. The opposite would be true if we had chosen an admittance representation, and the impedance/admittance representations are naturally best suited to the p/s-polarizations, but we wanted to show the two polarization impedances on the same diagram in order to compare them.

Figure 2.4(b) corresponds to the interluminal regime. The p-polarization impedance curve is now a hyperbola, and the s-polarization impedance curve is a hyperbolic limaçon. The same remarks apply: the impedances for pure-downstream and pure-upstream propagation are un-

[5] Indeed, the transverse components of the **E** and **H** fields transform the same way under Lorentz transformation and their ratio is thus invariant.

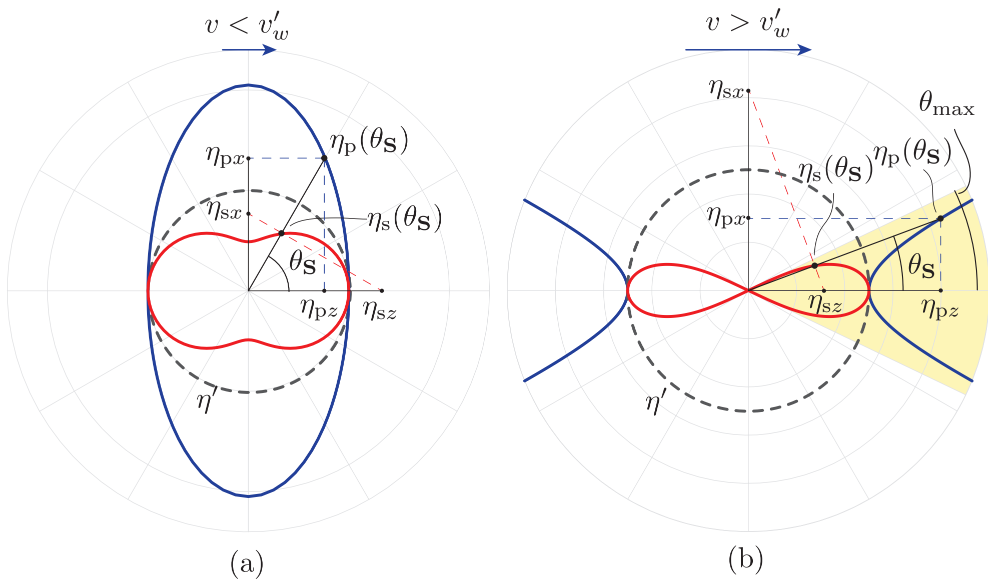

Figure 2.4 Impedance diagram [Eq. (2.19)), (2.20)] for a moving dielectric (fluid) medium with $n' = 2$ ($v'_\mathrm{w} = c/2$) and $\eta' = \eta_0/2$. The dashed circles correspond to the isotropic curves at $v = 0$. (a) Subluminal regime, with velocity $v = 0.45c < v'_\mathrm{w}$. (b) Interluminal regime, with $v = 0.8c > v'_\mathrm{w}$. The highlighted region corresponds to the region of physical solutions, with $\theta_\mathrm{max} = \arctan \pm\sqrt{|\alpha|}$.

affected by the motion, and $\eta_\mathrm{p} > \eta'$ and $\eta_\mathrm{s} < \eta'$ for all other angles . As was shown in Sec. 2.4 (Fig. 2.3(b)), the Poynting vector is restricted to the angular sector $\theta_\mathbf{S} \leq \arctan(\pm\sqrt{|\alpha|})$. Since the impedance is only meaningful in this sector, the solutions in the two left quadrants do not correspond to physical solutions.

2.6 Scattering at the Stationary Interface

We shall now study the scattering of waves at a stationary interface between free space and the moving medium (Fig. 2.1). The interface is positioned in the xy plane at $z = 0$, the medium propagates in the z direction, and hence perpendicularly to the interface, and the incident wave is in the xz-plane. Our purpose is to determine what waves are scattered across the interface and under which angles such scattering occurs in terms of both phase and group velocities.

The incident, reflected and transmitted fields, all of the form (2.2), must satisfy at the interface ($z = 0$) the spatial and temporal phase matching conditions

$$k_{x\mathrm{i}} = k_{x\mathrm{r}} = k_{x\mathrm{t}}, \tag{2.22a}$$

$$\omega_{\mathrm{i}} = \omega_{\mathrm{r}} = \omega_{\mathrm{t}}. \tag{2.22b}$$

The first equalities in these relations immediately indicate that the reflection angle must always be equal to the incidence angle, $\theta_{\mathrm{r}} = \theta_{\mathrm{i}}$, i.e., that the reflection must always be specular. To determine the transmission phase angle, $\theta_{\mathbf{k}\mathrm{t}}$, and the transmission group angle, $\theta_{\mathbf{S}\mathrm{t}}$, which are generally given by (2.18a) and (2.18b), respectively, one must first express the corresponding quantities $k_{x\mathrm{t}}$, $k_{z\mathrm{t}}$ and ω as a function of the incident wave quantities so as to satisfy the other conditions in (2.22). We have already from these relations $k_{x\mathrm{t}} = k_{x\mathrm{i}}$ and $\omega_{\mathrm{t}} = \omega_{\mathrm{i}}$. We solve then (2.14) for k_z, which yields $k_{z\mathrm{t}} = \chi\omega_{\mathrm{t}}/c \pm \sqrt{\alpha^2 {n'_2}^2 \omega_{\mathrm{t}}^2/c^2 - \alpha k_{x\mathrm{t}}^2}$, where we apply $k_{x\mathrm{t}} = k_{x\mathrm{i}}$ and $\omega_{\mathrm{t}} = \omega_{\mathrm{i}}$. Substituting these results into (2.18) finally yields the sought-after angles in terms of the angle and frequency of the incident wave

$$\theta_{\mathbf{k}\mathrm{t}}(\theta_{\mathrm{i}}, \omega_{\mathrm{i}}) = \arctan\left(\frac{k_{\mathrm{i}} \sin\theta_{\mathrm{i}}}{\chi\frac{\omega_{\mathrm{i}}}{c} \pm \sqrt{\alpha^2 {n'_2}^2 \omega_{\mathrm{i}}^2/c^2 - \alpha k_{\mathrm{i}}^2 \sin^2\theta_{\mathrm{i}}}}\right), \tag{2.23a}$$

$$\theta_{\mathbf{S}\mathrm{t}}(\theta_{\mathrm{i}}, \omega_{\mathrm{i}}) = \arctan\left(\frac{\pm\alpha k_{\mathrm{i}} \sin\theta_{\mathrm{i}}}{\sqrt{\alpha^2 {n'_2}^2 \omega_{\mathrm{i}}^2/c^2 - \alpha k_{\mathrm{i}}^2 \sin^2\theta_{\mathrm{i}}}}\right), \tag{2.23b}$$

where the dependence on the medium motion velocity (v) is embedded in the parameters α and χ, given in (2.6b).

Figure 2.5 plots the moving-medium phase and group velocities, resp. given by (2.16) and (2.17), the corresponding scattering (transmission) angles at the interface in Fig. 2.1, resp. given by (2.23a) and (2.23b), and the related rays. One distinguishes five main velocity regimes (v), corresponding to the regions labeled I to V in the figure.

Region I ($v = 0$) corresponds to the stationary regime, where wave scattering reduces the usual Snell reflection and refraction, and where $\mathbf{v}_{\mathrm{pt}} = \mathbf{v}_{\mathrm{gt}}$ since the medium is isotropic at rest.

Region II ($0 < v < c/n'_2$) corresponds to the subluminal co-directional ($\operatorname{sgn}(v) = \operatorname{sgn}(v_{\mathrm{pz}})$) regime, where the Fresnel-Fizeau drag boosts both $\mathbf{v}_{\mathrm{pt}}$ and $\mathbf{v}_{\mathrm{gt}}$ (swimmer progressing faster downstream), and where we observe a splitting between the directions of the two velocities. Only the mathematical solution branch with $v_{\mathrm{gzt}} > 0$ is physical, since the wave is launched towards positive z.

Region III ($c/n'_2 < v < 0$) corresponds to the subluminal contra-directional ($\operatorname{sgn}(v) = -\operatorname{sgn}(v_{\mathrm{pz}})$) regime, where the Fresnel-Fizeau drag effect is now negative (swimmer progressing slower upstream). Again, only the solution with positive v_{gzt} is physical, and we observe a flipping between the directions of the phase and group velocities compared to the subluminal

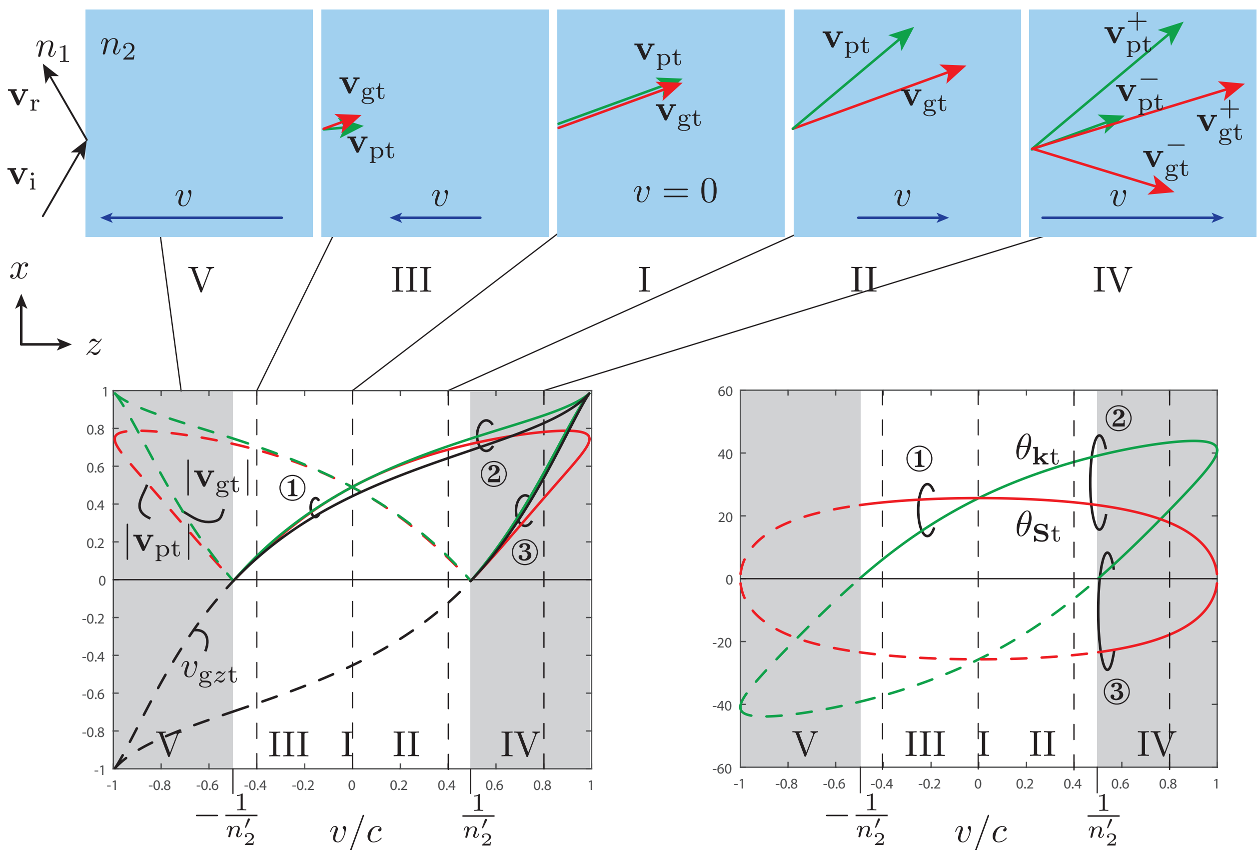

Figure 2.5 Wave scattering at the interface in Fig. 2.1 for the parameters $\theta_{\rm i} = 60°$, $n_1' = 1$, and $n_2' = 2$. Bottom-left panel: group velocity magnitude, phase velocity magnitude, and z-component of the group velocity, versus medium velocity. Bottom-right panel: group velocity and phase velocity angles versus medium velocity. The numbers ①, ② and ③ indicate the segments of physical solutions, corresponding to $v_{\rm gz} > 0$, while the dashed lines indicate nonphysical solutions. Top panels: ray configurations corresponding to the five regions indicated in the other two figures (incident and reflected rays indicated only in the left-most panel.).

co-directional case.

Region IV ($c/n_2' < v$) corresponds to the interluminal co-directional regime, where the Fresnel-Fizeau boost is, unsurprisingly, even greater than in the co-directional subluminal regime. The two mathematical solutions have a positive $v_{\rm gzt}$, and are therefore both physical. Note that the two group velocities are direction-wise symmetric but of different magnitudes while the two phase velocities differ in both direction and magnitude in this regime.

Finally, Region V ($v < -c/n_2'$) corresponds to the interluminal contra-directional regime, where no wave is transmitted into the medium, because the wave reaching the interface is pushed back by the faster contra-directional drag, consistently with the fact that $v_{\mathrm{gzt}} < 0$ for the two mathematical solution branches.

Let us now present, alternatively to the mathematical formulas used above, a graphical method that offers a quick qualitative resolution of the problem as well as physical insight into it. This graphical method includes two parts, the refractive index diagram, which was apparently introduced in [72] for stationary media and extended to modulated media in [1,47], and the impedance diagram, which is introduced here.

Figure 2.6 presents the graphical solution for the subluminal co-directional regime. The procedure is as follows: 1) plot the refractive index relations and the impedance relations for the media, i.e., $n_1(\theta_{\mathbf{k}})$ and $n_2(\theta_{\mathbf{k}})$, and $\eta_1(\theta_{\mathbf{S}})$ and $\eta_2(\theta_{\mathbf{S}})$, in corresponding diagrams; 2) locate the incident wave on the n_1 curve for the selected $\theta_{\mathbf{k}\mathrm{i}}$; 3) trace a horizontal line passing through this point, corresponding to the conservation of k_x/k_0 associated with the phase matching condition, and identify the intersections of this line with the refractive index curves; 4) at the intersection points, trace the Poynting vector angles $\theta_{\mathbf{S}\mathrm{r}}$ and $\theta_{\mathbf{S}\mathrm{t}}$ as the normal directions to the curves; 5) report these angles on the impedance diagram to locate the solutions $\eta_{\mathrm{i,r}} = \eta_1(\theta_{\mathbf{S}\mathrm{i,r}})$ and $\eta_{\mathrm{t}} = \eta_2(\theta_{\mathbf{S}\mathrm{t}})$.

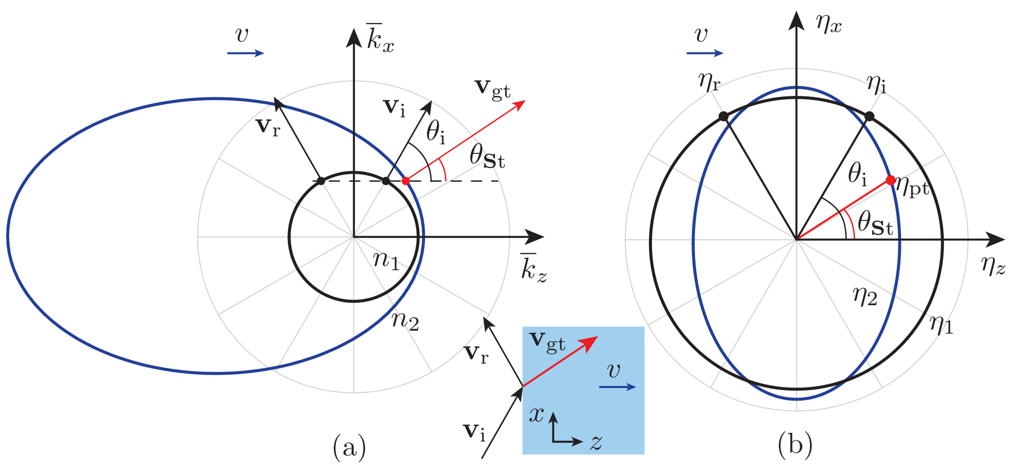

Figure 2.6 Graphical solution for the subliminal co-directional regime, for p-polarization, with $v = 0.6c$ and $\theta_{\mathrm{i}} = 60°$. (a) Refractive index diagram. Inset: scattering in space. (b) Impedance diagram.

Figure 2.7 presents the graphical solution for the interluminal co-directional regime, which follows the same procedure. From Fig. 2.7(a), we confirm that the group velocities of the two waves in the moving medium propagate symmetrically with respect to the z axis, consistently with Fig. 2.5. In Fig. 2.7(b), we report the angles found in Fig. 2.7(a) onto the impedance diagram and conclude, from the symmetry of the impedance curve, that the two transmitted waves see the same impedance, i.e., $\eta_\mathrm{t}^+ = \eta_\mathrm{t}^-$.

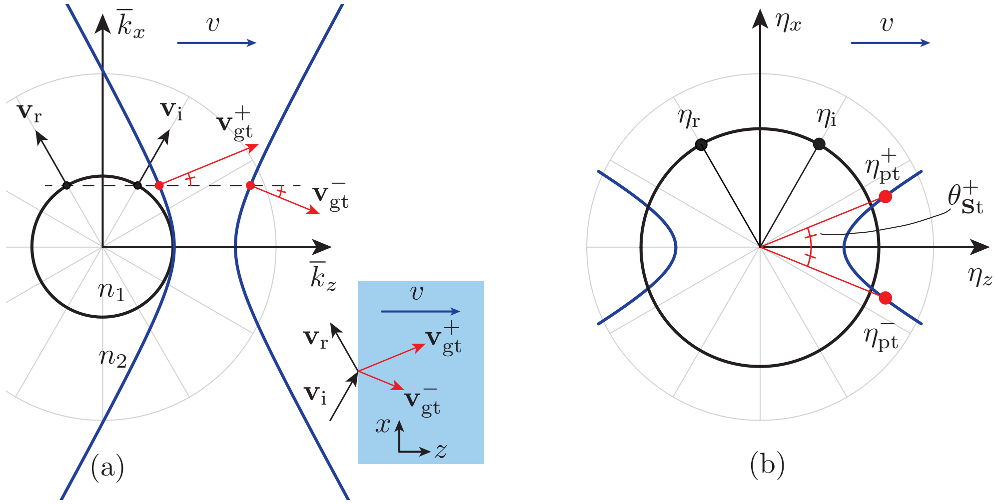

Figure 2.7 Same as Fig. 2.6, but for the interluminal regime, with $v = 0.9c$.

We have plotted the diagrams only for the p-polarization, but the same method can be applied for the s-polarization.

We have determined so far scattered waves in terms of phase and group velocity vectors. To complete the resolution of the scattering problem, we still have to determine the scattering coefficients. For the subluminal regime, the reflection and transmission coefficients are easily found by enforcing the continuity of the tangential electric and magnetic fields at the interface [17], resp. given by (2.11) and (2.13) for the p- and s-polarizations, as

$$\Gamma_\mathrm{p} = \frac{H_{y\mathrm{r}}}{H_{y\mathrm{i}}} = \frac{\eta_{\mathrm{p}z1} - \eta_{\mathrm{p}z2}}{\eta_{\mathrm{p}z1} + \eta_{\mathrm{p}z2}}, \quad T_\mathrm{p} = \frac{H_{y\mathrm{t}}}{H_{y\mathrm{i}}} = \frac{2\eta_{\mathrm{p}z1}}{\eta_{\mathrm{p}z1} + \eta_{\mathrm{p}z2}}, \tag{2.24}$$

$$\Gamma_\mathrm{s} = \frac{E_{y\mathrm{r}}}{E_{y\mathrm{i}}} = \frac{\eta_{\mathrm{s}z1}^{-1} - \eta_{\mathrm{s}z2}^{-1}}{\eta_{\mathrm{s}z1}^{-1} + \eta_{\mathrm{s}z2}^{-1}}, \quad T_\mathrm{s} = \frac{E_{y\mathrm{t}}}{E_{y\mathrm{i}}} = \frac{2\eta_{\mathrm{s}z1}^{-1}}{\eta_{\mathrm{s}z1}^{-1} + \eta_{\mathrm{s}z2}^{-1}}. \tag{2.25}$$

where the transverse impedances, defined in (2.21), can be found geometrically by performing the projections described in Sec. 2.5. In contrast, for the interluminal regime, it is not easy to calculate the scattering coefficients. We recall that either no wave (contra-directional case) or two waves (co-directional case) are transmitted, leading to either only a reflected wave or one reflected and two transmitted waves, for upstream or downstream propagation, respectively. This respectively leads to an overdetermined set of equations (one unknown and two continuity conditions) or an underdetermined one (three unknowns for 2 continuity conditions). We defer the resolution of this problem to an ulterior publication.

2.7 Generalization to Oblique Motion

So far, the medium motion was directed perpendicular to the interface. We now generalize the graphical method described in Sec. 2.6 to arbitrary angles. This corresponds to a shearing of the center portion of the apparatus of Fig. 2.1, as illustrated in Fig. 2.8.

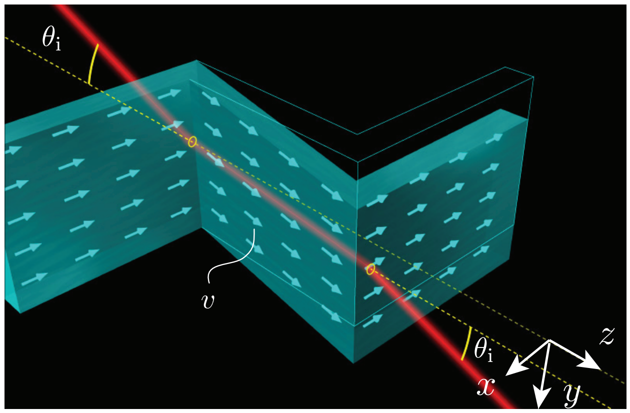

Figure 2.8 Same as Fig. 2.1, but sheared along the xz plane so as to have the medium moving at an angle with respect to the interface.

Figure 2.9 presents the graphical solution for a subluminal contra-propagating problem with velocity forming a 135 deg angle with respect to the z direction. To account for the angle of the medium velocity, the dispersion and impedance patterns of the bulk medium, with coordinates of the bulk medium, k_x'', k_z'' and η_x'', η_z'', where the double primes are used to avoid confusion with the primes of the Lorentz transformation, are rotated by 135 deg with respect to the coordinates of the interface. Once the isofrequency and impedance patterns have been drawn, the usual boundary condition, $k_{x\mathrm{i}} = k_{x\mathrm{r}} = k_{x\mathrm{t}}$, is applied, the interface being still positioned at $z = 0$. It is interesting to note that the oblique motion gives rise to negative refraction, which was not possible for perpendicular motion. Note that negative refraction for a medium moving at a subluminal velocity parallel to the interface, corresponding to a rotation of $\theta_\mathbf{v} = 90$ deg, was reported in [19]. The rotation in this scenario also increases the wave impedance.

2.8 Connection with Spacetime-Modulated Systems

The problem studied until this point is closely related to the problem of spacetime modulation (as opposed to motion) where the medium parameters are space- and time-invariant and the interface is moving in the form of a perturbation induced by an external modulation, without involving any transfer of matter [3, 66, 67]. Figure 2.10 compares the two problems, with

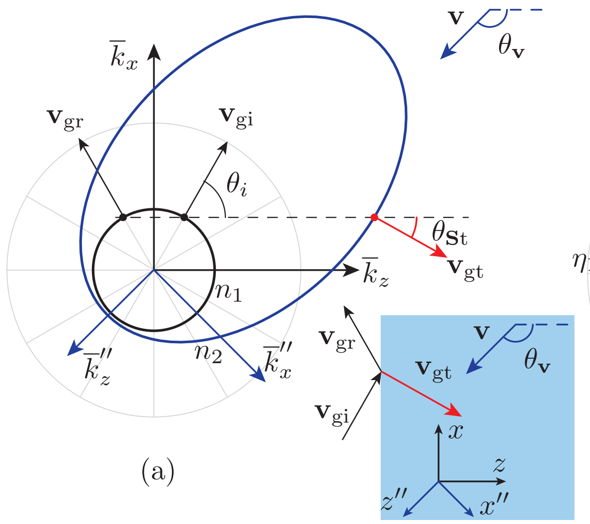

Figure 2.9 Same as Fig. 2.6, but for medium motion at angle $\theta_{\mathbf{v}} = 135°$.

Fig. 2.10(a) representing the problem studied here and Fig. 2.10(b) the related spacetime-modulated problem. In the former case, the reference frame is the rest frame (vacuum), corresponding to the xz coordinate system, where the interface is stationary and the particles of the medium (e.g., fluid molecules) move in the direction $\mathbf{v}_{\mathrm{m}}$. In the latter case, the reference frame is the moving frame (dielectric), corresponding to the $x'z'$ coordinate system, where the particles of the medium (e.g., fluid molecules) are stationary, while the interface moves in the direction $\mathbf{v}_{\mathrm{int}} = -\mathbf{v}_{\mathrm{m}}$.

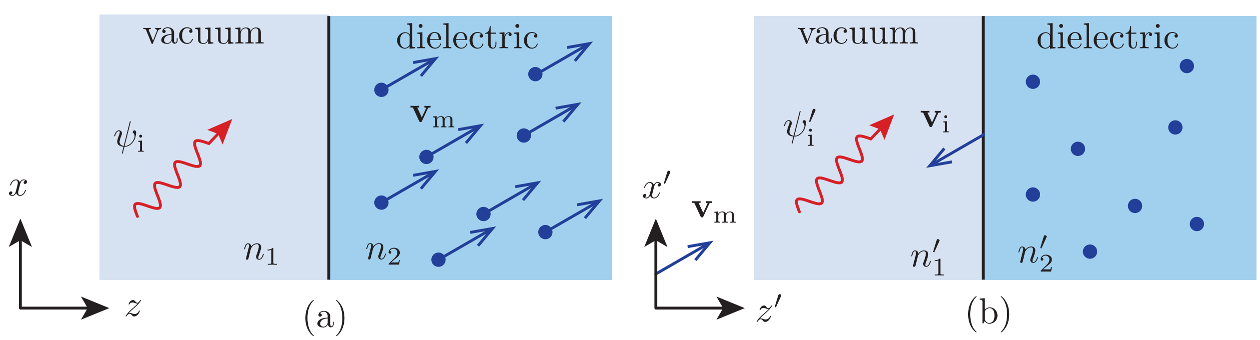

Figure 2.10 Comparison of two closely related problems involving motion. (a) Problem studied in this paper. (b) Related spacetime-modulated problem. In both cases, we assume that the incident medium is vacuum, i.e., $n_1 = n'_1 = 1$, and the transmission medium a dielectric fluid that is isotropic at rest.

The two problems are equivalent by constitution and by transformation but different in terms of the physics experienced by a wave incident on the interface: 1) Constitutional equivalence

– In both cases, we have the same set of particles and the same interface between vacuum and the medium formed by these particles, the difference being only a change of system of coordinates; 2) Transformation equivalence – The two problems are Lorentz transformations of each other, and each is therefore perfectly determined by the other; 3) Physics difference[6] – in the case of Fig. 2.10(a), the wave incident from vacuum sees a stationary interface followed by a bianisotropic medium, with electric-magnetic coupling being produced by the motion of particles [11,64], while in the case of Fig. 2.10(b) it sees an isotropic medium across a moving interface, so that distinct scattering phenomenologies occur in the two cases [66,67], with the most striking difference being the presence of Doppler frequency shifting in the latter case due to the interface motion and not in the former due to phase matching (Eq. (2.22b)).

2.9 Conclusion

We have derived the refractive index and impedance relations for bulk moving media and plotted the results in related diagrams in both the subluminal and interluminal regimes. Moreover, we have mathematically and graphically determined the phase and group velocities of the waves scattered at a stationary interface bounding a moving medium, for medium motion perpendicular and oblique with respect to the interface. Finally, we have discussed a connection between this problem and the problem of a spacetime modulated medium.

The experimental implementation of the problem solved in the paper seems challenging given the relativistic velocities of the fluid at the high end of the subluminal regimes and in the interluminal regimes, even if one would resort to the latest fluid dynamics technologies. However, the fluid could be potentially replaced by flows of electrons in naturally bounded two-dimensional plasmonic structures [73,74]. Moreover, spacetime perturbations, i.e., modulations without transfer of matter, of relativistic velocities are perfectly attainable in practice, and are directly related to the problem studied here by Lorentz transformations. The results presented in this paper are therefore not only of theoretical but also of wide practical interest.

[6]The simplest example would be the case where the dielectric reduces to a single charged particle, with charge q (or, more generally, a plasma). The problem of Fig. 2.10(b) is then a problem of electrostatics, since $\partial q/\partial t = 0$, whereas the problem of Fig. 2.10(a) is then a problem of electrodynamics and electromagnetics, since $\partial q/\partial t \neq 0 = i$.

CHAPTER 3 ARTICLE 2: UNIFORM-VELOCITY SPACETIME CRYSTALS

Zoé-Lise Deck-Léger, Nima Chamanara, Maksim Skorobogatiy, Mário G. Silveirinha and Christophe Caloz

Published in Advanced Photonics, Volume 1, Number 5, October 31, 2019

Abstract

We perform a comprehensive analysis of uniform-velocity bilayer spacetime crystals, combining concepts of conventional photonic crystals and special relativity. Given that a spacetime crystal consists of a sequence of spacetime discontinuities, we do this by solving the following sequence of problems: 1) the spacetime interface, 2) the double spacetime interface, or spacetime slab, 3) the unbounded crystal, and 4) the truncated crystal. For these problems, we present the following new results: 1) an extension of the Stokes principle to spacetime interfaces, 2) an interference-based analysis of the interference phenomenology, 3) a quick linear approximation of the dispersion diagrams, a description of simultaneous wavenumber and frequency bandgaps, and 4) the explanation of the effects of different types of spacetime crystal truncations, and the corresponding scattering coefficients. This work may constitute the foundation for a virtually unlimited number of novel canonical spacetime media and metamaterial problems.

3.1 Introduction

Crystals are structures that are periodic, either at the atomic level (e.g. electronic crystals) [75] or at the supermolecular level of artificial scatterers (e.g. photonic crystals) [76]. Their periodicity confers them a dispersion in the form of a bandgap structure, which leads to spatio-temporal filtering. They have a myriad of applications, such as for instance X-ray imaging [77] and Bragg gratings [78] in the case of electromagnetics.

In conventional crystals, the periodicity is purely spatial: the structure is composed of a 1D, 2D or 3D lattice of molecules or artificial particles, which may be seen as a variation of medium parameters in space. Medium variation may also occur in time, and a periodic time variation leads then to time crystals. Time crystals were first studied in the 1960s under the form of temporally modulated 1D structures, whose controlled instabilities led to parametric amplifiers [79, 80] and whose asymmetric frequency transitions led to nonreciprocal devices [81, 82]. Such time crystals [31, 32, 83–85], and more generally time-varying structures [86–88], have recently experienced a renewed attention. Moreover, the concept of spontaneous time crystals, which are time crystals produced by a non-periodic stimulus, was introduced as a new state of matter [29].

Generally, medium variation may occur in both space and time, and a periodic spacetime variation leads to spacetime crystals, supporting extremely rich and largely unexplored physics. Spacetime crystals may be moving-medium structures [89–92] or modulated-medium structures, the former involving the motion of matter, and the latter involving the motion of a perturbation. The two share much of the same physics, including Doppler-like frequency transitions [8], amplification [93,94], and Bradley-aberration deflections [4]. Modulated structures are easier to realize [95], more practical, and more diverse, as they may be superluminal, i.e. faster than the speed of light, have multiple periods, and accelerate without the application of any force [96, 97]. For these reasons, the paper focuses on modulated structures, while comparing them with moving structures whenever appropriate.

Spacetime crystals may generally include the three dimensions of space and the single dimension of time, and are hence (3+1)-D. In this paper, the quantitative developments are restricted to a single dimension of space, corresponding to (1+1)-D crystals, but the qualitative concepts equally apply to (1,2,3+1)-D spacetime crystals.

Figure 3.1 represents two canonical spacetime crystals in spacetime diagrams, where z and t denote space and time, and c is the speed of light in free space. For simplicity, throughout the paper we consider crystals composed of just two homogeneous media with refractive indices n_i and n_j separated by sharp, step discontinuities. The first crystal type, represented in Fig. 3.1(a), is a multiple-periodicity structure (2 periods in the (1+1)-D rectangular-scatterer case). Such multiple-periodicity, which may involve up to 4 periods (3 spatial and one temporal) in the (3+1)-D case, requires the presence of different slopes in the spacetime diagram, and hence multiple velocities. The set of velocities may be discrete (e.g. 2 velocities in the figure) or continuous (e.g. as obtained by rounding the corners of the grey areas in the figure). Some of the features of such crystals may be studied using space-time ray tracing [51, 52, 98–100].

The second crystal type, represented in Fig. 3.1(b), is a single-periodicity structure, featuring perturbation that moves along the z axis with a single and uniform velocity. Such uniform-velocity modulated spacetime crystals have been investigated under the form of traveling-wave amplifiers [44, 45, 101], and, more recently, under various forms for magnetless nonreciprocity [38, 65, 102–105]. The present paper focuses on this type of spacetime crystal because of its greater simplicity, and because this fundamental problem already exhibits

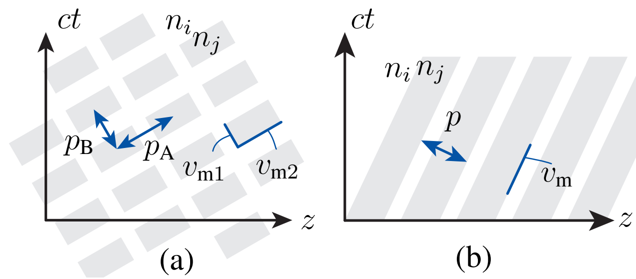

Figure 3.1 Representation of two canonical spacetime crystals. Here, the variable z is intended to represent the hyperspace, i.e. the three dimensions of space. The white and gray regions correspond to media with refractive index n_i and n_j, respectively. (a) Double-period (p_A and p_B) structure, characterized by two velocities, $v_{\mathrm{m}1}$ and $v_{\mathrm{m}2}$), which may be interpreted as acceleration at the corner. (b) Single-period (p) structure, characterized by a unique and uniform velocity, v_{m}.

many unreported and interesting physics. Since a crystal consists of a periodic sequence of medium discontinuities, we shall devote a considerable amount of time on the study of spacetime interfaces corresponding to such discontinuities.

This work studies the scattering of waves from uniform-velocity spacetime crystals [Fig. 3.1(b)] by generalizing standard crystallography and leveraging special relativity. It retrieves the known dispersion diagrams [37, 46] and transfer-matrix results [106], and presents a number of new results, including the generalization of the Stokes principle for spacetime interfaces, the derivation of the interference condition in spacetime slabs, and a complete description of the dispersion diagrams of spacetime crystals, with the identification and explanation of dispersion-slope asymmetry, the demonstration of simultaneous frequency and wavenumber bandgaps and the analytical derivation of the bandgap positions. The calculation of the scattered-wave amplitudes for finite crystals is also provided.

The paper is organized as follows. Section 3.2 presents preliminary concepts and principles, including the description of a spacetime interface, the introduction of generalized spacetime diagrams, the distinction of three velocity regimes in spacetime structures, our strategy to compute the fields scattered by spacetime structures, a brief recall on Lorentz transformations, the proper selection of Lorentz frames for subluminal and superluminal structures, and a discussion on the duality existing between space and time in spacetime systems. Section 3.3 deals with a single interface of a spacetime crystal, deriving its scattering coefficients, its frequency transitions, and generalizing the Stokes relations. Section 3.4 solves the double-interface problem of a spacetime slab, describing its scattering phenomenology, deriving its frequency transitions, phase shifts and scattering coefficients, and graphically illustrates the gap interference condition. Section 3.5 studies an unbounded bilayer crystal. It develops a linear approximation of the dispersion diagram, finds the position of the centers of the bandgaps, derives the transfer matrix for a unit cell of a spacetime crystal, subsequently computes the dispersion relation and explains its spacetime specifics in terms of the Brillouin zone, the complex bandgaps, and the bandgap edges. Section 3.6 uses the previously derived unit-cell transfer matrix to compute the scattered amplitudes across a finite spacetime crystal. Finally, conclusions are provided in Sec. 3.7.

3.2 Preliminaries

Physical Nature of a Modulated Spacetime Interface

Modulated spacetime interfaces should be understood as perturbations propagating in a stationary media. This may be understood using the following analogy: consider a chain of standing domino tiles, sufficiently closely spaced to topple their neighbours upon falling, so that a chain reaction can be launched by knocking down the first tile. In such a reaction, one clearly sees the "interface" between the fallen and standing parts of the chain propagating along the structure at a specific velocity, with the dominoes themselves on either side of the interface either standing or fallen but not moving in the direction of propagation. The velocity of such an interface along the chain would be limited by the time it takes for one tile to topple the next. We could nevertheless imagine the situation where the tiles could be knocked down by independent external triggers distributed along the domino chain. If these triggers were activated successively at vanishingly small time intervals, the interface velocity would be superluminal, and it would even be infinite if the triggers were operated simultaneously. We stress again that the interfaces described above should be distinguished from the moving interfaces that constitute an altogether different physical system due to the physical movement of the media. For example, in such structures the superluminal regime is physically prohibited.

Spacetime Diagrams

Subluminal and superluminal modulation regimes give rise to distinct physics [37, 46, 96, 97] and require distinct treatments. Figures 3.2(a) and (b) sketch the interaction of an incident wave with a spacetime interface. In the subluminal case of Fig. 3.2(a), the incident wave catches up with the receding interface. In the superluminal case of of Fig. 3.2(b), the interface, which is faster than the wave, overcomes the incident wave, which was launched earlier. Figures 3.2(c) and 3.2(d) graphically summarize the scattering from a subluminal interface and from a superluminal interface in spacetime diagrams, with corresponding spacetime interface trajectories (white and gray areas), wave trajectories (in blue), scattering coefficients (in black) and relevant spacetime coordinate frames (laboratory frame in black and moving frame in red).

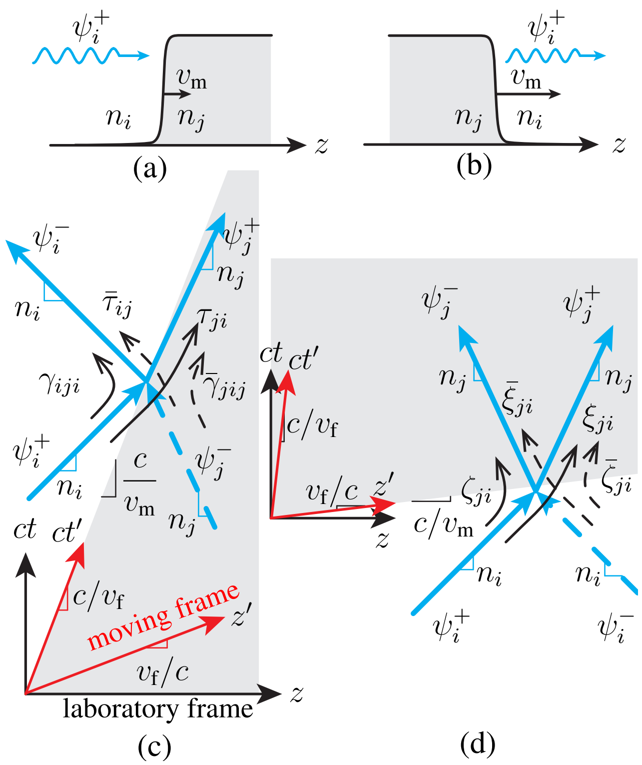

Figure 3.2 Scattering at a spacetime interface. The white and gray regions correspond to media i and j, with refractive indices n_i and n_j ($n_i < n_j$). (a) Sketch of a wave incident on a subluminal interface. (b) Same as (a) but for a superluminal interface. (c) Scattering from a subluminal ($v_\mathrm{m} < c$) interface in a spacetime diagram. The blue arrows represent wave trajectories (referring to a specific phase point of the waveform), while the black arrows represent scattering coefficients. The dashed lines correspond to incidence from the right. The laboratory and moving frames are superimposed with common origin, and the moving frame has the same velocity as the interface ($v_\mathrm{f}/c = v_\mathrm{m}/c$). (d) Same as (c) but for a superluminal interface ($v_\mathrm{m} > c$), with moving frame having the inverse velocity of the interface ($v_\mathrm{f}/c = c/v_\mathrm{m}$).

Given our assumption that the transitions between the homogeneous media i and j forming the crystal are step-like transitions, the spacetime interface problem is mathematically described by the following refractive index function

$$n(z - v_\mathrm{m}t) = n_i + (n_j - n_i)\theta(z - v_\mathrm{m}t) \tag{3.1a}$$

for Fig. 3.2(a) and

$$n(t - z/v_\mathrm{m}) = n_i + (n_j - n_i)\theta(t - z/v_\mathrm{m}) \tag{3.1b}$$

for Fig. 3.2(b), where $\theta(\cdot)$ is the Heaviside step function and v_m is the velocity of the modulated interface. Although such a step transition cannot be realized in practice, the step profile is an adequate description of it as long as the transition width is smaller that the wavelength in the subluminal case or the transition time is smaller than the period in the superluminal case. The problem of scattering from gradual spacetime interfaces does not generally admit closed-form solutions, but solutions for specific gradual profile may be found [27, 107]. In the case of a crystal, scattering from gradual spacetime profiles are found using a coupled-mode approach [37, 46]. Note also that setting $v_\mathrm{m} = 0$ in (3.1a) reduces the interface to a purely spatial one, while setting $v_\mathrm{m} = \infty$ in (3.1b) reduces the interface to a purely temporal one. Purely spatial and purely temporal problems have been widely investigated, and our results throughout the paper may be verified to correspond to those in the literature at these limit cases. Also note that (3.1a) and (3.1b) are different from each other, because we have chosen here to have the incident wave always in medium i, for symmetry with respect to the luminal axis $ct = z$; the other option would have been to use (3.1a) for all regimes, with an increasing v_m corresponding to a rotation of the interface in Fig. 3.2(a). In that case, the incidence media would be different for the subluminal or superluminal regimes. The symmetry between subluminal and superluminal problems will be further discussed in Sec. 3.2.

The trajectories of the interfaces in the spacetime diagrams of Fig. 3.2 have a slope that is inversely proportional to their velocity, i.e., equal to $\partial(ct)/\partial z_\text{traj.}(t) = [\partial z_\text{traj.}(t)/\partial(ct)]^{-1} = c/\text{velocity}$. The slope is therefore steeper for the subluminal case than for the superluminal case. Since the media at either side of the interface are homogeneous, the waves propagate in them at uniform velocities $v_i = c/n_i$ and $v_j = c/n_j$, that correspond to straight trajectories with slopes $c/v_i = n_i$ and $c/v_j = n_j$. Thus the slopes of the wave trajectories are steeper in the slower, or denser, medium j. Throughout the paper, we restrict our analysis to nondispersive structures, which would be a valid approximation in a system of moderate dispersion. In a regime of stronger dispersion, the velocity of the reflected wave would be different from that of the incident wave given the frequency shift induced by the interface.

The waves in medium (i, j) in the $\pm z$ directions are denoted $\psi^{\pm}_{i,j}$, with ψ representing any of the transverse components of the electromagnetic fields $\mathbf{E}$, $\mathbf{D}$, $\mathbf{H}$ and $\mathbf{B}$ [108]. The scattering problem for incidence from the left is called the forward problem and for incidence from the right the backward problem. The scattering coefficients for the forward problem are γ and τ for the subluminal regime and ζ and ξ for the superluminal regime, and the scattering coefficients for the backward problem are denoted by barred oversets ($\bar{\gamma}, \bar{\tau}$ and $\bar{\zeta}, \bar{\xi}$), that we shall simply refer to as "barred" for conciseness. All these coefficients will be detailed in Sec. 3.3. Note that the incident wave can propagate in the same direction as the interface or medium, i.e., $\mathrm{sgn}(v_{\mathrm{inc}}) = \mathrm{sgn}(v_{\mathrm{m}})$, as in Fig. 3.2, or in the direction opposite to the interface or medium, i.e., $\mathrm{sgn}(v_{\mathrm{inc}}) = -\mathrm{sgn}(v_{\mathrm{m}})$. These two cases, which we refer here to as codirectional and contradirectional, respectively, are important to distinguish because they involve drastically different physics, as clearly apparent in the Doppler phenomenon.

To solve scattering problems involving constant velocities, we will use the Lorentz transformations between the laboratory frame and the moving frame, moving at the uniform velocity v_{f}. These frames are shown in Fig. 3.2, with coordinates axes (z, ct) and (z', ct'), respectively. In the subluminal case [Fig. 3.2(a)], the interface appears stationary in the moving frame, i.e., the ct' axis is parallel to the interface. In the superluminal case [Fig. 3.2(b)], the interface appears purely temporal in the moving frame, i.e. the z' axis is parallel to the interface. The justification for this choice will be provided in Sec. 3.2.

Space-Time Duality

Subluminal and superluminal structures are symmetric around the light line ($z = ct$) in the spacetime diagram, as shown in Fig. 3.3 for the cases of an interface and a slab. This symmetry is due to the fact that changing from a subluminal to a superluminal problem reverts to exchanging space and time: $v_{\mathrm{sub}}/c = \partial z/\partial(ct) \leftrightarrow \partial(ct)/\partial z = c/v_{\mathrm{sub}} = v_{\mathrm{sup}}/c$. The subluminal and superluminal structures are thus related through a spacetime inversion. This geometrical symmetry manifests a fundamental duality between the subluminal and superluminal problems.

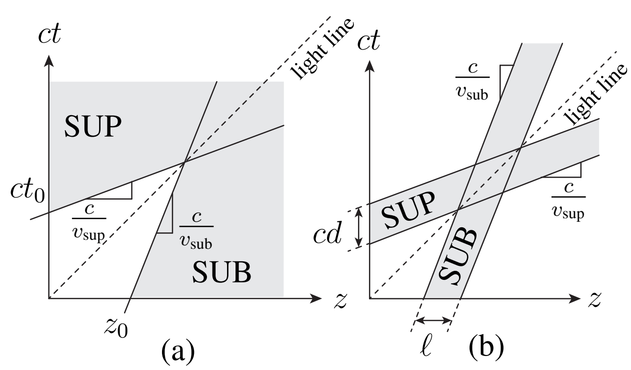

Figure 3.3 Spacetime-inversion symmetry of subluminal (SUB) and superluminal (SUP) structures. (a) Interfaces. (b) Slabs.

This structural duality is completed by the spacetime duality of Maxwell equations. Consider for instance the electric field in any of the (homogeneous) medium on either side of the discontinuities,

$$\frac{\partial^2 E_x}{\partial z^2} - n^2(z - v_\mathrm{m}t)\frac{\partial^2 E_x}{\partial (ct)^2} = 0. \tag{3.2}$$

Interchanging space and time in this equation, and also applying $n \to 1/n$, since $n = c/v = \partial(ct)/\partial z$ and $v_\mathrm{m}/c \to c/v_\mathrm{m}$, indeed transforms the equation into itself. Thus, the wave equation is also symmetric under spacetime inversion.

Therefore, subluminal and superluminal spacetime electromagnetic problems are the dual of each other. Table 3.1 lists the variables related to the spacetime duality. The first four row substitutions are the ones just discussed for the problem of an interface. The fifth row refers to the duality between the length ℓ of a subluminal slab and the duration cd of a superluminal slab, as illustrated in Fig. 3.3(b). The sixth and sevenths rows correspond to the duality of plane wave solutions in spacetime scattering problems.

Table 3.1 Duality transformations between the subluminal and superluminal regimes.

Subluminal regime		Superluminal regime	
space	z	time	ct
time	ct	space	z
modulation velocity	$\frac{v_\mathrm{m}}{c}$	inverse velocity	$\frac{c}{v_\mathrm{m}}$
refractive index	n	inverse index	$\frac{1}{n}$
phase velocity	$\frac{v}{c} = \frac{1}{n}$	inverse phase velocity	$\frac{c}{v} = n$
length	ℓ	duration	cd
wavelength	λ	period	cT
frequency	$\frac{\omega}{c}$	wavenumber	k

Note that the duality between space and time is incomplete, because one can go backwards in space but not in time. As a consequence, we shall see that the scattering coefficients are not related to each other, although the phase quantities will always be. Therefore, once the phase quantities are found for the subluminal case, the phases for the superluminal case are deduced by applying the substitutions noted in Tab. 3.1.

The Interluminal Regime

In the preceding sections, we distinguished the subluminal and the superluminal regime, but omitted to discuss a third velocity regime which we will describe here. To be more precise, we should refer to a modulated system as strictly subluminal when the modulation is slower than the slowest wave involved, i.e., here, $v_\mathrm{m} < v_j$, with $v_j < v_i$, and strictly superluminal when it is faster than the fastest wave involved, i.e., here, $v_\mathrm{m} > v_i$. The velocity range between these two regimes, $v_j \leq v_\mathrm{m} \leq v_i$, corresponds to a third regime, which we call here the interluminal regime. This regime involves yet different physics and requires yet a different treatment than the strictly sub- and superluminal regimes, as illustrated in Fig. 3.4: the incident wave in medium i scatters a single wave in the codirectional case (Fig. 3.4(a)) and three waves in the contradirectional case (Fig. 3.4(b)) [43, 109, 110].

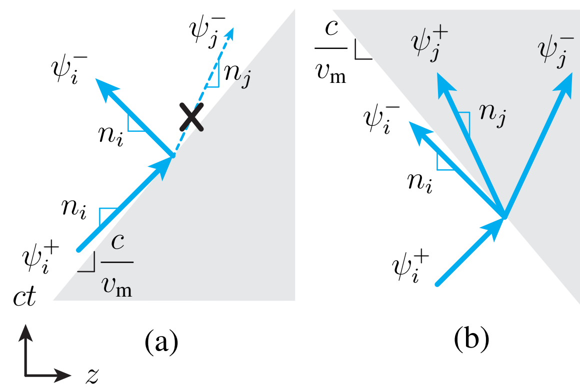

Figure 3.4 Graphical description of the interluminal regime in spacetime diagram. (a) Codirectional case, with a single scattered wave. (b) Contradirectional case, with three scattered waves.

Let us first consider the codirectional case. In the forward problem of the strictly subluminal regime [Fig. 3.2(a)], the incident wave, ψ_i^+, is scattered into a reflected wave, ψ_i^-, and a transmitted wave, ψ_j^+. Progressively increasing v_m, and therefore decreasing the slope of the interface, brings the interface closer and closer to the trajectory of the transmitted wave. At the point where the interface propagates at the same velocity as the wave transmitted in medium j, i.e., $v_\mathrm{m} = v_j$, a shock wave is produced from the accumulation of the transmitted wave at the interface. This is the upper limit of the strictly subluminal regime, and the lower limit of the interluminal regime. Beyond this limit ($v_\mathrm{m} > v_j$, but still with $v_\mathrm{m} < v_i$), the incident wave cannot penetrate any more into medium j because it would otherwise be overtaken by the interface. Thus, scattering reduces here to a single reflected wave. Further increasing the velocity leads to the situation where the interface propagates at the same velocity as the incident wave, i.e., $v_\mathrm{m} = v_i$. At this point, the incident wave is barely catching up with the interface, and so reflection tends to zero. Beyond this limit, we enter the strictly superluminal regime, where the incident wave cannot catch up with the interface unless it was launched earlier than it, which is the case in Fig. 3.2(b).

For the contradirectional case, we perform a similar thought experiment: starting with a strictly subluminal contradirectional problem, by setting a negative slope for the interface in [Fig. 3.2(a)], and increasing the velocity, we arrive to a point where the velocity of the modulation is equal to the velocity of the wave in the media, i.e. $v_\mathrm{m} = -v_j$, and so a wave will form, propagating along the interface. The scattering will therefore include three waves: a reflected wave, a later backward wave and a later forward wave. For a further increased velocity, the interface catches up with the reflected wave, i.e. $v_\mathrm{m} = -v_i$, leading to another shock wave from the accumulation of the reflected wave. Beyond this limit, we enter the strictly superluminal regime.

In this paper, we shall focus on the strictly subluminal and strictly superluminal regimes, which we will call subluminal or superluminal for brevity.

Recall of Special Relativity Concepts

We noted in Sec. 3.2 that we will use Lorentz transformations between the laboratory and moving frames to solve spacetime problems. We present here a brief recall of the Lorentz transformation tools required for this.

Lorentz Transformations and Lorentz Frames

Intervals of space and time in frames moving at a relative velocity v_f are related through the Lorentz transformations [111]

$$z' = \gamma\left(z - \frac{v_\mathrm{f}}{c}ct\right), \qquad ct' = \gamma\left(ct - \frac{v_\mathrm{f}}{c}z\right), \tag{3.3}$$

where

$$\gamma = (1 - v_\mathrm{f}^2/c^2)^{-1/2} \tag{3.4}$$

is the Lorentz factor, where the primed and unprimed quantities refer to quantities measured in the moving frame and in the laboratory frame, respectively. The inverse relations are found by exchanging the primed and unprimed quantities and replacing v_f by $-v_\mathrm{f}$ in (3.3):

$$z = \gamma\left(z' + \frac{v_\mathrm{f}}{c}ct'\right), \qquad ct = \gamma\left(ct' + \frac{v_\mathrm{f}}{c}z'\right). \tag{3.5}$$

From these Lorentz transformations, we may superimpose laboratory and moving frames onto the same spacetime plot, as done in Fig. 3.2. The laboratory frame coordinates are chosen to be orthogonal, and so the moving frame coordinates must be skewed, with the axes slopes found as follows. The z' axis corresponds to $ct' = 0$. Enforcing this in (3.5) yields $ct = (v_\mathrm{f}/c)z$, which provides v_f/c for the slope of the z' axis. Similarly, the ct' axis corresponds to $z' = 0$, and enforcing this in (3.5) yields the $z = (v_\mathrm{f}/c)ct$ which provides c/v_f for the ct' axis slope.

Velocity Addition Formula

Velocities measured in different frames do not simply differ by the frame velocity, i.e. the velocity measured in the laboratory frame, v, is not the sum of the moving frame velocity, v_f, and the velocity measured in the moving frame, $v' = \mathrm{d}z'/\mathrm{d}t'$. The correct relationship between the velocities measured in the different frames is found by applying the chain rule to the definition of v, $v = \mathrm{d}z/\mathrm{d}t$, and replacing the resulting terms by the derivative of the first relation of (3.5) with respect to t' and by the derivative of the second relation of (3.3) with respect to t, i.e.,

$$v = \frac{\mathrm{d}z}{\mathrm{d}t'}\frac{\mathrm{d}t'}{\mathrm{d}t} = \gamma^2 \left(v' + v_\mathrm{f}\right)\left(1 - \frac{v_\mathrm{f} v}{c^2}\right), \tag{3.6}$$

and solving for v. The result is

$$v = \frac{v' + v_\mathrm{f}}{1 + \dfrac{v' v_\mathrm{f}}{c^2}}. \tag{3.7a}$$

and the inverse is

$$v' = \frac{v - v_\mathrm{f}}{1 - \dfrac{v v_\mathrm{f}}{c^2}}. \tag{3.7b}$$

Spectral Lorentz Transformations

The phase of a wave is observer-independent [112]. For instance, different observers agree whether a wave is at a maximum or at a minimum, although they do not agree on the distance between two maxima (wavelength) and the time between two maxima (period). Thus

$$\phi^{\pm\prime} = \phi^{\pm}, \tag{3.8}$$

with the phases defined as

$$\phi^{\pm} = k^{\pm} z \mp \omega^{\pm} t, \qquad \phi^{\pm\prime} = k^{\pm\prime} z' \mp \omega^{\pm\prime} t', \tag{3.9}$$

where the wavenumbers $k^{\pm}$ are related to the corresponding frequencies through the dispersion relation $k^{\pm} = \pm\omega^{\pm}/v$. Using the expressions for z and t in (3.5), and resolving in (3.8) provides the frequency and wavenumber transformations

$$k^{\pm\prime} = \gamma\left(k^{\pm} \mp \frac{v_{\mathrm{f}}}{c}\frac{\omega^{\pm}}{c}\right), \qquad \frac{\omega^{\pm\prime}}{c} = \gamma\left(\frac{\omega^{\pm}}{c} \mp \frac{v_{\mathrm{f}}}{c}k^{\pm}\right). \tag{3.10}$$

Comparing these transformation with (3.3) reveals that k^{+} and ω^{+}/c transform as z and ct.

Field Transformations

Consider harmonic plane waves propagating along $\pm z$ with the electric field phasor $\mathbf{E} = E_x\hat{x}$ and magnetic field $\mathbf{H} = H_y\hat{y}$. These fields may be written as

$$E_x^{\pm} = A^{\pm}\mathrm{e}^{\pm i\phi^{\pm}}, \;\text{ with }\; \phi^{\pm} = k^{\pm}z \mp \omega^{\pm}t. \tag{3.11}$$

For later use, we relate the other fields to $E_x^{\pm}$ through the wave impedance $\eta = \sqrt{\mu/\epsilon}$ and phase velocity $v = 1/\sqrt{\epsilon\mu}$ as

$$H_y^{\pm} = \mp\frac{1}{\eta}E_x^{\pm}, \tag{3.12a}$$

$$B_y^{\pm} = \mp\frac{1}{v}E_x^{\pm}, \tag{3.12b}$$

$$D_x^{\pm} = \epsilon E_x^{\pm} = \frac{1}{v\eta}E_x^{\pm}, \tag{3.12c}$$

which follow from Maxwell equations, with the assumption of a purely dielectric medium having a purely real and positive permittivity, and no spatial or temporal dispersion.

The fields measured in the laboratory and moving frames are related through [113]

$$E_x' = \gamma\left(E_y - v_{\mathrm{f}}B_y\right), \quad H_y' = \gamma\left(H_x - v_{\mathrm{f}}D_x\right), \tag{3.13a}$$

$$D_x' = \gamma\left(D_x - \frac{v_{\mathrm{f}}}{c^2}H_y\right), \quad B_y' = \gamma\left(B_y - \frac{v_{\mathrm{f}}}{c^2}E_x\right), \tag{3.13b}$$

with the inverse relations again obtained by changing the sign of v_{f} and interchanging the primed and unprimed quantities. The primed counterpart of (3.11) therefore reads

$$E_x^{\pm'} = A^{\pm'}\mathrm{e}^{\pm i\phi^{\pm'}}, \;\text{ with }\; \phi^{\pm'} = k^{\pm'}z' \mp \omega^{\pm'}t', \tag{3.14}$$

and the primed counterparts of (3.12) are presented in App. A. For later use, we note that the phase velocity $v^{\pm'}$ transforms as (3.7) [112, 114], but with a negative sign for v_{f} since media appears to be moving in the $-z$ direction if the frame is moving in the $+z$ direction. Thus, the phase velocity in the moving frame is

$$v^{\pm\prime} = \frac{v^{\pm} + v_{\mathrm{f}}}{1 + \frac{v^{\pm} v_{\mathrm{f}}}{c^2}}. \tag{3.15}$$

Resolution Strategy

Electromagnetic problems involving moving media are conventionally solved in the moving frame where the system is stationary. The solutions are then converted back to the laboratory frame using Lorentz transformations. The situation for modulated media is more subtle. The overall medium is stationary, with the perturbation propagating through it. In a moving frame having the same velocity as the perturbation, the perturbation appears stationary, however the media on both sides of it appear to be in motion. As we show in App. A, moving media appear bianisotropic [6, 112, 115]. The complexity associated with such a bianisotropy defeats the original purpose of using the Lorentz transformation. In order to resolve this complication, we resort to the following hybrid strategy: we first apply the field continuity conditions in the moving frame, then transform the results to the laboratory frame, and finally apply the constitutive relations or the dispersion relations in the laboratory frame.

We stated in Sec. 3.2 that the moving frames for the subluminal and superluminal problems were chosen such that the problems appeared purely spatial or purely temporal, respectively, in the moving frames. We now revisit this statement in the light of the space and time Lorentz transformations presented in Sec. 3.2.

In the subluminal regime [Fig. 3.2(a)], we select the moving frame so that it is co-propagating with the interface, at a velocity equal to that of the interface, $v_{\mathrm{f}} = v_{\mathrm{m}}$, as conventionally done. The interface is then purely spatial (stationary) in that frame, positioned here at $z' = 0$, which corresponds to the ct' axis being parallel to the interface.

In the superluminal regime [Fig. 3.2(b)], as discussed in Sec. 3.2, the selection of a co-moving frame with ($v_{\mathrm{f}} = v_{\mathrm{m}}$) is not possible, since Lorentz transformations apply only to frames moving at subluminal velocities. Indeed, the corresponding superluminal Lorentz transformations would result into nonphysical imaginary space and time quantities, as can be seen by setting $v_{\mathrm{f}} > c$ in (3.4). Instead, we choose a frame where the interface appears to be purely temporal (sudden change of material properties at a given time t'), occurring here at $t' = 0$, which corresponds to the z' axis being parallel to the interface [47]. We then graphically find that the moving frame velocity is $c/v_{\mathrm{m}} = v_{\mathrm{f}}/c$. We may also find this result mathematically by inspecting (3.7b) and finding the condition for $v'_{\mathrm{m}} = \infty$, which was shown in Sec. 3.2 to correspond to a purely temporal interface (instantaneous change in the material properties). Since $v_\mathrm{m} > c$, we have $v_\mathrm{f} < c$, and the Lorentz transformations are now applicable.

3.3 Spacetime Interface

Scattering Coefficients

In this section, we compute the scattering coefficients denoted by lowercase Greek symbols in Fig. 3.2 for the case of a single interface that moves with a uniform velocity v_m through the stationary media characterized by two distinct refractive indices n_i and n_j respectively to the left and to the right of the interface. We start with the subluminal regime following the strategy outlined in Sec. 3.2. First, we derive the continuity conditions at the interface in the moving frame that has the same velocity as that of the interface, $v_\mathrm{f} = v_\mathrm{m}$, as was suggested in Sec. 3.2. Since the interface appears purely spatial in the moving frame, the usual boundary conditions apply in it, i.e.,

$$E_{xi}{}' = E_{xj}{}'\big|_{z'=0}\,, \qquad H_{yi}{}' = H_{yj}{}'\big|_{z'=0}\,, \tag{3.16}$$

which involve the total fields in media i and j, corresponding to $\psi_{i,j} = \psi_{i,j}^{+} + \psi_{i,j}^{-}$ in Fig. 3.2(a). We next express these fields in terms of their unprimed counterparts using the Lorentz transformations (3.13a), which yields the continuity conditions

$$E_{xi} - v_\mathrm{f} B_{yi} = E_{xj} - v_\mathrm{f} B_{yj}\big|_{z-v_\mathrm{f}t=0}\,, \tag{3.17a}$$

$$H_{yi} - v_\mathrm{f} D_{xi} = H_{yj} - v_\mathrm{f} D_{xj}\big|_{z-v_\mathrm{f}t=0}\,. \tag{3.17b}$$

Finally, the frame velocity is set equal to the modulation velocity, i.e. $v_\mathrm{f} = v_\mathrm{m}$.

To study the forward problem, corresponding to incidence $\psi_i^{+} \neq 0$ and $\psi_j^{-} = 0$ (See Fig. 3.2), we enforce the continuity conditions (3.17) by inserting (3.11) into (3.17) with $\psi_j^{-} = 0$, which yields

$$\gamma_{iji} = \frac{A_i^{-}}{A_i^{+}}\bigg|_{A_j^{-}=0} = \frac{\eta_j - \eta_i}{\eta_j + \eta_i}\left(\frac{1 - v_\mathrm{m}/v_i}{1 + v_\mathrm{m}/v_i}\right), \tag{3.18a}$$

$$\tau_{ji} = \frac{A_j^{+}}{A_i^{+}}\bigg|_{A_j^{-}=0} = \frac{2\eta_j}{\eta_i + n_j}\left(\frac{1 - v_\mathrm{m}/v_i}{1 - v_\mathrm{m}/v_j}\right). \tag{3.18b}$$

The subscripts in the reflection coefficient indicate that the wave travels from medium i, reaches medium j, and then reflects back to medium i. This notation will be useful later on to distinguish forward and backward waves in multiple-interface problems.

The results of (E.2) are valid across the subluminal range, which was shown to extend from $-v_j$ to v_j in Sec. 3.2. According to (E.2) the transmission coefficient increases monotonically while the reflection coefficients decreases monotonically across this velocity range. In the contradirectional case, the reflection coefficient is greater than in the purely spatial case, while in the codirectional case, the reflection is less than in the purely spatial case: the moving interface "cushions" the wave.

We next study the backward problem, corresponding to the incidence $\psi_i^+ = 0$ and $\psi_j^- \neq 0$. Inserting (3.11) into (3.17), or alternatively reversing the sign of v_m and exchanging i and j in (E.2), results into

$$\bar{\gamma}_{jij}(v_\mathrm{m}) = \left.\frac{A_j^+}{A_j^-}\right|_{A_i^+=0} = \frac{\eta_i - \eta_j}{\eta_i + \eta_j}\left(\frac{1 + v_\mathrm{m}/v_j}{1 - v_\mathrm{m}/v_j}\right), \tag{3.19a}$$

$$\bar{\tau}_{ij}(v_\mathrm{m}) = \left.\frac{A_i^-}{A_j^-}\right|_{A_i^+=0} = \frac{2\eta_i}{\eta_j + n_i}\left(\frac{1 + v_\mathrm{m}/v_j}{1 + v_\mathrm{m}/v_i}\right). \tag{3.19b}$$

We now turn to the superluminal regime. In the moving frame, where the interface appears purely temporal, the continuous fields are [25, 107]

$${D_{xi}}' = {D_{xj}}'|_{t'=0}\,, \;\; {B_{yi}}' = {B_{yj}}'|_{t'=0}\,. \tag{3.20}$$

Applying the Lorentz transformation (3.13b) yields the continuity relations

$$D_{xi} - \frac{v_\mathrm{f}}{c^2}H_{yi} = D_{xj} - \left.\frac{v_\mathrm{f}}{c^2}H_{yj}\right|_{t-\frac{v_\mathrm{f}}{c^2}z=0}, \tag{3.21a}$$

$$B_{yi} - \frac{v_\mathrm{f}}{c^2}E_{xi} = B_{yj} - \left.\frac{v_\mathrm{f}}{c^2}E_{xj}\right|_{t-\frac{v_\mathrm{f}}{c^2}z=0}. \tag{3.21b}$$

We start by studying the forward problem, corresponding to incidence $\psi_i^+ \neq 0$ and $\psi_i^- = 0$. The scattering coefficients are found by inserting (3.12) into (3.21) with $\psi_i^- = 0$, which yields the later backward and later forward coefficients

$$\zeta_{ji} = \left.\frac{A_j^-}{A_i^+}\right|_{A_i^-=0} = \frac{\eta_i - \eta_j}{2\eta_i}\left(\frac{1 - v_\mathrm{m}/v_i}{1 + v_\mathrm{m}/v_j}\right), \tag{3.22a}$$

$$\xi_{ji} = \left.\frac{A_j^+}{A_i^+}\right|_{A_i^-=0} = \frac{\eta_i + \eta_j}{2\eta_i}\left(\frac{1 - v_\mathrm{m}/v_i}{1 - v_\mathrm{m}/v_j}\right). \tag{3.22b}$$

The scattering coefficients for the backward problem are found by reversing the velocity sign, but not the exchanging the media, since both waves originate in the same medium, contrarily to the subluminal case, and read

$$\bar{\zeta}_{ji} = \left.\frac{A_j^+}{A_i^-}\right|_{A_i^+=0} = \zeta_{ji}(-v_\mathrm{m}). \tag{3.23a}$$

$$\bar{\xi}_{ji} = \left.\frac{A_j^-}{A_i^-}\right|_{A_i^+=0} = \xi_{ji}(-v_\mathrm{m}), \tag{3.23b}$$

Note that (3.17) with the substitution of $v_\mathrm{f} = v_\mathrm{m}$ is identical to (3.21) with the substitution $v_\mathrm{f}/c^2 = 1/v_\mathrm{m}$, which is a consequence of the space-time duality between subluminal and superluminal regimes as described in Sec. 3.2. Therefore the same boundary conditions apply for all regimes. However, we note the results in the subluminal and the superluminal regime are different: this is due to the fact that in the subluminal case, for the forward problem, $\psi_i^+ + \psi_i^- = \psi_j^+$ while for the superluminal case, the reflection is on the other side of the equality sign: $\psi_i^+ = \psi_j^+ + \psi_j^-$. App. A provides an alternative derivation of the continuity conditions for all regimes.

Generalization of the Stokes Principle

To facilitate the later study of multiple scattering (Sec. 3.4), we now establish relations between the scattering coefficients of forward and backward problems derived in Sec. 3.3. This leads to a generalization of the conventional Stokes relations [116] from stationary interfaces to spacetime interfaces.

The conventional Stokes relations are derived upon the basis of a time-reversal symmetry argument: time-reversing, or equivalently, reversing the direction of the waves scattered from an interface returns them to their origin. We extend here this argument to the spacetime interface, with the help of Fig. 3.5. The subluminal problem is represented in Fig. 3.5(a). The bottom part of the figure shows the scattering problem that we have already solved, while the top part shows its time-reversed counterpart, where the velocity signs of the two scattered waves have been reversed, along with the velocity sign of the interface. The scattered waves must return to their origin with the same amplitude, from the time-reversal symmetry argument, and the additional scattering possibility must therefore cancel out. Enforcing the symmetry yields then the subluminal generalized Stokes relations, which may be directly read out from the figure as

$$\bar{\gamma}_{iji}\gamma_{iji} + \tau_{ij}\tau_{ji} = 1, \tag{3.24a}$$

$$\bar{\tau}_{ji}\gamma_{iji} + \gamma_{jij}\tau_{ji} = 0. \tag{3.24b}$$

From these two generalized Stokes conditions we find a third relation, which will be used in Sec. 3.4 to simplify the problem of total scattering from a double interface: barring the unbarred coefficients and unbarring the barred coefficients in (3.24a), and comparing the resulting equations with the original equation of (3.24a), we find that

$$\bar{\tau}_{ij}\bar{\tau}_{ji} = \tau_{ij}\tau_{ji}. \tag{3.24c}$$

The superluminal case is represented in Fig. 3.5(b), with the initial problem at the bottom and the time-reversed problem at the top. The generalized superluminal Stokes relations are again read out from the figure, which gives now

$$\bar{\zeta}_{ij}\zeta_{ji} + \xi_{ij}\xi_{ji} = 1, \tag{3.25a}$$

$$\bar{\xi}_{ij}\zeta_{ji} + \zeta_{ij}\xi_{ji} = 0. \tag{3.25b}$$

which are of the same form as their subluminal counterparts. An additional relation, which will be used in Sec. 3.4 to calculate the total scattering from a slab, is found by rewriting (3.25b) as $\bar{\xi}_{ij} = -\xi_{ji}\zeta_{ij}/\zeta_{ji}$, exchanging i and j in this relation to obtain $\bar{\xi}_{ji} = -\xi_{ij}\zeta_{ji}/\zeta_{ij}$, and taking the product of these two, to find

$$\bar{\xi}_{ij}\bar{\xi}_{ji} = \xi_{ji}\xi_{ij}. \tag{3.25c}$$

Barring the unbarred coefficients and unbarring the barred coefficients in (3.25a) and using the relation (3.25c) leads then to

$$\bar{\zeta}_{ij}\zeta_{ji} = \zeta_{ij}\bar{\zeta}_{ji}. \tag{3.25d}$$

Frequency Transitions

The waves scattered from a spacetime interface undergo Doppler-like frequency transitions. We calculate here these frequency transitions, starting again with the subluminal regime. Inserting the moving-frame fields (3.14) into (3.16) leads to the result that the frequencies are conserved in the moving frame, consistently with the fact that the interface is stationary in that frame. We denote this conserved frequency ω_{e}', with

$${\omega_{\mathrm{e}}}' = {\omega_i^{+}}' = \omega_i'^{-} = \omega_j'^{+}. \tag{3.26a}$$

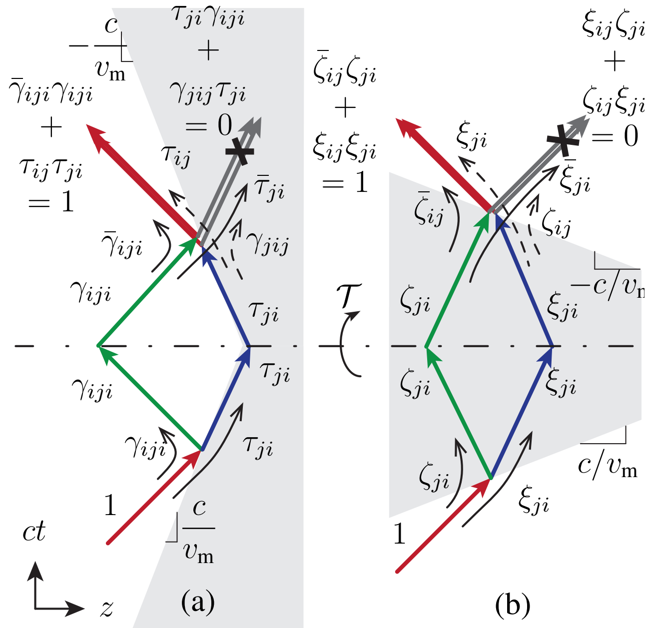

Figure 3.5 Generalization of the Stokes principle. (a) Subluminal regime. (b) Superluminal regime.

Applying the frequency Lorentz transformation (3.10) to (3.26a) with $k_{i,j}^{\pm} = \omega_{i,j}^{\pm}/v_{i,j}$ yields

$$\omega_\mathrm{e} = \omega_i^+ \left(1 - \frac{v_\mathrm{m}}{v_i}\right) = \omega_i^- \left(1 + \frac{v_\mathrm{m}}{v_i}\right) = \omega_j^+ \left(1 - \frac{v_\mathrm{m}}{v_j}\right), \tag{3.26b}$$

where the relation between $\omega_\mathrm{e}{}'$ and ω_e is found by dividing (3.26a) by (3.26b),

$$\omega_\mathrm{e}{}'/\omega_\mathrm{e} = \gamma, \tag{3.27}$$

with γ being the Lorentz factor given in (3.4). The frequency transitions for a backward problem, with the incident wave on the right of the interface, in medium j, would be found by changing the signs of the superscripts, the sign of v_m and exchanging i and j in (3.26b).

Equations (3.26) are graphically represented in the inverse spacetime diagram of Fig. 3.6(a). The moving-frame axes k' and ω' are superimposed to the laboratory-frame axes k and ω. The slopes of the moving frame axes, which are v_f/c and c/v_f, from (3.10), are written in terms of the interface velocity by setting $v_\mathrm{f} = v_\mathrm{m}$. The dispersion relations $\omega_{i,j}^{\pm} = k_{i,j}^{\pm} v_{i,j}$ of the two involved media are plotted in the laboratory frame. To find the spectra of the scattered waves, we trace a curve parallel to the k_z' axis with intercept ω_e, and locate the spectra of the incident and scattered waves at the intersection of this curve and the dispersion diagrams. Reading out the spectra in the laboratory frame reveals that the reflected wave,

ψ_i^-, is downshifted while the transmitted wave, ψ_j^+, is upshifted, consistently with (3.26b) for $v_i > v_j$.

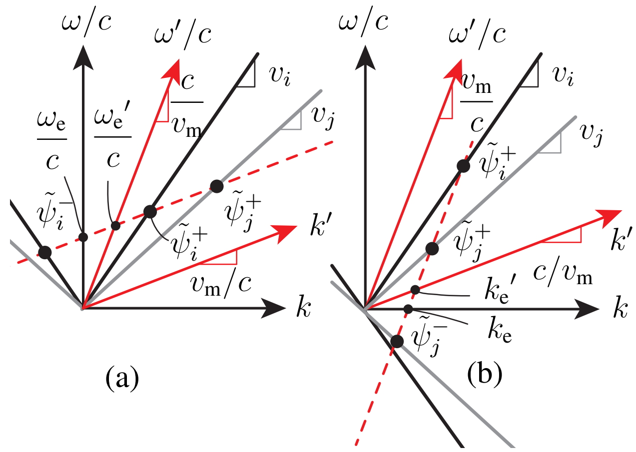

Figure 3.6 Frequency transitions at a spacetime interface corresponding to Fig. 3.2. (a) Subluminal case. (b) Superluminal case.

For the superluminal regime, we insert the moving-frame fields (3.14) into (3.20), and find the wavenumbers are conserved in the moving frame

$$k_e{}' = k_i^{+\prime} = k_j'^{+} = k_j'^{-}. \tag{3.28a}$$

where $k_e{}'$ is the conserved wavenumber.

Applying the wavenumber Lorentz transformation (3.10) to (3.28a), replacing the frame velocity by the modulation velocity through $v_m = c^2/v_f$ with $\omega_{i,j}^{\pm} = k_{i,j}^{\pm} v_{i,j}$ provides

$$k_e = k_i^+ \left(1 - \frac{v_i}{v_m}\right) = k_j^+ \left(1 - \frac{v_j}{v_m}\right) = k_j^- \left(1 + \frac{v_j}{v_m}\right). \tag{3.28b}$$

Dividing (3.28a) by (3.28b) gives the relation

$$k_e{}'/k_e = \gamma. \tag{3.29}$$

The frequency transitions for a backward problem, with the incident wave coming from the right, in medium i, would be found by changing the signs of the superscripts and the sign of v_m in (3.28b).

Equations (3.28) are represented graphically in Fig. 3.6(b). Once again, the axes of the moving frame and the laboratory frame are superimposed. The slopes of the moving frame, which are again v_f/c and c/v_f from (3.10), are written in terms of the interface velocity, v_m, by setting $v_\mathrm{f}/c = c/v_\mathrm{m}$. The dispersion curves of the two media are drawn, and the conservation of k' is enforced by tracing a line parallel to ω', with intercept k_e. The solutions are located at the intersections of this line and the dispersion diagram of medium j, remembering that both scattered waves are in medium j. Reading out the solutions in the laboratory frame reveals that both waves are downshifted, with ψ_j^- having a negative frequency, associated with time-reversal. As a consequence of time reversal, the wave reflected from a purely temporal interface is refocused to its source [26, 107] and the wave reflected from a superluminal interface is refocused to a shifted position [47].

The results of this section are summarized in Tab. 3.2.

Table 3.2 Summary of the scattering formulas, derived in Sec. 3.3, for a spacetime interface.

Subluminal	Superluminal
Coefficients (Fig. 3.2)	
$\tau_{ji} \overset{(3.18b)}{=} \dfrac{2\eta_j}{\eta_i+\eta_j}\left(\dfrac{1-\alpha_i}{1-\alpha_j}\right)$	$\xi_{ji} \overset{(3.22b)}{=} \dfrac{\eta_i+\eta_j}{2\eta_i}\left(\dfrac{1-\alpha_i}{1-\alpha_j}\right)$
$\gamma_{iji} \overset{(3.18a)}{=} \dfrac{\eta_j-\eta_i}{\eta_i+\eta_j}\left(\dfrac{1-\alpha_i}{1+\alpha_i}\right)$	$\zeta_{ji} \overset{(3.22a)}{=} \dfrac{\eta_i-\eta_j}{2\eta_i}\left(\dfrac{1-\alpha_i}{1+\alpha_j}\right)$
Frequencies (Fig. 3.6)	
$\omega_i^- \overset{(3.26b)}{=} \omega_i^+\dfrac{1-\alpha_i}{1+\alpha_i}$	$k_j^- \overset{(3.28b)}{=} k_i^+\dfrac{1-1/\alpha_j}{1+1/\alpha_i}$
$\omega_j^+ \overset{(3.26b)}{=} \omega_i^+\dfrac{1-\alpha_i}{1-\alpha_j}$	$k_j^+ \overset{(3.28b)}{=} k_i^+\dfrac{1-1/\alpha_i}{1-1/\alpha_i}$
$\alpha_{i,j} = v_\mathrm{m}/v_{i,j}$	

3.4 Spacetime Slab

Scattering Phenomenology

Noting that the succession of two interfaces corresponds to a slab, we can now address the slab problem upon the basis of Sec. 3.3. Figure 3.7 shows the multiple-reflections that occur in sub- and superluminal spacetime slabs. The slabs consist of a medium j sandwiched between media i and k, with media i and k sharing the same parameters. The two interfaces bounding the slab propagate at the same velocity and are thus parallel in the spacetime diagram. The slabs are illuminated by a wave incident from medium i.

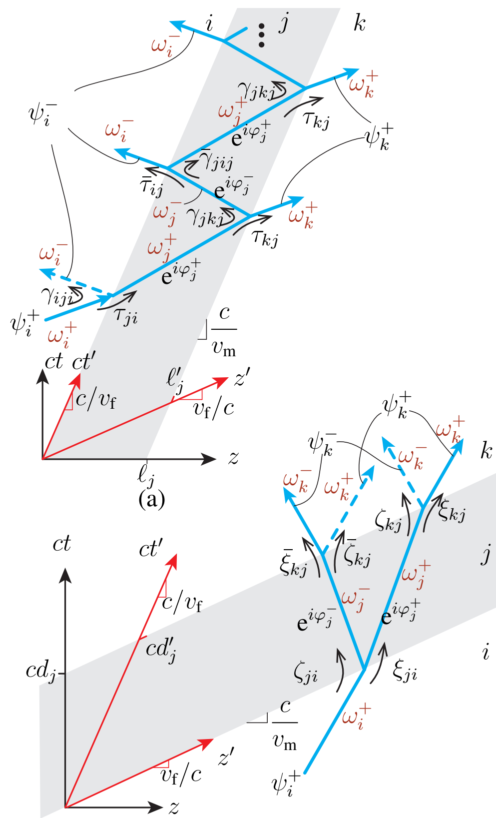

Figure 3.7 Multiple-reflection description of the scattering phenomenology in spacetime slabs. Changes in line type (solid $\leftrightarrow$ dashed) denote phase reversals. (a) Subluminal slab, with phase change occurring upon reflection to a lower impedance medium ($\eta_j < \eta_i$), according to (E.2). Note that the slope of the trajectories have been altered for representation convenience. (b) Superluminal slab, with phase change occurring upon reflection to a higher impedance medium ($\eta_k > \eta_j$), according to (E.3).

The multiple reflections in the subluminal case, represented in Fig. 3.7(a), and superluminal case, represented in Fig. 3.7(b) are strikingly different. In the subluminal case, the incident wave is divided into a reflected and a transmitted wave at the first interface. The transmitted wave propagates to the second interface, where it splits into new reflected and transmitted waves, with the former traveling back to the first interface, where it splits again in two parts, while the latter reaches the other side of the slab. This process repeats indefinitely, with the amplitudes of the exiting waves decreasing at each round trip. The transmitted wave, ψ_k^+ and the reflected wave, ψ_i^-, are found by summing the infinite contributions.

For the superluminal case, represented in Fig. 3.7(b), the wave incident from medium i splits into a later forward and a later backward wave at the first interface. The two waves propagate then to the second interface, where they split again. However, there is no further scattering, so that the total later forward and later backward waves, ψ_k^+ and ψ_k^-, are the sum of only four contributions.

We next calculate the frequency transitions and the phase shifts in the spacetime slabs, to later calculate the amplitudes of the scattered waves.

Frequency Transitions

Let us start with the subluminal slab. The frequencies, indicated in Fig. 3.7(a), are calculated by noting, as in (3.26a), that the frequencies in the moving frame are conserved, and are all equal to ω_e', i.e.,

$$\omega_\mathrm{e}{}' = \omega_i^+{}' = \omega_i^-{}' = \omega_j^+{}' = \omega_j^-{}' = \omega_k^+{}'. \tag{3.30}$$

Applying the frequency Lorentz transformation in (3.10), we obtain the same result as in (3.26b), but with the additional frequencies ω_j^- and ω_k^+ scattered from the second interface

$$\begin{aligned}\omega_\mathrm{e} = \omega_i^+ \left(1 - \frac{v_\mathrm{m}}{v_i}\right) = \omega_i^- \left(1 + \frac{v_\mathrm{m}}{v_i}\right) = \omega_j^+ \left(1 - \frac{v_\mathrm{m}}{v_j}\right)\\ = \omega_j^- \left(1 + \frac{v_\mathrm{m}}{v_j}\right) = \omega_k^+ \left(1 - \frac{v_\mathrm{m}}{v_k}\right).\end{aligned} \tag{3.31}$$

Equation (3.31) reveals that when media i and k share the same parameters, the wave transmitted through the slab has the same frequency as the incident wave, $\omega_k^+ = \omega_i^+$: it is upshifted to ω_j^+ at the first interface and then downshifted by the same amount at the second interface.

In the superluminal case, the frequencies, indicated in Fig. 3.7(b), are calculated by noting, as in (3.28a), that the wavenumbers in the moving frame are conserved and are all equal to k_e, i.e.,

$$k_\mathrm{e}' = k_i^+{}' = k_j^+{}' = k_j^-{}' = k_k^+{}' = k_k^-{}'. \tag{3.32}$$

Applying the wavenumber Lorentz transformation (3.10), these equalities are expressed in the laboratory frame as

$$\begin{aligned}k_\mathrm{e} = k_i^+ \left(1 - \frac{v_i}{v_\mathrm{m}}\right) = k_j^+ \left(1 - \frac{v_j}{v_\mathrm{m}}\right) = k_j^- \left(1 + \frac{v_j}{v_\mathrm{m}}\right)\\ = k_k^+ \left(1 - \frac{v_k}{v_\mathrm{m}}\right) = k_k^- \left(1 + \frac{v_k}{v_\mathrm{m}}\right).\end{aligned} \tag{3.33}$$

Equations (3.33) reveal that the later forward wave, ψ_k^+, has the same wavenumber as the incident wave, ψ_i^+, i.e. $k_k^+ = k_i^+$, if media i and k share the same parameters.

Phase Shift

We start, as usual, with the subluminal case. In the moving frame, where the slab appears stationary, the phase shift of the forward and backward waves is

$$\varphi_j^{\pm\prime} = k_j^{\pm\prime}\ell_j' = \frac{\omega_\mathrm{e}'}{v_j^{\pm\prime}}\ell_j', \tag{3.34}$$

where ℓ_j' is the length of the slab in the moving frame, as shown in Fig. 3.7(a), and the second equality was found by using the dispersion relation $k_j^{\pm\prime} = \omega_j^{\pm\prime}/v_j^{\pm\prime} = \omega_\mathrm{e}'/v_j^{\pm\prime}$, from frequency conservation (3.30) and with v_j' the phase velocity in the moving frame. We decompose this phase shift as

$$\varphi_j^{\pm\prime} = \bar{\varphi}_j' \pm \Delta\varphi_j', \tag{3.35a}$$

with the average and difference parts

$$\bar{\varphi}_j' = \frac{\varphi_j^{+\prime} + \varphi_j^{-\prime}}{2} \quad \text{and} \quad \Delta\varphi_j' = \frac{\varphi_j^{+\prime} - \varphi_j^{-\prime}}{2}, \tag{3.35b}$$

where the bar should not be confused with the bar for the scattering coefficients of the backward problem. Using (3.34), these average and difference parts may be written as

$$\bar{\varphi}_j' = \frac{{\omega_\mathrm{e}}'\ell_j'}{2}\left(\frac{1}{v_j^{+\prime}} + \frac{1}{v_j^{-\prime}}\right), \tag{3.36a}$$

$$\Delta\varphi_j' = \frac{{\omega_\mathrm{e}}'\ell_j'}{2}\left(\frac{1}{v_j^{+\prime}} - \frac{1}{v_j^{-\prime}}\right). \tag{3.36b}$$

Let us now derive the laboratory-frame counterparts of (3.34) and (3.36). From phase invariance [Eq. (3.8)], $\varphi_j = \varphi_j'$, $\bar{\varphi}_j = \bar{\varphi}_j'$ and $\Delta\varphi_j = \Delta\varphi_j'$. The three primed variables ω_e', $v_j^{\pm\prime}$ and ℓ_j' in (3.34) and (3.36) may be converted to their unprimed counterparts using respectively ${\omega_\mathrm{e}}' = \gamma\omega_\mathrm{e}$ (Eq. (3.27)), the equation for $v_j^{\pm\prime}$ in (3.15), and the length contraction formula

$$\ell_j' = \gamma\ell_j, \tag{3.37}$$

where the lengths ℓ_j and ℓ_j' are indicated in Fig. 3.7(a) to corresponds to the spatial separation between the two parallel lines separating the slab. Relation (3.37) is obtained by setting $z' = \ell_j'$, $z = \ell_j$ and $ct = 0$ in the left expression of (3.3). Applying the three substitutions results in the phase shift counterpart of (3.34)

$$\varphi_j^{\pm} = \gamma^2 \omega_{\mathrm{e}} \ell_j \frac{1 \mp v_{\mathrm{m}} v_j / c^2}{v_j \mp v_{\mathrm{m}}}, \tag{3.38a}$$

and the average and difference phase counterparts of (3.36)

$$\bar{\varphi}_j = \omega_{\mathrm{e}} \frac{\ell_j v_j}{v_j^2 - v_{\mathrm{m}}^2}, \tag{3.38b}$$

$$\Delta\varphi_j = \omega_{\mathrm{e}} \ell_j \gamma^2 v_{\mathrm{m}} \frac{1 - v_j^2/c^2}{v_j^2 - v_{\mathrm{m}}^2}. \tag{3.38c}$$

For the case of the superluminal slab, the phase shift of the forward and backward waves is found by inserting (3.14) into (3.20)

$$\varphi_j^{\pm\prime} = \omega_j^{\pm\prime} d_j' = k_{\mathrm{e}}' v_j^{\pm\prime} d_j'. \tag{3.39a}$$

with d_j' is the duration in the moving frame, drawn in Fig. 3.7(b). Expressing the phase shift in the form of an average and a difference, as in (3.35a), we find

$$\bar{\varphi}_j' = \frac{k_{\mathrm{e}}' d_j'}{2} \left(v_j^{+\prime} + v_j^{-\prime} \right), \tag{3.39b}$$

$$\Delta\varphi_j' = \frac{k_{\mathrm{e}}' d_j'}{2} \left(v_j^{+\prime} - v_j^{-\prime} \right). \tag{3.39c}$$

The superluminal results (3.39) are expressed in terms of laboratory-frame quantities by replacing $k_{\mathrm{e}}' = \gamma k_{\mathrm{e}}$ [Eq. (3.29)], the equation for $v_j^{\pm\prime}$ in (3.15) in which we substitute $v_{\mathrm{f}} = c^2/v_{\mathrm{m}}$, and the duration

$$d_j' = \gamma d_j, \tag{3.40}$$

where d_j' and d_j are indicated in Fig. 3.7(b) to correspond to the time separation between the two parallel trajectories delimiting the slab. Equation (3.40) is obtained by setting $t' = d_j'$, $t = d_j$, and $z = 0$ in the right expression of (3.3). Note that (3.40) does not correspond to the time dilation equation (which would read $d_j' = \gamma^{-1} d_j$), since time dilation compares the time separation between two fixed events, whereas we are comparing the time separation between two trajectories. Applying the substitutions for k_{e}' $v_j^{\pm\prime}$ and d_j' into (3.39) yield the phase shift

$$\varphi_j^{\pm} = \gamma^2 k_{\mathrm{e}} d_j \frac{1 \mp c^2/(v_j v_{\mathrm{m}})}{1/v_j \mp 1/v_{\mathrm{m}}}, \tag{3.41a}$$

and the average and difference quantities

$$\bar{\varphi}_j = k_\mathrm{e} \frac{d_j v_j v_\mathrm{m}^2}{v_\mathrm{m}^2 - v_j^2}, \tag{3.41b}$$

$$\Delta\varphi_j = k_\mathrm{e} d_j \gamma^2 v_\mathrm{m} c^2 \frac{1 - v_j^2/c^2}{v_j^2 - v_\mathrm{m}^2}. \tag{3.41c}$$

Note that Eqs. (3.41) could have been alternatively found by applying the substitutions of Tab. 3.1 into (3.38).

Scattering Coefficients

For the subluminal case, the reflection coefficient for the forward problem is found by summing up the amplitude of the wave reflected at the first interface, the amplitude of the wave having traveled one round trip, the amplitude of the wave having traveled two round trips, and so on, which yields

$$\begin{aligned} \Gamma_{iki} = \frac{|\psi_i^-|}{|\psi_i^+|} &= \gamma_{iji} + \bar{\tau}_{ij}\gamma_{jkj}\tau_{ji}\mathrm{e}^{2i\bar{\varphi}} \\ &\quad + \bar{\tau}_{ij}\gamma_{jkj}\bar{\gamma}_{jij}\gamma_{jkj}\tau_{ji}\mathrm{e}^{4i\bar{\varphi}} \\ &\quad + \bar{\tau}_{ij}\gamma_{jkj}\left(\bar{\gamma}_{jij}\gamma_{jkj}\right)^2 \tau_{ji}\mathrm{e}^{6i\bar{\varphi}} \\ &= \gamma_{iji} + \bar{\tau}_{ij}\gamma_{jkj}\tau_{ji}\mathrm{e}^{2i\bar{\varphi}} \sum_{n=0}^{\infty} \left(\bar{\gamma}_{jij}\gamma_{jkj}\mathrm{e}^{2i\bar{\varphi}}\right)^n, \end{aligned} \tag{3.42}$$

which is the same expression as that for a stationary slab [117], but with the local generalized coefficients (E.2) and (3.19), and the phases $\bar{\varphi}_j$ in (3.38b). Since $\bar{\gamma}_{jij} < 1$ and $\gamma_{jkj} < 1$, the geometric series (3.42) reduces to

$$\Gamma_{iki} = \gamma_{iji} + \frac{\bar{\tau}_{ij}\gamma_{jkj}\tau_{ji}\mathrm{e}^{2i\bar{\varphi}_j}}{1 - \bar{\gamma}_{jij}\gamma_{jkj}\mathrm{e}^{2i\bar{\varphi}_j}} = \gamma_{iji}\frac{1 - \mathrm{e}^{2i\bar{\varphi}_j}}{1 - \bar{\gamma}_{jij}\gamma_{jkj}\mathrm{e}^{2i\bar{\varphi}_j}}, \tag{3.43}$$

where the second equality was obtained by using the generalized Stokes condition (3.24).

The transmission coefficient for the forward problem wave is found by summing the wave traveling through the slab, the wave reflected at the second interface and traveling one round trip, the wave traveling two round trips, and so on, i.e,

$$\begin{aligned}
T_{ki} = \frac{|\psi_k^+|}{|\psi_i^+|} =& \tau_{kj}\tau_{ji}\mathrm{e}^{i\varphi_j^+} \\
&+ \tau_{kj}\bar{\gamma}_{jij}\gamma_{jkj}\tau_{ji}\mathrm{e}^{i\varphi_j^+}\mathrm{e}^{2i\bar{\varphi}_j} \\
&+ \tau_{kj}\left(\bar{\gamma}_{jij}\gamma_{jkj}\right)^2\tau_{ji}\mathrm{e}^{i\varphi_j^+}\mathrm{e}^{2i\bar{\varphi}_j} \\
=& \tau_{kj}\tau_{ji}\mathrm{e}^{i\varphi_j^+}\sum_{n=0}^{\infty}\left(\bar{\gamma}_{jij}\gamma_{jkj}\mathrm{e}^{2i\bar{\varphi}_j}\right)^n \\
=& \frac{\tau_{kj}\tau_{ji}\mathrm{e}^{i\varphi_j^+}}{1-\bar{\gamma}_{jij}\gamma_{jkj}\mathrm{e}^{2i\bar{\varphi}_j}}.
\end{aligned} \tag{3.44}$$

The scattering coefficient extrema are found from (3.43) and (3.44) to correspond to $\bar{\varphi}_j = n\pi/2$, where n is an integer. For n odd, reflection is maximal and transmission is minimal, and conversely for n even.

The reflection and transmission coefficients for the backward problem are found by barring the unbarred coefficients, unbarring the barred coefficients and exchanging i and k. The phases $\bar{\varphi}_j$ are unchanged, since they correspond to the round trip phase, but the phases φ_j^+ are replaced by φ_j^-. Thus,

$$\bar{\Gamma}_{kik} = \frac{|\psi_k^+|}{|\psi_k^-|} = \bar{\gamma}_{kjk}\frac{1-\mathrm{e}^{2i\bar{\varphi}_j}}{1-\bar{\gamma}_{jij}\gamma_{jkj}\mathrm{e}^{2i\bar{\varphi}_j}} = \Gamma_{iki}\frac{\bar{\gamma}_{kjk}}{\gamma_{iji}}. \tag{3.45a}$$

$$\bar{T}_{ik} = \frac{|\psi_i^-|}{|\psi_k^-|} = \frac{\bar{\tau}_{ij}\bar{\tau}_{jk}\mathrm{e}^{i\varphi_j^-}}{1-\bar{\gamma}_{jj}\gamma_{jj}\mathrm{e}^{2i\bar{\varphi}_j}} = T_{ki}\mathrm{e}^{-i\Delta\varphi_j}. \tag{3.45b}$$

where the third equality in (3.45b) was found from a consequence of the Stokes relations (3.24c). Note that we are comparing forward and backward problems that have different incident frequencies, ω_i^+ and ω_i^- respectively, related through ω_e (3.31) as shown in Fig. 3.6(a).

In the superluminal case, the situation, although less usual, is simpler, since there are now only three scattering events. Reading out Fig. 3.7(b), we find the later backward and later forward coefficients

$$Z_{ki} = \frac{|\psi_k^-|}{|\psi_i^+|} = \zeta_{kj}\xi_{ji}\mathrm{e}^{i\varphi_j^+} + \bar{\xi}_{kj}\zeta_{ji}\mathrm{e}^{-i\varphi_j^-}, \tag{3.46a}$$

$$\Xi_{ki} = \frac{|\psi_k^+|}{|\psi_i^+|} = \xi_{kj}\xi_{ji}\mathrm{e}^{i\varphi_j^+} + \bar{\zeta}_{kj}\zeta_{ji}\mathrm{e}^{-i\varphi_j^-}. \tag{3.46b}$$

Applying the generalized Stokes relations for superluminal coefficients (3.25), (3.46) reduce to

$$Z_{ki} = \zeta_{kj}\xi_{ji}\mathrm{e}^{-i\varphi_j^-}\left(\mathrm{e}^{i\bar{\varphi}_j}-1\right), \tag{3.47a}$$

$$\Xi_{ki} = \mathrm{e}^{-i\varphi_j^-} \left(1 + \xi_{kj}\xi_{ji}\left(\mathrm{e}^{i\bar{\varphi}_j} - 1\right)\right). \tag{3.47b}$$

The scattering coefficient extrema are found from from (3.47) to correspond, again, to $\bar{\varphi}_j = n\pi/2$, with n an integer. For n even, both later forward and later backward coefficients are maximal, while for n odd, both coefficients are minimal.

The coefficients for the opposite incidence direction $\bar{Z}_{ki}$ and $\bar{\Xi}_{ki}$ are found by barring and unbarring unbarred and barred coefficients, respectively, and replacing the phase term φ_j^+ by φ_j^-:

$$\bar{Z}_{ki} = \frac{|\psi_k^-|}{|\psi_i^-|} = \bar{\zeta}_{kj}\bar{\xi}_{ji}\mathrm{e}^{-i\varphi_j^+}\left(\mathrm{e}^{i\bar{\varphi}_j} - 1\right) = Z_{ki}\frac{\bar{\zeta}_{kj}\bar{\xi}_{ji}}{\zeta_{kj}\xi_{ji}}\mathrm{e}^{i\Delta\varphi_j}, \tag{3.48a}$$

$$\bar{\Xi}_{ki} = \frac{|\psi_k^+|}{|\psi_i^-|} = \mathrm{e}^{-i\varphi_j^+}\left(1 + \bar{\xi}_{kj}\bar{\xi}_{ji}\left(\mathrm{e}^{i\bar{\varphi}_j} - 1\right)\right) = \Xi_{ki}\mathrm{e}^{-i\Delta\varphi_j}. \tag{3.48b}$$

Were again (3.48) compares the coefficients for the forward and the backward problems having different incident wavenumbers, k_i^+ and k_i^- respectively, related through k_e (3.33) as represented in Fig. 3.6(b).

Interference Condition

The extrema of the scattering coefficients, which were just previously derived, are now analysed in terms of Bragg-like interference conditions, with the help of Fig. 3.8.

In the subluminal case, constructive interference occurs in reflection and destructive interference occurs in transmission. The interference condition may be found geometrically by recognizing the triangle with slopes c/v_m and c/v_j has a total length ℓ_j related to the period of the wave T_j^+ through

$$\ell_j = \frac{cT_j^+}{4}\left(\frac{v_\mathrm{m}}{c} + \frac{v_j}{c}\right) = \frac{\lambda_j^+}{4}(1 + v_\mathrm{m}/v_j), \tag{3.49}$$

where the second equality is found by using $T_j^+ = \lambda_j^+/v_j$. This can be seen as a generalization of the quarter-wave condition. Inserting (3.49) and the definition of ω_e (3.31) into (3.38b) retrieves $\bar{\varphi}_j = \pi/2$.

In the superluminal case, shown in Fig. 3.8(b), constructive interference occurs for both the later forward and later backward components. The interference condition may be found geometrically by studying the shaded triangle and noticing the total duration cd_j is related

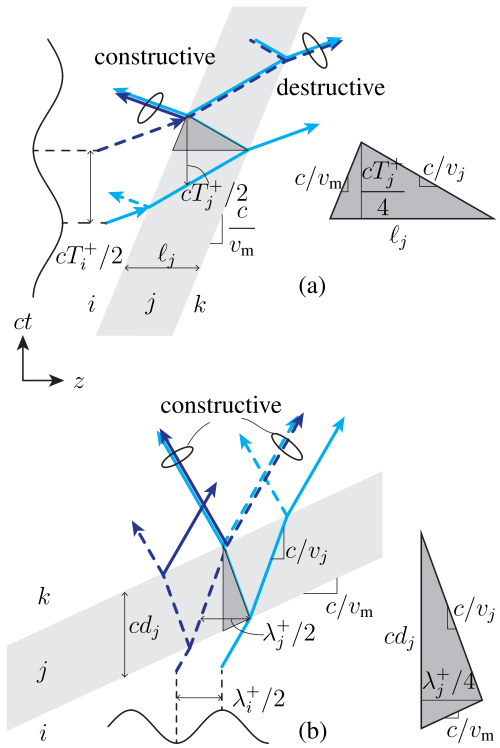

Figure 3.8 Graphical Bragg-like interference argument. The light and dark blue trajectories correspond to the maxima and minima of the incident wave, and changes in line type (solid $\leftrightarrow$ dashed) denote phase reversals. (a) Subluminal case, with constructive and destructive interference in reflection and transmission, respectively. Note that the slope of the trajectories have been altered for representation convenience. (b) Superluminal case, with constructive interference in both the later forward and later backward waves.

to the slopes of the triangle, c/v_m and c/v_j and to the wavelength $\lambda_j^+/4$ through

$$cd_j = \frac{\lambda_j^+}{4}\left(\frac{c}{v_j} + \frac{c}{v_\mathrm{m}}\right) = \frac{cT_j^+}{4}(1 + v_j/v_\mathrm{m}), \tag{3.50}$$

where $\lambda_j^+ = v_j T_j^+$ was used. Inserting (3.50) and the definition of k_e, (3.33), into (3.39b) retrieves $\bar{\varphi}_j = \pi/2$.

The spacetime slab results are summarized in Tab. 3.3.

3.5 Unbounded Bilayer Crystal

We now move on to the study of bilayer crystals, whose periodic unit cell is composed of a pair of slabs, or layers, as presented in Fig. 3.9.

Table 3.3 Summary of spacetime slab results.

Subluminal regime	Superluminal regime
Phase (Fig. 3.7)	
$\varphi_j^{\pm\prime} \overset{(3.35a)}{=} \bar{\varphi}_j' \pm \Delta\varphi_j'$	
$\bar{\varphi}_j \overset{(3.38b)}{=} \omega_\mathrm{e}\ell_j \dfrac{v_j}{v_j^2 - v_\mathrm{m}^2}$	$\bar{\varphi}_j \overset{(3.41b)}{=} k_\mathrm{e} d_j \dfrac{v_j v_\mathrm{m}^2}{v_j^2 - v_\mathrm{m}^2}$
$\Delta\varphi_j \overset{(3.38c)}{=} \dfrac{\bar{\varphi}_j\gamma^2(1 - v_j^2/c^2)v_\mathrm{m}}{v_j}$	$\Delta\varphi_j \overset{(3.41c)}{=} \dfrac{\bar{\varphi}_j\gamma^2(1 - v_j^2/c^2)c^2}{v_j v_\mathrm{m}}$
Coefficients (Fig. 3.7)	
$\Gamma_{iki} \overset{(3.42)}{=} \gamma_{iji} \dfrac{1 - \mathrm{e}^{2i\bar{\varphi}_j}}{1 - \bar{\gamma}_{jij}\gamma_{jkj}\mathrm{e}^{2i\bar{\varphi}_j}}$	$Z_{ki} \overset{(3.47)}{=} \zeta_{kj}\xi_{ji}\mathrm{e}^{-i\varphi_j^-}\left(\mathrm{e}^{i\bar{\varphi}_j} - 1\right)$
$T_{ki} \overset{(3.44)}{=} \dfrac{\tau_{kj}\tau_{ji}\mathrm{e}^{i\varphi_j^+}}{1 - \bar{\gamma}_{jij}\gamma_{jkj}\mathrm{e}^{2i\bar{\varphi}_j}}$	$\Xi_{ki} \overset{(3.47)}{=} \left(1 + \xi_{kj}\xi_{ji}\left(\mathrm{e}^{i\bar{\varphi}_j} - 1\right)\right)\mathrm{e}^{-i\varphi_j^-}$
Bragg Interference Condition(Fig. 3.8)	
$\ell_j \overset{(3.49)}{=} \dfrac{\lambda_j^+}{4}(1 + \dfrac{v_\mathrm{m}}{v_j})$	$d_j \overset{(3.50)}{=} \dfrac{T_j^+}{4}(1 + \dfrac{v_j}{v_\mathrm{m}})$

Linear Approximation of Dispersion Diagram

Crystals are largely described by their dispersion diagrams, which consist in periodic alternances of passbands and stopbands, or bandgaps. The bandgaps are produced by the constructive or destructive interference of the wave scattered by the crystal, as described in Sec. 3.4 for the particular case of a slab. Away from these bandgaps, the waves are transmitted through the crystal without attenuation or amplification, and they undergo little dispersion.

Before presenting the exact construction of the dispersion diagrams, whose complexity occults some of the physics of the problem, we shall derive a simple and useful linear approximation of the exact solution. This approximation consists of a diamond-like grid that coincides with the exact diagram away from the gaps and whose nodes correspond to the exact bandgap centers, as will be shown in Sec. 3.5.

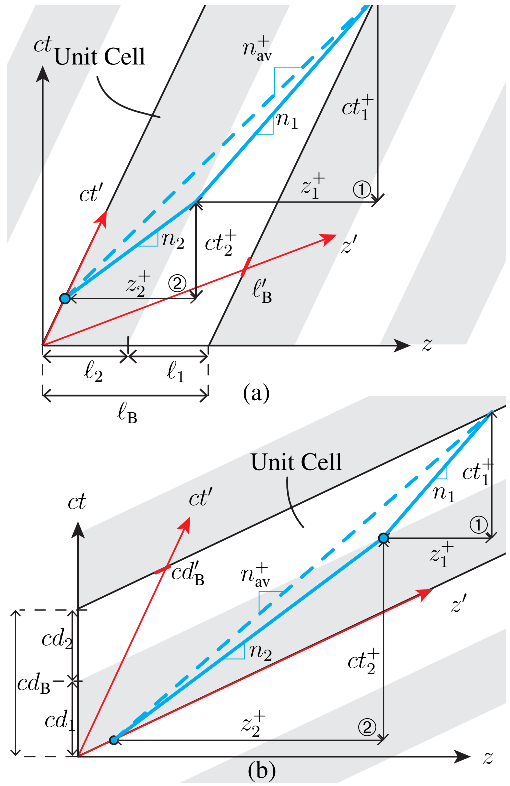

Figure 3.9 Bilayer spacetime crystal with spacetime unit cell and out-of-gap wave trajectories. (a) Subluminal equal-length crystal, with $\ell_1 = \ell_2$. The slopes of the triangles ① and ② are $n_1 = ct_1^+/z_1^+$ and $n_2 = ct_2^+/z_2^+$, so that $z_1^+ = ct_1^+/n_1$ and $z_2 = ct_2^+/n_2$. Substituting these lengths into the expression for the slope $n_{\text{av}} = (ct_1^+ + ct_2^+)/(z_1^+ + z_2^+)$, yields (3.51). (b) Superminal equal-duration crystal, with $d_1 = d_2$. From the slopes of the triangles ① and ②, given in (a), we have $ct_1^+ = z_1^+ n_1$ and $ct_2 = z_2^+ n_2$. Substituting these durations into the expression for the average slope, also given in (a), yields (3.55).

Average Velocity

The slopes of the curves in the dispersion diagram of Fig. 3.10 correspond to the average group velocities, which are inversely proportional to the average refractive indices, $v_{\text{av}}^{\pm} = c/n_{\text{av}}^{\pm}$. As the approximation is only valid far from the bandgaps, these average refractive indices are only valid in the absence of reflection. The average indices may be found geometrically with the help of Fig. 3.9 as the slopes of the straight segments connecting the entering and exiting points of the trajectory through the crystal unit cell. This leads to expressions for the average velocities in terms of the refractive indices with weights corresponding to the time spent or distance traveled by the wave in each medium, as shown in Fig. 3.9.

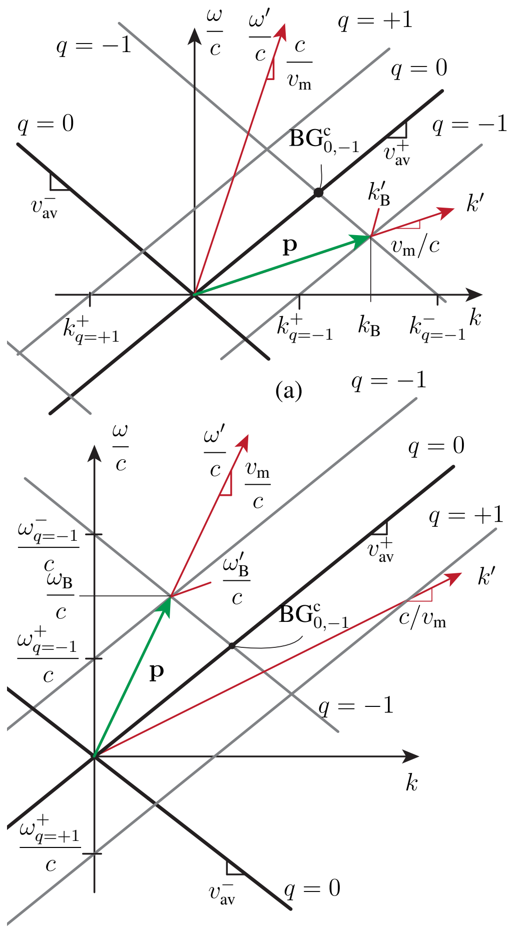

Figure 3.10 Linear approximation of the dispersion diagram of bilayer crystals with $n_2/n_1 = 1.5$ and equal electrical lengths. (a) Subluminal case, with $v = (1/3)c$. (b) Superluminal case, with $v = 2c$.

In the subluminal case, represented in Fig. 3.9(a), the average index is found as

$$n^\pm_\mathrm{av} = \frac{t^\pm_1 + t^\pm_2}{t^\pm_1/n_1 + t^\pm_2/n_2} \tag{3.51}$$

where the superscript refers to the $\pm z$ wave direction, and where the terms $d^\pm_{1,2}$ correspond to the duration of the wave travels in layers $1, 2$ in the $\pm$ direction. This average index may be more conveniently written in terms the layer lengths, $\ell_{1,2}$. For this purpose, we express the durations in terms of these lengths, derived in App. A as

$$t^\pm_{1,2} = \frac{\ell_{1,2} n_{1,2}/c}{1 \mp v_\mathrm{m} n_{1,2}/c}, \tag{3.52}$$

and insert this relation into (3.51), which yields

$$n_{\mathrm{av}}^{\pm} = \frac{n_1\ell_1 + n_2\ell_2 \mp v_{\mathrm{m}} n_1 n_2/c(\ell_1 + \ell_2)}{\ell_1 + \ell_2 \mp v_{\mathrm{m}}/c\,(n_2\ell_1 + n_1\ell_2)}. \tag{3.53}$$

It is also useful, for later use, to write the expression of the average velocity $v_{\mathrm{av}}^{\pm} = c/n_{\mathrm{av}}$ in terms of the velocities in the two media, i.e.,

$$v_{\mathrm{av}}^{\pm} = \frac{v_1 v_2\,(\ell_1 + \ell_2) \mp v_{\mathrm{m}}\,(\ell_1 v_1 + \ell_2 v_2)}{(\ell_1 v_2 + \ell_2 v_1) \mp v_{\mathrm{m}}\,(\ell_1 + \ell_2)}. \tag{3.54}$$

In the superluminal case, represented in Fig. 3.9(b), the average index is found as

$$n_{\mathrm{av}}^{\pm} = \frac{z_1^{\pm} n_1 + z_2^{\pm} n_2}{z_1^{\pm} + z_2^{\pm}}, \tag{3.55}$$

where the quantities $z_{1,2}^{\pm}$ correspond to the length traveled by the wave in the $\pm$ direction in layers $1, 2$. The average index may be more conveniently written in terms the layer durations $d_{1,2}$. For this purpose, we express the lengths in terms of these durations, derived in App. A, as

$$z_{1,2}^{\pm} = \frac{c d_{1,2}}{n_{1,2} \mp c/v_{\mathrm{m}}}, \tag{3.56}$$

and insert this relation into (3.55), which yields

$$n_{\mathrm{av}}^{\pm} = \frac{d_1 + d_2 \mp c/v_{\mathrm{m}}(d_1/n_2 + d_2/n_1)}{d_1/n_1 + d_2/n_2 \mp c/(v_{\mathrm{m}} n_1 n_2)(d_1 + d_2)}. \tag{3.57}$$

It is also useful, for later use, to write the expression of the average velocity in terms of the velocities in the two media, i.e.,

$$v_{\mathrm{av}}^{\pm} = \frac{v_{\mathrm{m}}(d_1 v_1 + d_2 v_2) \mp v_1 v_2 (d_1 + d_2)}{v_{\mathrm{m}}(d_1 + d_2) \mp (d_1 v_2 + d_2 v_1)}. \tag{3.58}$$

Note that (3.57) and (3.58) could have been alternatively found by applying the substitutions of Tab. 3.1 to (3.53) and (3.54).

Table 3.4 lists the forward and backward average refractive indices at special velocity points for unit cells of equal layer length or equal layer duration. The first row gives the average indices for the purely spatial regime, found by setting $v_{\mathrm{m}} = 0$ in (3.53). These indices are found to be the same for forward or backward waves, and are the arithmetic average of the two indices.

The second row provides the average indices for the upper limit of the subluminal regime (or lower limit of the interluminal regime, see Sec. 3.2), and are found by setting $v_\mathrm{m} = c/n_2$ in (3.53). The forward average index reduces to n_2, since the wave has the same velocity as the modulation, and therefore never exits the layer of refractive index n_2. The backward wave travels across both media, so that the average index is a function of the two refractive indices.

The third row corresponds to the superluminal lower limit (or upper limit of the interluminal regime, see Sec. 3.2) and is found by setting $v_\mathrm{m} = c/n_1$ in (3.57). Now, the forward average index reduces to n_1 since the wave remains in medium n_1 while the backward index is the same function as in the previous case with exchanged indices.

The fourth row provides the indices for the purely temporal limit, found by setting $v_\mathrm{m} = \infty$ in (3.57). The average indices for forward and backward waves are again equal, as is expected since the structure is symmetric in space. Now the inverse of the average index is the arithmetic average of the inverses of two indices, reminiscent of a parallel circuit form. The series and parallel circuit forms of the spatial and temporal average indices are akin to the polarization-dependent form of the average indices in hyperbolic media [118].

Table 3.4 Average refractive index for different modulation velocities, from (3.53), with $\ell_1 = \ell_2$ (upper half) and (3.57), with $d_1 = d_2$ (lower half).

Modulation regime	**Velocity** ($v_\mathbf{m}$)	**Average index** ($n^+_\mathbf{av}$)	**Average index** ($n^-_\mathbf{av}$)
spatial	0	$\frac{1}{2}(n_1+n_2)$	$\frac{1}{2}(n_1+n_2)$
subluminal upper limit	$v_2 = \frac{c}{n_2}$	n_2	$n_2\frac{3n_1+n_2}{n_1+3n_2}$
superluminal lower limit	$v_1 = \frac{c}{n_1}$	n_1	$n_1\frac{3n_2+n_1}{n_2+3n_1}$
temporal	∞	$\frac{1}{2}\left(\frac{1}{n_1}+\frac{1}{n_2}\right)^{-1}$	$\frac{1}{2}\left(\frac{1}{n_1}+\frac{1}{n_2}\right)^{-1}$

Dispersion Diagram Period

The first pair of dispersion curves in Fig. 3.10 (solid lines), $\omega = \pm v_{\text{av}}^{\pm} k$, has its intercept at the origin, while the other pairs of curves are (obliquely) translated from this first pair by $q\mathbf{p} = q(k_{\text{B}}, \omega_{\text{B}})$, where q is the integer representing the pair of curves, $\mathbf{p}$ is the spacetime period and k_{B} and ω_{B} are the wavenumber and frequency translation quantities.

In the subluminal case, the spacetime period vector is found by recalling that the crystal is stationary in the moving frame, so that the period is simply

$$\mathbf{p}' = (k'_{\text{B}}, 0) = \left(\frac{2\pi}{\ell'_{\text{B}}}, 0\right). \tag{3.59}$$

This period is expressed in terms of laboratory-frame quantities by first applying the wavenumber Lorentz transformations $k'_{\text{B}} = k_{\text{B}}/\gamma$ and $k'_{\text{B}} = \omega_{\text{B}}/(v_{\text{m}}\gamma)$, which are found by setting $k' = k'_{\text{B}}$, $\omega' = 0$, $k = k_{\text{B}}$ and $\omega = \omega_{\text{B}}$ in (3.10) with $v_{\text{f}} = v_{\text{m}}$ (Sec. 3.2), and next applying the length contraction $\ell'_{\text{B}} = \gamma \ell_{\text{B}}$ (as in Eq. (3.37), replacing ℓ_j, ℓ'_j by $\ell_{\text{B}}, \ell'_{\text{B}}$), so that

$$k_{\text{B}} = \frac{2\pi}{\ell_{\text{B}}}, \qquad \omega_{\text{B}} = \frac{2\pi v_{\text{m}}}{\ell_{\text{B}}}, \tag{3.60}$$

which may be alternatively obtained from Bloch-Floquet theory.

In the superluminal case, the spacetime period vector is

$$\mathbf{p}' = (0, \omega'_{\text{B}}) = \left(0, \frac{2\pi}{d'_{\text{B}}}\right). \tag{3.61}$$

As for the subluminal case, we express this period into laboratory frame quantities by first applying the frequency transformations $\omega'_{\text{B}} = \omega_{\text{B}}/\gamma$ and $\omega'_{\text{B}} = k_{\text{B}}/(\gamma v_{\text{f}}/c^2) = k_{\text{B}} v_{\text{m}}/\gamma$, which are found by setting $\omega' = \omega'_{\text{B}}$, $k' = 0$, $k = k_{\text{B}}$, and $\omega = \omega_{\text{B}}$ in (3.10) with $v_{\text{f}} = c^2/v_{\text{m}}$ (Sec. 3.2). We then apply the time contraction $d'_{\text{B}} = d_{\text{B}}/\gamma$, as in (3.40), replacing d_j, d'_j by $d_{\text{B}}, d'_{\text{B}}$, and this gives

$$\omega_{\text{B}} = \frac{2\pi}{d_{\text{B}}}, \qquad k_{\text{B}} = \frac{2\pi}{v_{\text{m}} d_{\text{B}}}. \tag{3.62}$$

For both the subluminal and the superluminal cases, we may write the equations for the pairs of curves forming the linear approximation grid as

$$\omega + q\omega_{\text{B}} = \pm v_{\text{av}}^{\pm}(k + qk_{\text{B}}), \tag{3.63}$$

so that Fig. 3.10 may be simply plotted from $v_{\text{av}}^{\pm}$ derived in Sec. 3.5 along with the just derived translation quantities.

Bandgap Center Position

The bandgap centers are located at the nodes of the linear approximation grid we have just derived. The bandgap center $\mathrm{BG}^{\mathrm{c}}_{0,-1}$ is indicated in Fig. 3.10 at the intersection of curves $q = 0$ and $q = -1$, where the superscript c refers to the center of the bandgap.

Let us start with the subluminal case. We first derive the k-intercepts of the curves $\omega = v^{\pm}_{\mathrm{av}}(k-k^{\pm}_{q})$, with $k^{\pm}_{q}$ being the k-intercepts of the forward-wave and backward-wave solutions, found by setting $\omega = 0$ in (3.63) as

$$k^{\pm}_{q} = \frac{q\omega_{\mathrm{B}}}{\pm v^{\pm}_{\mathrm{av}}} - qk_{\mathrm{B}} = qk_{\mathrm{B}}\left(\frac{v_{\mathrm{m}}}{\pm v^{\pm}_{\mathrm{av}}} - 1\right), \tag{3.64}$$

where the second equation in (3.64) was found using (3.60)

The position of bandgap $\mathrm{BG}_{0,-1}$ is then found by intersecting the curves representing the two relevant modes, i.e. setting $\omega = v^{+}_{\mathrm{av}}k = -v^{-}_{\mathrm{av}}(k - k^{-}_{q=-1})$. Inserting (3.64) into this intersection condition results in the bandgap center position

$$k^{\mathrm{c}}_{0,-1} = \frac{v_{\mathrm{m}} + v^{-}_{\mathrm{av}}}{v^{+}_{\mathrm{av}} + v^{-}_{\mathrm{av}}}k_{\mathrm{B}}. \tag{3.65}$$

The other bandgap centers are found by a similar procedure. This relation reduces to the coupled-mode result [119, 120] under the approximation $v^{+}_{\mathrm{av}} = v^{-}_{\mathrm{av}}$.

For the superluminal regime, we first calculate the ω-intercepts of the forward and backward curve of each mode. These intercepts are found by setting $k = 0$ in (3.63), which yields

$$\omega^{\pm}_{q} = \pm qk_{\mathrm{B}}v^{\pm}_{\mathrm{av}} - q\omega_{\mathrm{B}} = q\omega_{\mathrm{B}}\left(\frac{\pm v^{+}_{\mathrm{av}}}{v_{\mathrm{m}}} - 1\right), \tag{3.66}$$

with the second equality again obtained using (3.62). From these intercepts, we find the intersection position of the bandgap $\mathrm{BG}_{0,-1}$ by intersecting the two curves as $k = \omega/v^{+}_{\mathrm{av}} = -(\omega - \omega^{\mathrm{b}}_{q=-1})/v^{-}_{\mathrm{av}}$, which yields

$$\omega^{\mathrm{c}}_{0,-1} = \frac{v^{+}_{\mathrm{av}}}{v_{\mathrm{m}}}\frac{v^{-}_{\mathrm{av}} + v_{\mathrm{m}}}{v^{-}_{\mathrm{av}} + v^{+}_{\mathrm{av}}}\omega_{\mathrm{B}}, \tag{3.67}$$

which reduce to the coupled-mode results [121] under the approximation $v^{+}_{\mathrm{av}} = v^{-}_{\mathrm{av}}$. The other bandgap centers are again found by a similar procedure.

Unit-Cell Tranfer Matrix

We now calculate the transfer matrix of a unit cell, extending the classical transfer matrix of stationary structures [122], with the help of Fig. 3.11. Note that this graph corresponds, for later illustration convenience, to the particular design of an equal-phase crystal, where the forward and backward round-trip trajectories emerge at the same spacetime point. By definition, the transfer matrix relates the fields in media i and k at the interfaces $I_{i,j}$ and $I_{k,l}$ as

$$\begin{bmatrix} \psi_k^+ \\ \psi_k^- \end{bmatrix}_{I_{k,l}} = [M_\mathrm{B}] \begin{bmatrix} \psi_i^+ \\ \psi_i^- \end{bmatrix}_{I_{i,j}}, \tag{3.68}$$

where the two interfaces separate layers i, j and k, l, respectively, as shown in Fig. 3.11.

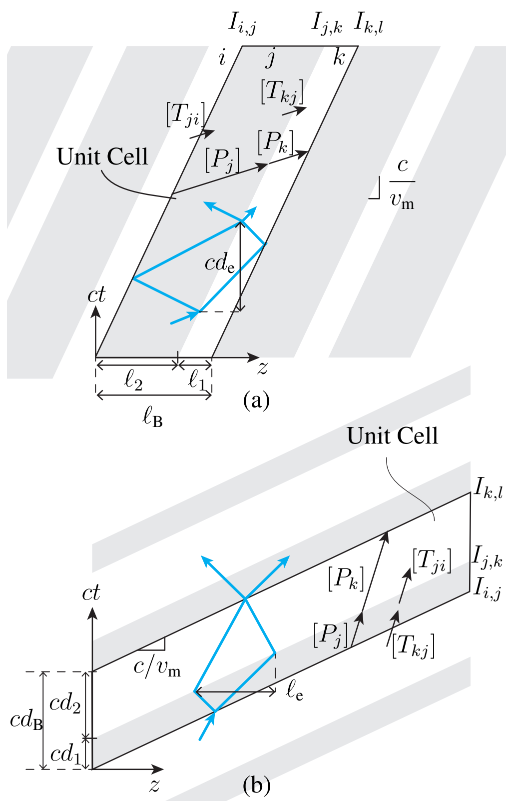

Figure 3.11 Bilayer spacetime crystal with spacetime unit cell. (a) Subluminal regime. b) Superminal regime.

The unit-cell matrix is found by multiplying interface matrices, $[T_{ji}]$ and propagation matrices, $[P_j]$, according to Fig. 3.11, i.e.,

$$[M_\mathrm{B}] = [P_k]\,[T_{kj}]\,[P_j]\,[T_{ji}]\,. \tag{3.69}$$

We first calculate the interface matrix, $[T_{m,m-1}]$, which relates the fields at both sides of the interface $I_{m,m-1}$. At the first interface of the unit cell, we have

$$\begin{bmatrix} \psi_j^+ \\ \psi_j^- \end{bmatrix}_{I_{i,j}} = [T_{ji}] \begin{bmatrix} \psi_i^+ \\ \psi_i^- \end{bmatrix}_{I_{i,j}} . \tag{3.70}$$

The interface matrix may be computed using the results of Sec. 3.3 for interface scattering. In the subluminal case, reading out Fig. 3.2(a), we write the scattered fields in terms of the incident fields

$$\psi_j^+ = \tau_{ji}\psi_i^+ + \bar{\gamma}_{jij}\psi_j^-, \tag{3.71a}$$

$$\psi_i^- = \gamma_{iji}\psi_i^+ + \bar{\tau}_{ij}\psi_j^-, \tag{3.71b}$$

and rearrange these equations to cast them into the form of (3.70), i.e.,

$$[T_{ji}^{\mathrm{Sb}}] = \frac{1}{\bar{\tau}_{ij}} \begin{bmatrix} \tau_{ji}\bar{\tau}_{ij} - \bar{\gamma}_{jij}\gamma_{iji} & \bar{\gamma}_{jij} \\ -\gamma_{iji} & 1 \end{bmatrix}, \tag{3.72}$$

where the superscript Sb stands for subluminal. Substituting the interface scattering coefficients (E.2) into (3.72) yields

$$\left[T_{ji}^{\mathrm{Sb}}\right] = \frac{1}{2\eta_i} \begin{bmatrix} (\eta_i + \eta_j)\dfrac{1 - v_{\mathrm{m}}/v_i}{1 - v_{\mathrm{m}}/v_j} & (\eta_i - \eta_j)\dfrac{1 + v_{\mathrm{m}}/v_i}{1 - v_{\mathrm{m}}/v_j} \\ (\eta_i - \eta_j)\dfrac{1 - v_{\mathrm{m}}/v_i}{1 + v_{\mathrm{m}}/v_j} & (\eta_i + \eta_j)\dfrac{1 + v_{\mathrm{m}}/v_i}{1 + v_{\mathrm{m}}/v_j} \end{bmatrix}. \tag{3.73}$$

In the superluminal case, reading out Fig. 3.2(b), we write the scattered fields in terms of the incident fields as

$$\psi_j^+ = \xi_{ji}\psi_i^+ + \bar{\zeta}_{ji}\psi_i^-, \tag{3.74a}$$

$$\psi_j^- = \zeta_{ji}\psi_i^+ + \bar{\xi}_{ji}\psi_i^-. \tag{3.74b}$$

These equations can then be cast into the matrix form of (3.70)

$$[T_{ji}^{\mathrm{Sp}}] = \begin{bmatrix} \xi_{ji} & \bar{\zeta}_{ji} \\ \zeta_{ji} & \bar{\xi}_{ji} \end{bmatrix}, \tag{3.75}$$

with the superscript Sp standing for superluminal. We note that (3.75) is much simpler than (3.72), since in the superluminal case both incident waves are in the first medium and both scattered waves are in the later medium. In other words, the scattering matrix is equal to the interface matrix for the superluminal case. Although (3.75) and (3.72) have a very different appearance, inserting (E.3) into (3.75) reveals that they are in fact exactly identical, i.e. $[T_{ji}^{\mathrm{Sb}}] = [T_{ji}^{\mathrm{Sp}}]$, consitently with Biancalana's result [106].

We next derive the propagation matrix, which relates the fields at the first and second interface delimiting a given layer. For instance, the propagation matrix of layer j is given by

$$\begin{bmatrix} \psi_j^+ \\ \psi_j^- \end{bmatrix}_{I_{j,k}} = [P_j] \begin{bmatrix} \psi_j^+ \\ \psi_j^- \end{bmatrix}_{I_{i,j}} . \tag{3.76}$$

Since there is no scattering and only a phase shift between the interfaces, the matrix simply reads

$$[P_j] = \begin{bmatrix} \mathrm{e}^{i\varphi_j^+} & 0 \\ 0 & \mathrm{e}^{-i\varphi_j^-} \end{bmatrix} = \mathrm{e}^{i\Delta\varphi_j} \begin{bmatrix} \mathrm{e}^{i\bar{\varphi}_j} & 0 \\ 0 & \mathrm{e}^{-i\bar{\varphi}_j} \end{bmatrix}, \tag{3.77}$$

with the phase terms defined in Sec. 3.4. Inserting the interface matrix (3.73) and the propagation matrix (3.77) into (3.68) yields the unit-cell transfer matrix

$$[M_{\mathrm{B}}] = \mathrm{e}^{i\Delta\varphi} \begin{bmatrix} a & ib \\ ic & a^* \end{bmatrix} = \mathrm{e}^{i\Delta\varphi}[M_{\mathrm{B0}}], \tag{3.78}$$

where

$$a = \mathrm{e}^{i\bar{\varphi}_k} \left(\cos\bar{\varphi}_j + \frac{i}{2} \left(\frac{\eta_j}{\eta_k} + \frac{\eta_k}{\eta_j} \right) \sin\bar{\varphi}_j \right), \tag{3.79a}$$

$$b = -\mathrm{e}^{-i\bar{\varphi}_k} \frac{1}{2} \left(\frac{\eta_j}{\eta_k} - \frac{\eta_k}{\eta_j} \right) \frac{1 + v_{\mathrm{m}}/v_j}{1 - v_{\mathrm{m}}/v_j} \sin\bar{\varphi}_j, \tag{3.79b}$$

$$c = \mathrm{e}^{i\bar{\varphi}_k} \frac{1}{2} \left(\frac{\eta_j}{\eta_k} - \frac{\eta_k}{\eta_j} \right) \frac{1 - v_{\mathrm{m}}/v_j}{1 + v_{\mathrm{m}}/v_k} \sin\bar{\varphi}_j. \tag{3.79c}$$

Equations (3.79) are valid for both the subluminal regime and the superluminal regime, with the phase expressions $\bar{\varphi}_{j,k}$ and $\Delta\varphi_{j,k}$ provided in Tab. 3.3. Matrix $[M_{B0}]$ is unimodular, and so the determinant of M_{B} in (3.78) is $\det[M_{\mathrm{B}}] = \mathrm{e}^{i\Delta\varphi}$. Note that this matrix satisfies the conditions $b\mathrm{e}^{i\Delta\phi} = -b^*$ and $c\mathrm{e}^{i\Delta\phi} = -c^*$ [123], which stems from space-time reversal symmetry, as shown in App. A. Identical results were found in Biancalana's paper [106] using an alternative approach based on a symmetric form of Maxwell equations.

Dispersion Relation Derivation

The exact dispersion diagram may now be computed using the unit-cell transfer matrix (3.78), which we have just derived. From Bloch-Floquet theory, the fields before and after the unit-cell of a crystal are related through $\psi_k^{\pm} = \mathrm{e}^{i\Phi_\mathrm{B}}\psi_i^{\pm}$, where Φ_B is the Bloch-Floquet phase. This leads to the eignenvalue problem

$$\begin{bmatrix}\psi_\mathrm{k}^+ \\ \psi_\mathrm{k}^-\end{bmatrix}_{I_{k,l}} = [M_\mathrm{B}]\begin{bmatrix}\psi_\mathrm{i}^+ \\ \psi_\mathrm{i}^-\end{bmatrix}_{I_{i,j}} = \mathrm{e}^{i\Phi_\mathrm{B}}\begin{bmatrix}\psi_\mathrm{i}^+ \\ \psi_\mathrm{i}^-\end{bmatrix}_{I_{i,j}}. \tag{3.80}$$

The eigensolution to this problem is found by substituting (3.78) into (3.80), grouping the difference phase $\mathrm{e}^{i\Delta\varphi}$ with the Bloch-Floquet phase $\mathrm{e}^{i\Phi_\mathrm{B}}$, so that $([M_{\mathrm{B}0}]-\mathrm{e}^{i(\Phi_\mathrm{B}-\Delta\varphi)}[I])[\psi_i] = 0$, and setting the determinant to zero, i.e.,

$$\begin{vmatrix} a-\mathrm{e}^{i(\Phi_\mathrm{B}-\Delta\varphi)} & b \\ c & a^*-\mathrm{e}^{i(\Phi_\mathrm{B}-\Delta\varphi)}\end{vmatrix} = 0. \tag{3.81}$$

This corresponds to a quadratic equation whose solutions are

$$\mathrm{e}^{i(\Phi_\mathrm{B}-\Delta\varphi)} = \frac{a+a^*}{2} \pm \sqrt{\left(\frac{a+a^*}{2}\right)^2 - 1}, \tag{3.82}$$

where the identity $aa^* - bc = 1$ associated with the unimodularity of $[M_{B0}]$ has been applied. Equation (3.82) may be rewritten in a more standard, trigonometric form by applying the Euler identity $\mathrm{e}^{i(\Phi_\mathrm{B}+\Delta\varphi)} = \cos(\Phi_\mathrm{B}+\Delta\varphi) + i\sin(\Phi_\mathrm{B}+\Delta\varphi)$ to the left hand side of (3.82) and writing $i\sin(\Phi_\mathrm{B}+\Delta\varphi) = \pm\sqrt{\cos^2(\Phi_\mathrm{B}+\Delta\varphi)-1}$. Comparing the result with the right hand side of (3.82) implies

$$\begin{aligned}\cos(\Phi_\mathrm{B}-\Delta\varphi) &= \frac{a+a^*}{2} \\ &= \cos\bar{\varphi}_j\cos\bar{\varphi}_k - \frac{1}{2}\left(\frac{\eta_j}{\eta_k}+\frac{\eta_k}{\eta_j}\right)\sin\bar{\varphi}_j\sin\bar{\varphi}_k,\end{aligned} \tag{3.83}$$

where (3.79) has been used in the second equality.

Equation (3.83) is the dispersion relation, whose graphical representation corresponds to the dispersion diagram, which we will construct next. We may already note that the phase Φ_B in (3.83) may be either real or complex, since the right hand side may be less than 1, and the inverse cosine of a quantity less than one is complex. A real Φ_B phase will be associated with pure propagation, while an imaginary Φ_B phase will be associated with either attenuation or amplification, corresponding to bandgaps in the dispersion diagram.

Construction of Dispersion Diagram

The dispersion relation (3.83) essentially relates the Bloch-Floquet phase (Φ_B) and the phases in the layers of the crystal ($\bar{\varphi}$ and $\Delta\varphi$). To plot the dispersion diagram, we must transform this relation into one of that relates the frequencies and wavenumbers (ω and k). This may be conveniently done using a set of parametric equations.

We start with the subluminal case. First, we write the Bloch-Floquet phase in terms of the frequency and wavenumber, i.e.,

$$\Phi_\mathrm{B} = \Phi'_\mathrm{B} = k'\ell'_\mathrm{B} = \gamma^2 \left(k - \frac{v_\mathrm{m}}{c^2}\omega \right) \ell_\mathrm{B}, \tag{3.84}$$

where the last equation used the Lorentz wavenumber transformation (3.10) and length contraction (3.37). The frequency and wavenumber in (3.84) are related to the conserved frequency parameter ω_e through

$$\omega_\mathrm{e} = \omega - v_\mathrm{m} k, \tag{3.85}$$

from the fact that $\omega'_\mathrm{e} = \omega'$, similarly to (3.26). Combining (3.84) and (3.85), and factoring out ω and k finally yields the parametric equations

$$\omega\left(\omega_\mathrm{e}\right) = \frac{v_\mathrm{m}\Phi_\mathrm{B}\left(\omega_\mathrm{e}\right)}{\ell_\mathrm{B}} + \gamma^2\omega_\mathrm{e}, \tag{3.86a}$$

$$k\left(\omega_\mathrm{e}\right) = \frac{\Phi_\mathrm{B}\left(\omega_\mathrm{e}\right)}{\ell_\mathrm{B}} + \gamma^2\frac{v_\mathrm{m}^2}{c^2}\omega_\mathrm{e}. \tag{3.86b}$$

To plot the dispersion relations, we first calculate the Bloch-Floquet phase $\Phi_\mathrm{B}(\omega_\mathrm{e})$ using (3.83), with $\bar{\varphi}_{i,j}(\omega_\mathrm{e})$ and $\Delta\varphi_{i,j}(\omega_\mathrm{e})$ given in Tab. 3.3. We then compute $\omega(\omega_\mathrm{e})$ and $k(\omega_\mathrm{e})$ in (3.86) independently, for a range of frequencies ω_e, and plot them to obtain the dispersion diagram of Fig. 3.12(a).

In the superluminal case, the Bloch-Floquet phase is

$$\Phi_\mathrm{B} = \Phi'_\mathrm{B} = \omega' d'_\mathrm{B} = \gamma^2 \left(\omega - \frac{c^2}{v_\mathrm{m}}k \right) d_\mathrm{B}, \tag{3.87}$$

where the second equality was again found from the Lorentz frequency transformation (3.10) and the time contraction (3.40). The frequency and wavenumber in (3.87) are related to the conserved spatial frequency k_e through

$$k_\mathrm{e} = k - \omega/v_\mathrm{m}, \tag{3.88}$$

from the fact that $k_\mathrm{e}' = k'$ as in (3.28). Combining (3.87) with (3.88) leads to the parametric equations

$$\omega\left(k_\mathrm{e}\right) = \frac{\Phi_\mathrm{B}\left(k_\mathrm{e}\right)}{d_\mathrm{B}} + \gamma^2 \frac{c^2}{v_\mathrm{m}} k_\mathrm{e}, \tag{3.89a}$$

and

$$k\left(k_\mathrm{e}\right) = \frac{\Phi_\mathrm{B}\left(k_\mathrm{e}\right)}{v_\mathrm{m} d_\mathrm{B}} + \gamma^2 k_\mathrm{e}. \tag{3.89b}$$

The dispersion diagram corresponding to the parametric equations (3.89) is plotted Fig. 3.12(b) following the same procedure as for the subluminal case, i.e., calculating $\Phi_\mathrm{B}(k_\mathrm{e})$ from (3.83), with $\bar{\varphi}(k_\mathrm{e})$ and $\Delta\varphi(k_\mathrm{e})$ given in Tab. 3.3, and then computing the parametric equations (3.89) for $\omega(k_\mathrm{e})$ and $k(k_\mathrm{e})$.

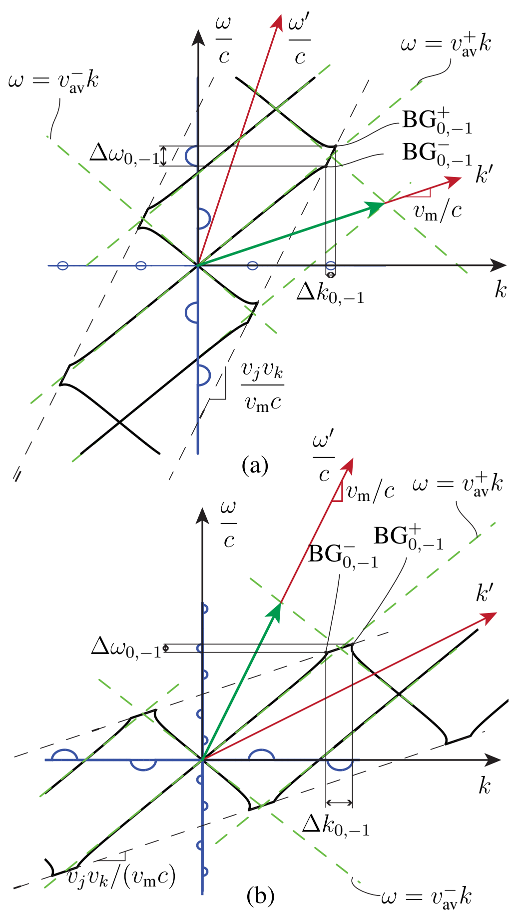

Figure 3.12 Dispersion diagram of bilayer crystals with $n_2/n_1 = 1.5$ and equal phases ($\bar{\varphi}_j = \bar{\varphi}_k$). The solid curves corresponds to the exact solution [Eqs. (3.86) and (3.89)], with the black and blue parts respectively corresponding to the real and imaginary parts, while the dashed curves to the linear approximation [Eq. (3.63)]. (a) Subluminal case, with $v = (1/3)c$. (b) Superluminal case, with $v = 3c$.

Figure 3.12 plots not only the exact dispersion diagram, but also the linear approximation derived in Sec. 3.5. It may be seen that latter coincides with the former as expected.

Equal-Phase Crystals

The formulas of the previous sections are completely general and readily amenable to computation. For presentation simplicity, the rest of the paper studies the particular design of an equal-phase crystal, which is a generalization of the conventional quarter-stack structure. In this section, we find the closed-form expressions of the average and difference phase of equal-phase crystals.

We define a bilayer equal-phase crystal as a crystal whose two layers constituting the unit cell induce the same round-trip phase shift, i.e.

$$\bar{\varphi} = \bar{\varphi}_j = \bar{\varphi}_k. \tag{3.90}$$

For stationary crystals, this corresponds to the condition $n_i\ell_i = n_j\ell_j$, which is called the quarter-wave stack condition when $n_i\ell_i = n_j\ell_j = \lambda_0/4$ [117].

In the subluminal case, the expression of the average phase is written in terms of the lengths, the modulation velocity and the wave velocities by inserting (3.38b) into (3.90), yielding

$$\bar{\varphi} = \omega_\mathrm{e}\frac{\ell_j v_j}{v_j^2 - v_\mathrm{m}^2} = \omega_\mathrm{e}\frac{\ell_k v_k}{v_k^2 - v_\mathrm{m}^2} = \omega_\mathrm{e} d_\mathrm{e}/2, \tag{3.91}$$

where the quantity d_e corresponds to the time a wave takes to accomplish a round trip in a layer, as can be found geometrically from the plot of d_e in Fig. 3.9(a). Therefore if two layers have the same round-trip duration d_e, we will call them equal-phase. For later use, we express this round-trip duration in terms of the physical length of the unit cell, ℓ_B, as

$$d_\mathrm{e} = \frac{2v_j v_k}{(v_j + v_k)\left(v_j v_k - v_\mathrm{m}^2\right)}\ell_\mathrm{B}, \tag{3.92}$$

which may also be found geometrically from Fig. 3.9(a).

The total phase difference $\Delta\varphi$ between forward and backward waves in the entire unit-cell is

$$\begin{aligned}\Delta\varphi &= \Delta\varphi_j + \Delta\varphi_k \\ &= v_\mathrm{m}\gamma^2\frac{(v_j + v_k)(1 - v_j v_k/c^2)}{v_j v_k}\omega_\mathrm{e} d_\mathrm{e} \\ &= 2v_\mathrm{m}\gamma^2\frac{1 - v_j v_k/c^2}{v_j v_k - v_\mathrm{m}^2}\omega_\mathrm{e}\ell_\mathrm{B}.\end{aligned} \tag{3.93}$$

where (3.38c) and (3.92) have been used in the second and third equalities.

In the superluminal case, the equal-phase condition is written in terms of the durations of the layers, the modulation velocity and the wave velocities by inserting (3.41b) into (3.90), yielding

$$\bar{\varphi} = k_\mathrm{e}\frac{d_j v_\mathrm{m}^2 v_j}{v_\mathrm{m}^2 - v_j^2} = k_\mathrm{e}\frac{d_k v_\mathrm{m}^2 v_k}{v_\mathrm{m}^2 - v_k^2} = k_\mathrm{e}\ell_\mathrm{e}/2, \tag{3.94}$$

where ℓ_e corresponds to the total travel length of the forward and backward waves in a slab, as can be found from Fig. 3.9(b), and is related to the duration d_B through

$$\ell_\mathrm{e} = \frac{2v_\mathrm{m}^2 v_j v_k}{(v_j + v_k)\left(v_\mathrm{m}^2 - v_j v_k\right)} d_\mathrm{B}. \tag{3.95}$$

The total phase difference, $\Delta\varphi$, is

$$\begin{aligned}\Delta\varphi &= \Delta\varphi_j + \Delta\varphi_k \\ &= \gamma^2 \frac{c^2}{v_\mathrm{m}^2}\frac{(v_j + v_k)(1 - v_j v_k/c^2)}{v_j v_k} k_\mathrm{e}\ell_\mathrm{e} \\ &= v_\mathrm{m} c^2 \gamma^2 \frac{1 - v_j v_k/c^2}{v_j v_k - v_\mathrm{m}^2} k_\mathrm{e} d_\mathrm{B}\end{aligned} \tag{3.96}$$

where (3.41c) and (3.95) have been used in the second and third equalities.

Description of the Dispersion Diagram

Brillouin Zone

The dispersion diagrams corresponding to the exact solutions (3.86) and (3.89) are plotted only for first Brillouin zones in Fig. 3.12, since the rest of the diagrams follows by periodicity. To find the limits of the Brillouin zones, we study equation (3.83), and see that this function is periodic in $\Phi_\mathrm{B} - \Delta\varphi = 2\pi n$. We therefore define the Brillouin zones as delimited by

$$\Phi_\mathrm{B} - \Delta\varphi = \pm\pi. \tag{3.97}$$

In the subluminal case, this can be expressed in terms of the frequency and wavenumber by substituting (3.84) and (3.93) with (3.85) into (3.97), yielding

$$k = \frac{v_\mathrm{m}}{v_j v_k}\omega \pm \frac{\pi(v_j v_k - v_\mathrm{m}^2)}{v_j v_k \ell_\mathrm{B}}. \tag{3.98}$$

This is the expression for the two oblique lines delimiting the Brillouin zone. Their slope is $v_j v_k/v_\mathrm{m}$, and the k-intercepts are $\pm\pi(v_j v_k - v_\mathrm{m}^2)/(v_j v_k \ell_\mathrm{B})$, reducing, as expected, to $\pm\pi/\ell_\mathrm{B}$ in the stationary case. Note that the limits of the Brillouin zone are not parallel to the ω' axis, as they would be for the case of a moving medium. In the case of a moving isotropic medium, the crystal would appear stationary in the moving frame and so the Brillouin zone would be parallel to the ω' axis.

In the superluminal case, substituting (3.87) and (3.96) with (3.88) into (3.97) yields

$$\omega = \frac{v_j v_k}{v_\mathrm{m}} k \pm \frac{\pi(v_\mathrm{m}^2 - v_j v_k)}{v_\mathrm{m}^2 d_\mathrm{B}}. \tag{3.99}$$

with the slope being again $v_j v_k/v_\mathrm{m}$.

Complex Nature of the Bandgaps

The bandgaps correspond to the imaginary part of the solution in Fig. 3.12, with the imaginary frequencies alternating along the k axis and the imaginary wavenumbers alternating along the ω axis. We see that the frequencies and the wavenumbers are simultaneously complex, for both the subluminal and superluminal regimes. This is a feature that seems to have been previously overlooked in the literature, although it is a straightforward consequence of the Lorentz transformations.

In the subluminal case, the moving-frame solution has the complex wavenumbers $k' = k'_\mathrm{r} + ik'_\mathrm{i}$, with k'_r, k'_i the real and imaginary parts, and purely real frequencies, so that $\omega'_\mathrm{i} = 0$. Applying the frequency Lorentz transformation (3.10) to the imaginary frequency yields $\omega_\mathrm{i} - v_\mathrm{m} k_\mathrm{i} = 0$, or $\omega_\mathrm{i} = v_\mathrm{m} k_\mathrm{i}$, which shows that the complexity of k_i indeed implies the complexity of ω_i, with ω_i non negligible for relativistic velocities.

In the superluminal case, the moving-frame solution has the complex wavenumbers $\omega' = \omega'_\mathrm{r} + i\omega'_\mathrm{i}$, with ω'_r, ω'_i the real and imaginary parts, and purely real wavenumbers, so that $k'_\mathrm{i} = 0$. Applying the wavenumber Lorentz transformation (3.10) to the imaginary wavenumber, with $v_\mathrm{f} = c^2/v_\mathrm{m}$, yields $k_i - (1/v_\mathrm{m})\omega_i = 0$, or $k_i = \omega_i/v_\mathrm{m}$, so that the complexity of ω_i implies the complexity of k_i, with k_i decreasing as the modulation velocity increases.

Bandgap Edges

We now calculate the edges of the bandgaps, indicated as $\mathrm{BG}^{\pm}_{p,q}$ in Fig. 3.12, where the subscripts indicate the two modes involved, and the superscript $\pm$ refers to the top and bottom edges. Theses edges are found by analyzing the exact solution (3.83), which reduces to

$$\cos(\Phi_{\mathrm{B}} - \Delta\varphi) = \cos^2\bar{\varphi} - \frac{1}{2}\left(\frac{\eta_1}{\eta_2} + \frac{\eta_2}{\eta_1}\right)\sin^2\bar{\varphi} \tag{3.100}$$

in the equal-phase case, $\bar{\varphi}_1 = \bar{\varphi}_2 = \bar{\varphi}$ (Sec. 3.5).

The bandgaps correspond to complex Bloch-Floquet phases, and therefore to the right-hand side of (3.100) being less than -1. Thus, the bandgap edges occur at the limit

$$\cos^2\bar{\varphi} - \frac{1}{2}\left(\frac{\eta_1}{\eta_2} + \frac{\eta_2}{\eta_1}\right)\sin^2\bar{\varphi} = -1. \tag{3.101}$$

Applying the trigonometric relation $\sin^2(\bar{\varphi}) = 1 - \cos^2(\bar{\varphi})$ and grouping the cosine terms, we find that the bandgap edge condition reduces to

$$\bar{\varphi} = \arccos\left(\pm\frac{\eta_2 - \eta_1}{\eta_1 + \eta_2}\right) = \arccos(\pm\upsilon) \overset{\upsilon \ll 1}{\approx} \frac{\pi}{2} \mp \upsilon. \tag{3.102}$$

This condition delimits two curves on which the bandgap edges lie. In addition, the bandgap edges lie on the Brillouin zone limits, as can be seen in Fig. 3.12. This is found by noting that the inverse cosine of a quantity less than -1 has the form $\pi + ix$, and at the limit is $\pm\pi$. Setting the inverse cosine of the right-hand side of (3.100) equal to $\pm\pi$ retrieves (3.97).

In the subluminal case, the condition for the bandgap edge may be written in terms of frequency and wavenumber by inserting (3.91) with (3.85) into (3.102) as

$$\omega = v_{\mathrm{m}}k + \frac{1}{d_{\mathrm{e}}}\arccos(\pm\upsilon), \tag{3.103}$$

which represent the equations of the parallel straight curves, with slope v_{m} and ω-intercept $1/d_{\mathrm{e}}\arccos(\pm\upsilon)$, that delimit the bandgap. The Brillouin zone limits are written in terms of frequencies and wavenumbers in (3.98). Solving this system of equations provides the bandgap edge positions $\mathrm{BG}_{0,-1}$ as

$$\omega_{0,-1}^{\pm} = \frac{1}{\ell_{\mathrm{B}}}\left(v_{\mathrm{m}}\pi + (v_j + v_k)\arccos\left(\pm\upsilon\right)\right), \tag{3.104a}$$

$$k_{0,-1}^{\pm} = \frac{1}{\ell_{\mathrm{B}}}\left(\pi + \frac{v_{\mathrm{m}}(v_j + v_k)}{v_j v_k}\arccos\left(\pm\upsilon\right)\right). \tag{3.104b}$$

From these results, we may express the bandgap width $\Delta\omega_{0,-1} = \omega^+_{0,-1} - \omega^-_{0,-1}$ as

$$\begin{aligned}\Delta\omega_{0,-1} &= \frac{v_j + v_k}{\ell_\mathrm{B}} \left(\arccos \upsilon - \arccos(-\upsilon)\right) \\ &\overset{\upsilon\ll 1}{\approx} 2\frac{vj + v_k}{\ell_\mathrm{B}}|\upsilon|,\end{aligned} \tag{3.105}$$

and the corresponding wavenumber width $\Delta k_{0,-1} = k^+_{0,-1} - k^-_{0,-1}$, simply found as $\Delta k_{0,-1} = \Delta\omega_{0,-1} v_\mathrm{m}/(v_j v_k)$ from the geometrical construction in Fig. 3.12(a).

Note that the bandgap widths are the same for all the bandgaps in the case of equal-phase crystals, so that the edges of all the bandgaps may be found from the bandgap width expressions and the center positions provided in (3.65).

In the superluminal case, the bandgap edges lie at the intersection of the straight line given by (3.102) and the Brillouin zone limits, the former of which is rewritten in terms of frequency and wavenumber by inserting (3.94) with (3.88) into (3.102) as

$$k = \frac{\omega}{v_\mathrm{m}} + \frac{1}{\ell_\mathrm{e}} \arccos(\pm\upsilon), \tag{3.106}$$

and the latter of which corresponds to (3.99). Solving for this system of equations, we find the positions of the limits of the gap $\mathrm{BG}_{0,-1}$, denoted by $\mathrm{BG}^\pm_{0,-1}$ in Fig. 3.12(b), as

$$k^\pm_{0,-1} = \frac{1}{d_\mathrm{B}} \left(\frac{\pi}{v_\mathrm{m}} + \frac{v_j + v_k}{v_j v_k} \arccos\left(\pm\upsilon\right)\right), \tag{3.107a}$$

$$\omega^\pm_{0,-1} = \frac{1}{d_\mathrm{B}} \left(\pi + \frac{v_j + v_k}{v_\mathrm{m}} \arccos\left(\pm\upsilon\right)\right). \tag{3.107b}$$

From these results, we may express the bandgap width $\Delta k_{0,-1} = k^+_{0,-1} - k^-_{0,-1}$ as

$$\begin{aligned}\Delta k_{0,-1} &= \frac{v_j + v_k}{v_j v_k d_\mathrm{B}} \left(\arccos \upsilon - \arccos(-\upsilon)\right) \\ &\overset{\upsilon\ll 1}{\approx} 2\frac{v_j + v_k}{v_j v_k d_\mathrm{B}}|\upsilon|,\end{aligned} \tag{3.108}$$

and the frequency width $\Delta\omega_{0,-1} = \omega^+_{0,-1} - \omega^-_{0,-1}$ is then simply found as $\Delta\omega_{0,-1} = \Delta k_{0,-1} v_j v_k / v_\mathrm{m}$, from the geometrical construction in Fig. 3.12(b).

3.6 Truncated Crystal

Types of Truncation

As for conventional crystals, practical spacetime crystals are necessarily finite, and may be truncated along different directions, including now also the time direction.

Figure 3.13 describes examples of spacetime crystal truncation. In the top row (Figs. 3.13(a)-(c)), the crystals are truncated on the left and on the right by interfaces sharing the same velocity. In the bottom row (Figs. 3.13(d)-(f)) the crystals are truncated on the left and on the right by interfaces of different velocities. The truncations of Fig. 3.13 represent only a few of an infinite number of possibilities, including for instance multiple truncations separating the crystal in different parts, truncations delimiting holes, or spacetime defects, in the crystal, or periodic truncation leading to a multiscale spacetime crystal.

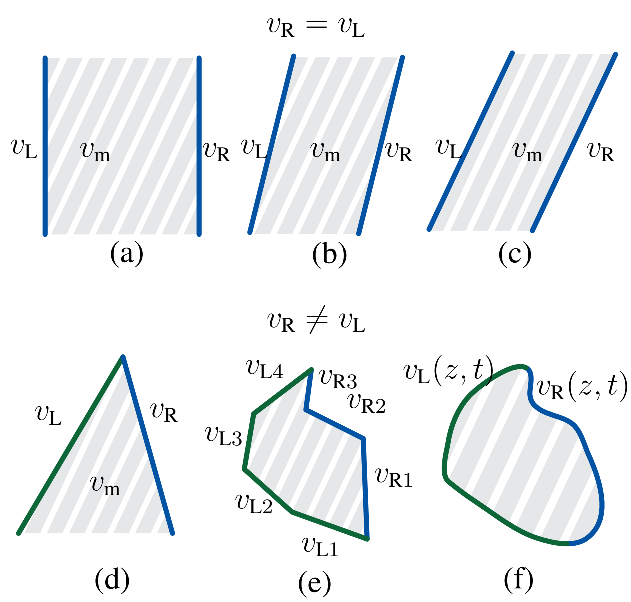

Figure 3.13 Examples of spacetime crystal truncation by a pair of spactime interfaces of velocities v_L and v_R for the left and right interfaces, respectively. Top row: the two interfaces have the same velocity, $v_L = v_R$. Bottom row: the two interfaces have different velocities, $v_L \neq v_R$. (a) Purely spatial truncation, $v_L = v_R = 0$. (b) Truncation with velocity different from the modulation velocity, $v_L = v_R \neq v_m$. (c) Co-moving truncation, $v_L = v_R = v_m$. (d) Antiparallel truncation, $v_L \neq v_R \neq v_m$. (e) Spacetime cavity with piecewise constant velocities. (f) Spacetime cavity with continuously varying velocity.

Figure 3.14 illustrates the scattering phenomenology for truncated spacetime crystals, with Fig. 3.14(a) corresponding to the co-moving structure of Fig. 3.13(c) and Fig. 3.14(b) corresponding to the purely spatially truncated crystal of Fig. 3.13(a). The top panels show the frequency transitions in the dispersion diagrams, while the bottom panels show the different scattered waves in the spacetime diagrams.

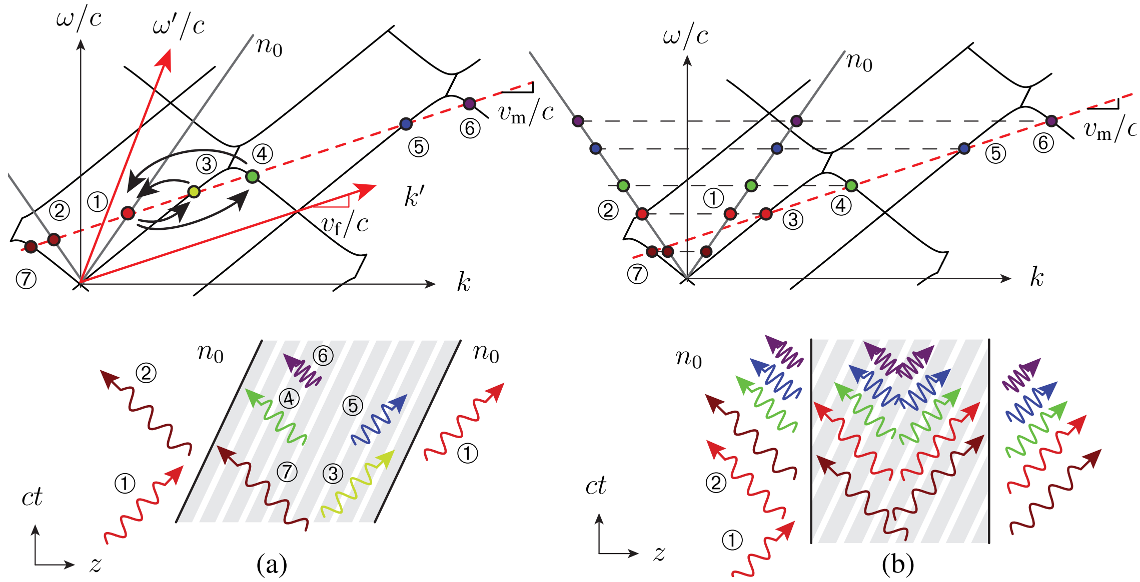

Figure 3.14 Scattering from two canonical truncated spacetime crystals. In both cases, the crystal is subluminal, and the medium surrounding it is a simple nondispersive dielectric medium of refractive index n_0. Top row: dispersion diagrams with transition frequencies. Bottom row: spacetime diagrams with scattered waves, with labels corresponding the solutions of the top panels. Note that the drawn scattered waves correspond to the waves seen in the laboratory frame, and would completely different in the moving frame. (a) Co-moving truncation. A moving-frame observer would see a stationary crystal bounded by stationary interfaces, and hence measure a unique frequency everywhere, inside and outside the crystal. The arrows indicate the up and down frequency and wavenumber transitions at the two interfaces. (b) Purely spatial truncation. A moving-frame observer would see a stationary crystal bounded by moving interfaces, and hence measure an infinity of frequencies.

Let us start with the co-moving truncated crystal [Fig. 3.14(a)]. The transition frequencies are obtained trough the following construction. First, we plot the dispersion diagrams of the spacetime crystal (Sec. 3.5) and of the surrounding medium, which is here a simple pair of straight lines in the present nondispersive case. Second, we place the point corresponding to the incident wave, labeled ①, on the dispersion diagram of the incident medium. Third, we trace an oblique line of slope v_m/c, corresponding to the moving-frame conserved frequency (see Sec. 3.3). The intersections of this line with the two dispersion diagrams provide the scattered frequencies. The corresponding scattered waves are represented in the spacetime diagram below the dispersion diagram.

We notice that, although infinitely many frequencies are excited inside the crystal (solutions labeled ③-⑦), the transmitted and reflected waves are monochromatic. Indeed, in the moving frame, the interfaces appear stationary, so that a single frequency exists throughout the structure. Therefore the reflected and transmitted solutions in the laboratory frame, found by applying the frequency Lorentz transformation (3.10), are also monochromatic. The incident and transmitted waves both transform in the same way, since they both propagate in the same direction, whereas the reflected wave, propagating in the opposite direction, acquires a different frequency. In the case of Fig. 3.14(a) it is downshifted, as expected from the Doppler effect for a receding structure.

We now proceed to the analysis of the purely spatially truncated crystal [Fig. 3.14(b)]. The transition frequencies are obtained through the following construction. First, we plot again the dispersion diagrams of the spacetime crystal and the surrounding media, along with the incident wave, labeled ①. Second, we enforce frequency conservation at the first interface by tracing horizontal lines, which leads to the reflected wave labeled ② and the transmitted wave labeled ③. The frequency conservation in the moving frame involves then all the harmonic waves along the oblique line of slope v_m/c (labeled ④-⑦). Due to frequency conservation at the left and right interfaces, each of these harmonics produces a corresponding wave in the surrounding medium, so that the scattered waves contain multiple harmonics.

Scattering Coefficients

We now apply the transfer matrix technique to solve the problem of the co-moving truncation spacetime crystal [Fig. 3.14(a)]. The spatially truncated spacetime crystal may be studied using conventional phase matching and Bloch-Floquet techniques [39, 80].

The transmission and reflection coefficients of a spacetime crystal truncated by co-moving interfaces of N periods may be obtained by simply multiplying unit-cell transfer matrix (3.78) N times, and then extracting the coefficients. An alternative approach to the matrix multiplication is the application of the Chebyshev identity [117]

$$\begin{aligned}[M_\mathrm{B}]^N &= \mathrm{e}^{iN\Delta\phi}[M_\mathrm{B0}] \\ &= \mathrm{e}^{iN\Delta\phi}\begin{bmatrix} a\mathcal{U}_{N-1}(x)-\mathcal{U}_{N-2}(x) & ib\mathcal{U}_{N-1}(x) \\ ic\mathcal{U}_{N-1}(x) & a^*\mathcal{U}_{N-1}(x)-\mathcal{U}_{N-2}(x) \end{bmatrix},\end{aligned} \tag{3.109}$$

where $\mathcal{U}_N$ are the Chebyshev polynomials of the second kind, defined as

$$\mathcal{U}_N(x) = \frac{\sin[(N+1)\cos^{-1}x]}{\sqrt{1-x^2}} \tag{3.110}$$

with the argument

$$x = \frac{a + a^*}{2}, \tag{3.111}$$

where we recall that a, a^*, b, and c are the elements of the unit-cell matrix M_B, given in (3.79).

To extract the total transmission and reflection coefficients, the scattering matrix is written in terms of transfer-matrix parameters.

$$\begin{aligned}\begin{bmatrix}\psi_1^- \\ \psi_N^-\end{bmatrix} &= \begin{bmatrix}\Gamma_{11} & \bar{T}_{1N} \\ T_{N1} & \bar{\Gamma}_{NN}\end{bmatrix}\begin{bmatrix}\psi_1^+ \\ \psi_N^+\end{bmatrix} \\ &= \frac{1}{A^*}\begin{bmatrix}-A & 1 \\ AA^* - BC & A\end{bmatrix}\begin{bmatrix}\psi_1^+ \\ \psi_N^+\end{bmatrix},\end{aligned} \tag{3.112}$$

with A, A^*, B, C corresponding to the a, a^*, b, c elements of the $[M_\mathrm{B}]^N$ matrix.

The results are plotted in Fig. 3.15(a). We notice for waves in the gap, the reflected wave is partly absorbed by the structure, since the reflection coefficient is less than one, while there is no transmitted wave.

For the superluminal crystal, the scattering matrix is the same as the transfer matrix, since waves in the last medium are also the scattered waves. The coefficients are thus

$$Z_{N1} = A, \tag{3.113a}$$

$$\Xi_{N1} = C, \tag{3.113b}$$

and are plotted in Fig. 3.15. We see that in the gap, both the transmitted and the reflected wave are amplified. This is consistent with the analysis of the interference for a superluminal slab in Sec. 3.4: both scattered waves are in constructive interference in the bandgap.

We note that the bandgap centers in Fig. 3.15 do not correspond to the bandgap centers calculated in (3.65) and (3.67). This is due to the effect illustrated in Fig. 3.14(a): the frequencies horizontally aligned with the bandgaps will not see the bandgap. Instead, the frequencies aligned on an oblique line of slope v_m and passing through the bandgap will see the bandgap. The bandgap centers of Fig. 3.15 are provided in App. A.

3.7 Conclusion

We have performed a comprehensive analysis of uniform-velocity bilayer spacetime crystals. We started with the problem of spacetime interfaces, then addressed the problem of double-

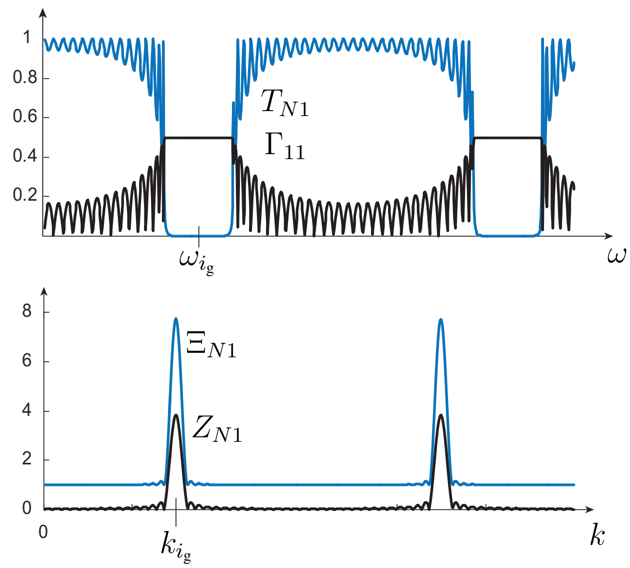

Figure 3.15 Transmission and reflection coefficients for an $N = 15$-layer crystal (corresponding to Fig. 3.13(c) and Fig. 3.14(a)) with $\bar{\phi}_{1,2} = \pi/2$. The gap centers ω_{i}, k_{i} are provided in App. A. (a) Subluminal case, with $v = 1/3c$ and $n_2/n_1 = 2$, with attenuation in the bandgaps. (b) Superluminal case, with $v = 3c$ and $n_2/n_1 = 1.2$ with amplification in the bandgaps.

interfaces, or spacetime slabs, next solved the problem of unbounded crystals, and finally studied the problem of truncated crystals.

Throughout the paper, we have made an extensive use of special relativity concepts, including the graphical tool of spacetime diagrams, which offered remarkable resolution simplicity, provided deep insight into the physics, and led us to uncover a number of new results. The new insights include a vivid Bragg-type description of the bandgap interference phenomenology, a quick linear approximation of dispersion diagrams, and the explanation of the effect of the truncation. The new results include the generalization of the Stokes principle to spacetime interfaces and the description of the simultaneous frequency and wavenumber complexity in the bandgaps.

This work may be extended to multi-layer-cell spacetime crystals, spacetime crystals made of dispersive media, and higher dimension crystals.

CHAPTER 4 ARTICLE 3: ORTHOGONAL ANALYSIS OF SPACE-TIME CRYSTALS

Zoé-Lise Deck-Léger, Amir Bahrami, Zhiyu Li and Christophe Caloz

Published in Optics Letters, Volume 48, Number 15, August 4, 2023

This paper presents a space-time-wise orthogonal analysis of space-time crystals. This analysis provides a solution consisting of a pair of explicit parametric equations that result from a separate application of the Bloch-Floquet theorem in the (orthogonal) directions of space and time. Compared to previous approaches, this solution offers the benefits of greater simplicity, clearer emphasis on space-time duality and deeper physical insight.

The emergence of photonic crystals [33, 76, 124] in the late 1980s as the optical counterparts of solid-state crystals [125] represented a major development in the field of electromagnetics. Recently, these crystals have gained even greater interest with the *addition of temporal modulation* to their spatial modulation within the framework of research on space-time metamaterials [96, 97, 126]. The resulting *space-time crystals* have already been demonstrated to support a diversity of novel effects, such as distributed parametric amplification [45, 51, 127], magnetless isolation [38, 39], space-time weighted averaging "dragging" [3, 126], beam deflection [40] and beam curving [54].

The addition of the time dimension dramatically complicates the computation of the dispersion diagram (or photonic bandgap structure) of photonic crystals. An early attempt to address the related challenge has been the plane-wave expansion method reported in [1, 37, 128]. However, this approach results in transcendental equations that are intractable and offer no direct insight into the physics of the crystals. A promising approach to resolve these issues might a priori seem to be the (spectral) frame-hopping technique [23], using respectively stationary and instantaneous moving frames for the space-like and time-like regimes [47, 97], but this technique would in fact involve cumbersome bianisotropic parameters [126, 129, 130] and complex space-time frequency coupling [96, 97]. A *partial* frame-hopping approach, applying periodicity in the direction of the moving frame but keeping quantities in the laboratory frame, was used in [3, 106] to remove the bianisotropic complication; however, this approach could not resolve the issue of coupling complexity.

We present here a *space-time-wise orthogonal approach* of space-time crystals, completely conducted in the laboratory frame, that avoids both bianisotropy and space-time frequency coupling. This approach offers thus maximum simplicity. Furthermore, it unveils fundamental symmetries between the spatial and temporal frequencies, hence highlighting strong duality between the two, and provides deeper insight into the physics of the crystal.

The spirit of the proposed solution may be best understood with the help of the crystals and related symmetries depicted in Fig. 4.1. Figure 4.1(a) shows a purely spatial crystal, with discrete translation symmetry, or periodicity (length ℓ), in space, leading to the production of wavevector harmonics, and with continuous translation symmetry (δt) in time, corresponding to frequency conservation [124]. Figure 4.1(b) shows a purely temporal crystal (e.g. [131]), with discrete translation symmetry, or periodicity (duration d), in time, leading to the production of frequency harmonics, and with continuous translation symmetry (δz) in space, corresponding to momentum conservation [97]. Figures 4.1(c) and (d) show a space-time crystal [3, 106], with modulation velocity v, under different symmetry perspectives: Figure 4.1(c) highlights the moving-frame perspective [3, 106], with continuous temporal and discrete spatial symmetries, which could be considered as the logical extension of the spatial crystal in a frame-hopping logic, whereas Fig. 4.1(d) highlights the space-time-wise orthogonal perspective that will be taken in this paper, with discrete translation symmetries, or periodicities, in both space and time. Note that Figs. 4.1(c) and (d) pertain to *subluminal* ($v < c/n_{i,j}$, where $c/n_{i,j}$ is the speed of light in a medium with refractive index $n_{i,j}$) space-time crystals; the corresponding figures for *superluminal* crystals ($v > c/n_{i,j}$) straightforwardly follow from subluminal-superluminal duality [47].

According to the elected strategy of orthogonal treatment of space and time, we shall proceed as follows in our analysis of the crystal: 1) establish the field waveforms with their motion-shifted frequencies and motion-deflected propagation angles in each layer of the crystal; 2) separately compute the corresponding spatial and temporal unit-cell [Fig. 4.1(d)] transmission matrices; 3) apply the Bloch-Floquet theorem to each of these matrices to obtain parametric relations for the Bloch-Floquet wavevector and frequency; 4) combine these relations to plot the dispersion diagram and isofrequency curves of the crystal.

Assuming propagation and scattering in the $x-z$ plane and s-polarization (the p-polarization case can be treated analogously), as illustrated in Fig. 4.2, the electric field waveform in the crystal may be written as the succession of individual layer waveforms, which read

$$E_n^{\pm} = A_n^{\pm} \mathrm{e}^{i(k_{x,n}^{\pm} x \pm k_{z,n}^{\pm} z - \omega_n^{\pm} t)}, \tag{4.1a}$$

with

$$k_{z,n}^{\pm} = \frac{n_n}{c}\omega_n^{\pm}\cos\theta_n^{\pm}, \quad k_{x,n}^{\pm} = \frac{n_n}{c}\omega_n^{\pm}\sin\theta_n^{\pm}, \tag{4.1b}$$

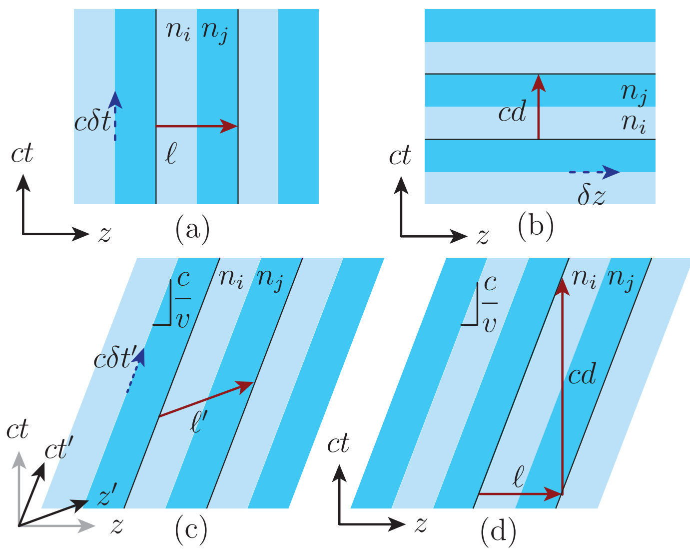

Figure 4.1 Basic crystals, composed of layers of media with alternating refractive indices (n_i and n_j), featuring discrete and continuous translation symmetries. (a) Spatial crystal. (b) Temporal crystal. (c) Space-time crystal with discrete spatial translation in the moving frame. (d) Space-time crystal with discrete spatial and temporal translations in the direct frame.

where we assume the medium to be isotropic, nondispersive and linear, with the subscripts n referring to the crystal layer and the superscript signs corresponding to propagation in the forward $(+z, +x)$ backward $(-z, +x)$ directions, respectively.

The motion-shifted frequencies $\omega_n^\pm$ and motion-deflected propagation angles $\theta_n^\pm$ in Eqs. (4.1b) may be found with the help of Fig. 4.2(a), which represents the corresponding wavevectors across two layers, labeled i and j. The phases $\phi_n^\pm = k_{x,n}^\pm x \pm k_{z,n}^\pm z - \omega_n^\pm t$ $(n = i, j)$ in (4.1a) must be conserved at the interface. Due to the absence of motion in the x direction, the component k_x of the wavevector is conserved at the crystal's interfaces and is hence unique across the crystal. In contrast, the frequencies, $\omega_n^\pm$, are not conserved, due to motion in the z direction. Enforcing the continuity of the phases at $z = z_n + vt$, with $k_{z,n}^\pm$ given in (4.1b) and $k_{x,n}^\pm = k_x$ yields [132]

$$\omega_n^\pm(\omega_i^+) = \frac{1 - \beta n_i \cos\theta_i^+}{1 \mp \beta n_n \cos\theta_n^\pm}\omega_i^+, \tag{4.2}$$

where $\beta = v/c$ is the normalized modulation velocity. The corresponding deflection angles are then found by substituting $\omega_{n,i}^\pm$ from the second expression in (4.1b) into (4.2), and solving for $\cos\theta_n^\pm$, which yields [132]

$$\cos\theta_n^\pm(\theta_i^+) = \pm\frac{C^2\beta \pm D_n}{(1 + C^2\beta^2)n_n}, \tag{4.3a}$$

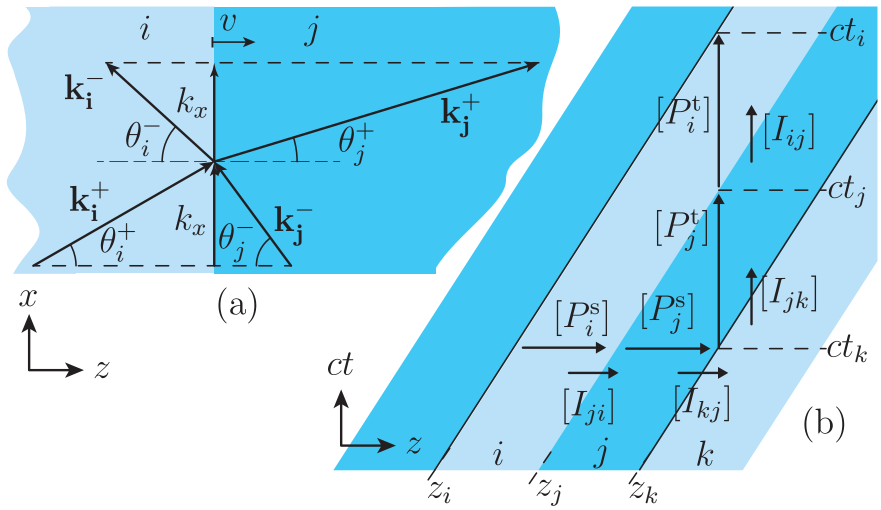

Figure 4.2 Crystal unit-cell features. (a) Frequency transitions and deflection angles at the interface between layers i and j. (b) Spatial and temporal unit-cell transfer matrices.

with

$$C = \frac{n_i \sin\theta_i^+}{1 - \beta n_i \cos\theta_i^+} \quad \text{and} \quad D_n = \sqrt{(1 + C^2\beta^2)n_n^2 - C^2}. \tag{4.3b}$$

Note that, at this point, all the quantities in Eqs. (4.1) are expressed in terms of the parameters ω_i^+ and θ_i^+ via Eqs. (4.2) and (4.3).

We can now compute the spatial and temporal transfer matrices of the unit cell. The spatial matrix, corresponding to the horizontal arrows in Fig. 4.2(b), $[M_{ki}^{\rm s}]$, relates the fields at the output of the unit cell, $E_k(z_k)$, to those at the input, $E_i(z_i)$, as

$$\begin{bmatrix} E_k^+ \\ E_k^- \end{bmatrix}_{z=z_k} = [M_{ki}^{\rm s}] \begin{bmatrix} E_i^+ \\ E_i^- \end{bmatrix}_{z=z_i} = [I_{kj}][P_j^{\rm s}][I_{ji}][P_i^{\rm s}] \begin{bmatrix} E_i^+ \\ E_i^- \end{bmatrix}_{z=z_i}, \tag{4.4}$$

where $[M_{ki}^{\rm s}]$ is composed of interface matrices $[I_{kj}]$ and $[I_{ji}]$ and propagation matrices $[P_j^{\rm s}]$ and $[P_i^{\rm s}]$, which are respectively defined by

$$\begin{bmatrix} E_{n+1}^+ \\ E_{n+1}^- \end{bmatrix}_{z_n} = [I_{n+1,n}] \begin{bmatrix} E_n^+ \\ E_n^- \end{bmatrix}_{z_n}, \quad \begin{bmatrix} E_n^+ \\ E_n^- \end{bmatrix}_{z_{n+1}} = [P_n^{\rm s}] \begin{bmatrix} E_n^+ \\ E_n^- \end{bmatrix}_{z_n}. \tag{4.5}$$

The interface matrices are found by applying the boundary conditions in terms of the electric fields at the moving interface and read (see App. B)

$$[I_{mn}] = \frac{1}{2f_m^+ f_m^-} \begin{bmatrix} f_n^+ g_m^- + f_m^- g_n^+ & -f_n^- g_m^- + f_m^- g_n^- \\ -f_n^+ g_m^+ + f_m^+ g_n^+ & f_n^- g_m^+ + f_m^+ g_n^- \end{bmatrix}, \tag{4.6a}$$

with

$$f_n^{\pm} = 1 \mp \beta n_n \cos\theta_n^{\pm}, \quad \text{and} \quad g_n^{\pm} = \frac{1}{\eta_n}\left(\cos\theta_n^{\pm} \mp \beta n_n\right), \tag{4.6b}$$

while the propagation matrices are obtained by inserting (4.1a) into the second equation of (4.5) with $z_{n+1} = z_n + \ell_n$, and read

$$[P_n^{\mathrm{s}}] = \begin{bmatrix} e^{ik_{z,n}^{+}\ell_n} & 0 \\ 0 & e^{-ik_{z,n}^{-}\ell_n} \end{bmatrix}. \tag{4.7}$$

Similarly, the temporal matrix, following the vertical arrows in Fig. 4.2(b), $[M_{ik}^{\mathrm{t}}]$, relates the fields at the output of the unit cell, $E_i(t_i)$, to those at the input, $E_k(t_k)$, as

$$\begin{bmatrix} E_i^{+} \\ E_i^{-} \end{bmatrix}_{t=t_i} = [M_{ik}^{\mathrm{t}}] \begin{bmatrix} E_k^{+} \\ E_k^{-} \end{bmatrix}_{t=t_k} = [P_i^{\mathrm{t}}][I_{ij}][P_j^{\mathrm{t}}][I_{jk}] \begin{bmatrix} E_k^{+} \\ E_k^{-} \end{bmatrix}_{t=t_k}, \tag{4.8}$$

where the interface matrices correspond to those for the spatial unit-cell [Eqs. 4.6] with inverted indices, while the temporal propagation matrices reads

$$[P_n^{\mathrm{t}}] = \begin{bmatrix} e^{i\omega_n^{+}d_n} & 0 \\ 0 & e^{i\omega_n^{-}d_n} \end{bmatrix}. \tag{4.9}$$

We can now proceed to the application of the Bloch-Floquet theorem in the spatial and temporal directions of the crystal to obtain the corresponding wavevectors and frequencies. In the spatial direction, the theorem states [133, 134]

$$E^{\pm}(z+\ell) = e^{\pm ik_z^{\pm}\ell} E^{\pm}(z), \tag{4.10}$$

where $k_z^{\pm}$ are the sought-after Bloch-Floquet wavevectors. Successively substituting $E^{\pm}(z) = E_i^{\pm}(z_i)$ and $E^{\pm}(z+\ell) = E_k^{\pm}(z_k)$ from Fig. 4.2(b) and the first relation of (4.4) into this equation yields

$$\begin{bmatrix} E_k^{+} \\ E_k^{-} \end{bmatrix}_{z_k} = \mathrm{e}^{\pm ik_z^{\pm}\ell} \begin{bmatrix} E_i^{+} \\ E_i^{-} \end{bmatrix}_{z_i} = [M_{ki}^{\mathrm{s}}] \begin{bmatrix} E_i^{+} \\ E_i^{-} \end{bmatrix}_{z_k}. \tag{4.11}$$

The second equality in (4.11) is an eigenvalue matrix equation, whose characteristic equation reads

$$\mathrm{e}^{\pm 2ik_z^{\pm}\ell} - \mathrm{tr}[M_{ki}^{\mathrm{s}}]\mathrm{e}^{\pm ik_z^{\pm}\ell} + \det[M_{ki}^{\mathrm{s}}] = 0, \tag{4.12a}$$

with, using (4.4) with Eqs. (4.6) and (4.7), the explicit terms

$$\det[M_{ki}^{\mathrm{s}}] = e^{i\Delta\phi^{\mathrm{s}}}, \tag{4.12b}$$

and

$$\mathrm{tr}[M_{ki}^{\mathrm{s}}] = 2e^{i\Delta\phi^{\mathrm{s}}/2}\left(C_i^{\mathrm{s}}C_j^{\mathrm{s}} - AS_i^{\mathrm{s}}S_j^{\mathrm{s}}\right) = 2e^{i\Delta\phi^{\mathrm{s}}/2}\mathrm{tr}[M_{ki,0}^{\mathrm{s}}], \tag{4.12c}$$

where $\Delta\phi^{\mathrm{s}} = \Delta\phi_i^{\mathrm{s}} + \Delta\phi_j^{\mathrm{s}}$, $C_n^{\mathrm{s}} = \cos(\Sigma\phi_n^{\mathrm{s}}/2)$, $S_n^{\mathrm{s}} = \sin(\Sigma\phi_n^{\mathrm{s}}/2)$,

$$\Delta\phi_n^{\mathrm{s}} = (k_{z,n}^{+} - k_{z,n}^{-})\ell_n, \quad \Sigma\phi_n^{\mathrm{s}} = (k_{z,n}^{+} + k_{z,n}^{-})\ell_n, \tag{4.12d}$$

and

$$A(\theta_i^{+}) = \frac{{f_j^{+}}^2{g_i^{+}}^2 + {f_i^{+}}^2{g_j^{+}}^2}{2f_i^{+}f_j^{+}g_i^{+}g_j^{+}}. \tag{4.12e}$$

Multiplying now (4.12a) with (4.12b) by $\mathrm{e}^{-i\Delta\phi^{\mathrm{s}}}$ leads to

$$\mathrm{e}^{2i(\pm k_z^{\pm}\ell - \Delta\phi^{\mathrm{s}}/2)} - \mathrm{tr}[M_{ki,0}^{\mathrm{s}}]\mathrm{e}^{i(\pm k_z^{\pm}\ell - \Delta\phi^{\mathrm{s}}/2)} + 1 = 0, \tag{4.13}$$

which is a quadratic equation with solutions

$$\mathrm{e}^{\pm i(k_z^{\pm}\ell \mp \Delta\phi^{\mathrm{s}}/2)} = \frac{\mathrm{tr}[M_{ki,0}^{\mathrm{s}}]}{2} \pm i\sqrt{1 - \left(\frac{\mathrm{tr}[M_{ki,0}^{\mathrm{s}}]}{2}\right)^2}. \tag{4.14}$$

According to Euler's formula, $e^{\pm i\theta} = \cos\theta \pm i\sin\theta$, this relation is equivalent to $\cos(k_z^{\pm}\ell \mp \Delta\phi^{\mathrm{s}}/2) = \mathrm{tr}[M_{ki,0}^{\mathrm{s}}]/2$, whose inversion yields the explicit formula

$$k_z^{\pm}(\omega_i^{+}, \theta_i^{+}) = \frac{1}{\ell}\left[\arccos\left(\frac{\mathrm{tr}[M_{ki,0}^{\mathrm{s}}]}{2}\right) \pm \Delta\phi^{\mathrm{s}}/2\right]. \tag{4.15}$$

Similarly, in the temporal direction, the Bloch-Floquet theorem states

$$E^{\pm}(t+d) = e^{i\omega^{\pm}d}E^{\pm}(t), \tag{4.16}$$

where $\omega^{\pm}$ are the sought-after Bloch-Floquet frequencies. Successively substituting $E^{\pm}(t) = E_k^{\pm}(t_k)$ and $E^{\pm}(t+d) = E_i^{\pm}(t_i)$ from Fig. 4.2(b) and the first relation of (4.8) into this equation yields

$$\begin{bmatrix} E_i^{+} \\ E_i^{-} \end{bmatrix}_{t_i} = \mathrm{e}^{-i\omega^{\pm}d}\begin{bmatrix} E_k^{+} \\ E_k^{-} \end{bmatrix}_{t_k} = [M_{ij}^{\mathrm{t}}]\begin{bmatrix} E_k^{+} \\ E_k^{-} \end{bmatrix}_{t_k}. \tag{4.17}$$

A treatment of this (second equality) eigenvalue matrix equation analogous to that applied to the spatial case straightforwardly leads to the explicit formula

$$\pm\,\omega^{\pm}(\omega_i^+,\theta_i^+)=\frac{1}{d}\left(\arccos\left(\frac{\mathrm{tr}[M_{ik,0}^{\mathrm{t}}]}{2}\right)\pm\Sigma\phi^{\mathrm{t}}/2\right), \tag{4.18}$$

where, from (4.8) with Eqs. (4.6) and (4.9), we used

$$\det[M_{ik}^{\mathrm{t}}]=e^{i\Sigma\phi^{\mathrm{t}}} \tag{4.19}$$

and where

$$\mathrm{tr}[M_{ki}^{\mathrm{t}}]=e^{i\Sigma\phi^{\mathrm{t}}/2}\left(C_i^{\mathrm{t}}C_j^{\mathrm{t}}-AS_i^{\mathrm{t}}S_j^{\mathrm{t}}\right)=e^{i\Sigma\phi^{\mathrm{t}}/2}\mathrm{tr}[M_{ik,0}^{\mathrm{t}}], \tag{4.20}$$

with $\Sigma\phi^{\mathrm{t}}=\Sigma\phi_i^{\mathrm{t}}+\Sigma\phi_j^{\mathrm{t}}$, $C_n=\cos(\Delta\phi_n^{\mathrm{t}}/2)$, $S_n=\sin(\Delta\phi_n^{\mathrm{t}}/2)$,

$$\Sigma\phi_n^{\mathrm{t}}=(\omega_n^++\omega_n^-)d_i,\quad \text{and}\quad \Delta\phi_n^{\mathrm{t}}=(\omega_n^+-\omega_n^-)d_n, \tag{4.21}$$

and with A given in (4.12e).

Our orthogonal spatio-temporal treatment of the problem, illustrated in Fig. 4.1(d), has thus led to a pair of *separate* and *explicit* parametric (parameters ω_i^+ and θ_i^+) formulas for the Bloch-Floquet wavevectors and frequencies of the crystal, namely formulas (4.15) and (4.18), which represents the central result of the paper. These formulas offer the following benefits:

• Being separate and explicit, they offer maximal simplicity.

• Their duality, in terms of the substitutions $k_z^{\pm}\leftrightarrow\pm\omega^{\pm}$, $\ell\leftrightarrow d$, $\Delta\phi^{\mathrm{s}}\leftrightarrow\Sigma\phi^{\mathrm{t}}$ and $\Sigma\phi^{\mathrm{s}}\leftrightarrow\Delta\phi^{\mathrm{t}}$, reveals perfect spatio-temporal symmetry.

• Their arccos function term, being multi- and complex-valued, provides physical insight into the spatio-temporal periodicity and band structure of the crystal.

• The non-zero value of their parameters $\Delta\phi^{\mathrm{s}}$ and $\Sigma\phi^{\mathrm{t}}$, due to different forward and backward features, is a direct manifestation and measure of nonreciprocity [65, 135].

Figure 4.3 shows a typical dispersion diagram, corresponding the dispersion relation $\omega^{\pm}(k_z^{\pm})$, which has been plotted by varying the parameter ω_i^+ with parameter θ_i^+ fixed in Eqs. (4.15) and (4.18). Note the double average slope and gap position asymmetry, or nonreciprocity, in that diagram. The former asymmetry corresponds to unequal co- and contra-directional space-time weighted averaging [126], or Fresnel drag [40], while the latter asymmetry corresponds to different co- and contra-directional interference conditions due do the related Doppler red- and blue-shift.

Figure 4.4 shows an isofrequency diagram, i.e., $\omega(k_z,k_x)$ contour curves, corresponding to an ω-cut in the dispersion diagram of Fig. 4.3. This diagram has been obtained by the following

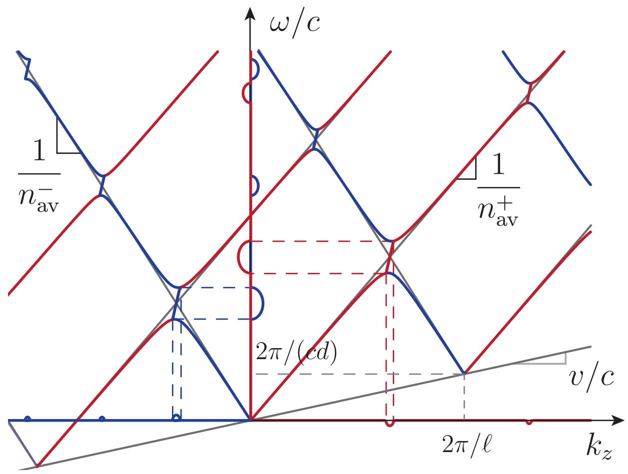

Figure 4.3 Dispersion diagram for $\epsilon_1 = 1$, $\epsilon_2 = 1.5$ $\mu_1 = \mu_2 = 1$, $\ell_1 = \ell_2 = \ell/2$, $v = 0.2c$ and $\theta_i^+ = 40°$, normalized to ℓ ($d = \ell/v$), with gray curves corresponding to the empty-lattice approximation found in App. B

procedure, varying this time the parameter θ_i^+: 1) find in (4.18) the values of ω_i^+ that satisfy $\omega^+ = \omega_0$ (red curves) and $\omega^- = \omega_0$ (blue curves); 2) insert these values into (4.15) to obtain the corresponding k_z^+ (red) and k_z^- (blue) values; 3) use the formula $k_x = \omega_i^+ n_i \sin\theta_i^+/c$ to determine the corresponding k_x values; 4) plot the corresponding $k_z^\pm(\omega_i^+, \theta_i^+)$ and $k_x(\omega_i^+, \theta_i^+)$ values.

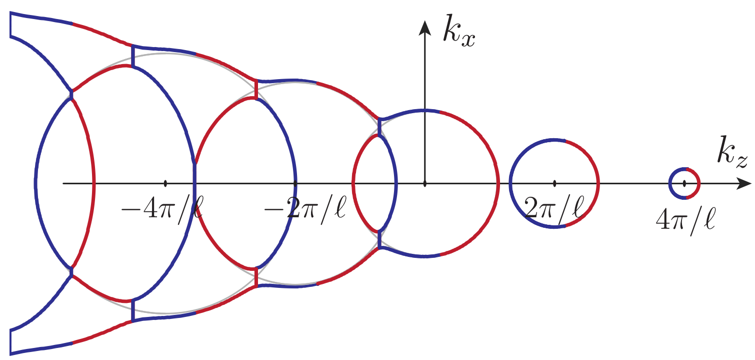

Figure 4.4 Isofrequency diagram for the same crystal parameters as Fig. 4.3 at $\omega^+ = \omega^- = \omega_0 = \pi$, with gray circles corresponding to empty-lattice approximation $(k_n + n2\pi/\ell) = (\omega_0 - n2\pi/d)n_{\mathrm{av}}/c$ [1, 2].

CHAPTER 5 ARTICLE 4: GENERALIZED FDTD SCHEME FOR THE SIMULATION OF ELECTROMAGNETIC SCATTERING IN MOVING STRUCTURES

Zoé-Lise Deck-Léger, Amir Bahrami, Zhiyu Li and Christophe Caloz

Published in Optics Express, Volume 31 Number 14, June 27, 2023

Abstract

Electromagnetic scattering in moving structures is a fundamental topic in physics and engineering. Yet, no general numerical solution to related problems has been reported to date. We introduce here a generalized FDTD scheme to remedy this deficiency. That scheme is an extension of the FDTD standard Yee cell and stencil that includes not only the usual, physical fields, but also auxiliary, unphysical fields allowing a straightforward application of moving boundary conditions. The proposed scheme is illustrated by four examples – a moving interface, a moving slab, a moving crystal and a moving gradient – with systematic validation against exact solutions.

5.1 Introduction

Moving structures are pervasive in electromagnetics. They may involve both moving bodies, such stars or vehicles, and moving perturbations, such as fluid or elastic waves. The category of moving-body structures has a nearly 300-year history and has lead to the discovery of many fundamental physical phenomena, such as Bradley aberration [4], Doppler frequency shifting [8], Fizeau dragging [6], relativity [113], magneto-electric coupling [129], medium bianisotropy [136] and gravity emulation [24]. The category of moving-perturbation structures is more recent and particularly amenable to practical applications; it produces effects such as parametric amplification [37, 44, 46], nonreciprocal transmission [38, 39], deflected reflection [47, 95], space-time frequency transitions [36, 137], pseudo Fizeau dragging [40, 126], spatiotemporal bandgaps [100, 106, 138] and accelerated metamaterial bending [54].

Surprisingly, no general numerical tool is currently available to simulate electromagnetic moving structures, whether of the moving-body or moving-perturbation type. The development of such a tool would be highly desirable to simulate the plethora of moving structures mentioned above as well as future ones, particularly the noncanonical – and typically more practical – structures that do not admit analytical solutions. This issue is well-known. There have been only two workarounds in the litterature so far [139–143], both based on the FDTD technique [144, 145], probably selected for its natural incarnation of both spatial and temporal variations in Maxwell's equations. However, one of these approaches is restricted to non-penetrable objects [139, 140], while the other one implies cumbersome Lorentz frame transformations [141–143].

We present here a novel, general and efficient FDTD scheme for simulating electromagnetic scattering in moving structures. That scheme, contrarily to that in [139,140], also applies to penetrable media, allowing hence to handle gradient structures and metamaterials [3, 146], without requiring problematic numerical transformations, contrarily to that in [141–143]. This scheme is based on a generalized Yee cell and stencil, which include not only the usual, physical fields, but also auxiliary, unphysical fields that carry the velocity information, so as to automatically satisfy the moving boundary conditions.

5.2 Types of Systems

The proposed method applies to both moving-matter and moving-perturbation media [126], the only difference between the two, in terms of modeling, being that in the former case, motion transforms media that are isotropic at rest into bianisotropic media [68,130], whereas in the latter case, motion alters the values of the permittivity or permeability parameters without affecting the isotropy of the medium [36, 94, 96]. Figure 5.1 depicts some of these structures[1], which will be used for illustration and validation purposes in Sec. 5.6: a simple interface [147] [Fig. 5.1(a)], a slab [148] [Fig. 5.1(b)], a bilayer crystal [Fig. 5.1(c)], which can be operated in the Bragg regime [37] or in the metamaterial (homogeneous) regime [146], and a gradient [27] [Fig 5.1(d)], all moving at a velocity v in a direction selected as being z in a Cartesian coordinate system. The different parts of these structures can naturally represent arbitrary bianisotropic media, with general tensor $\overline{\overline{\chi}} = \left[\overline{\overline{\epsilon}}, \overline{\overline{\xi}}; \overline{\overline{\zeta}}, \overline{\overline{\mu}}\right]$, which may be all different from each other and may be arbitrarily truncated in the xy-plane. Note that all these structures can be seen as a succession of interfaces, including the gradient considering a decomposition in subwavelength slabs. For this reason, we shall focus on an interface in the next section, which deals with boundary conditions.

[1]In the case of moving-perturbation, these structures are essentially *traveling-wave* modulation-type structures, while *standing-wave* modulation-type structures, such as those studied in [99, 138], which consist combinations of purely spatial and purely temporal interfaces can be handled by standard FDTD algorithm. Indeed, the FDTD algorithm naturally enforces continuity of the tangential **E** and **H** fields at stationary interfaces and continuity of **D** and **B** fields at temporal interfaces.

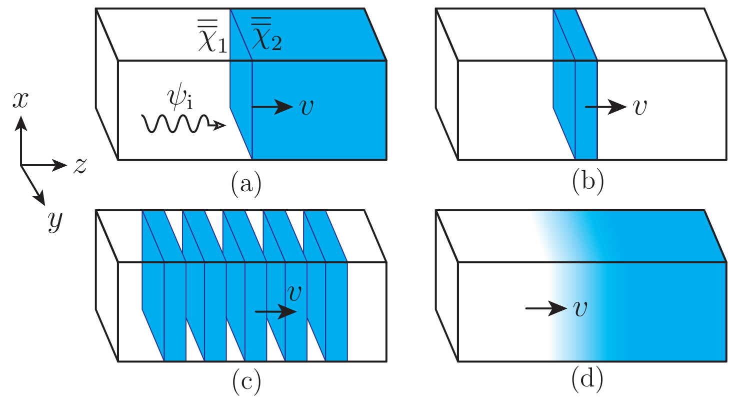

Figure 5.1 Types of moving structures, of either the moving-matter or moving-perturbation type, that can be simulated by the proposed generalized FDTD scheme. (a) Simple interface. (b) Slab. (c) Bilayer crystal. (d) Gradient.

5.3 Generalized Yee Cell

The boundary conditions at a moving interface, whether associated to moving modulation or moving matter, read [23, 112]

$$\hat{\mathbf{n}} \times (\mathbf{E}_2^* - \mathbf{E}_1^*) = 0, \tag{5.1a}$$

$$\hat{\mathbf{n}} \times (\mathbf{H}_2^* - \mathbf{H}_1^*) = \mathbf{J}_{\rm s}, \tag{5.1b}$$

$$\hat{\mathbf{n}} \cdot (\mathbf{D}_2 - \mathbf{D}_1) = \rho_{\rm s}, \tag{5.1c}$$

$$\hat{\mathbf{n}} \cdot (\mathbf{B}_2 - \mathbf{B}_1) = 0, \tag{5.1d}$$

with

$$\mathbf{E}^* = \mathbf{E} + \mathbf{v} \times \mathbf{B} \quad \text{and} \quad \mathbf{H}^* = \mathbf{H} - \mathbf{v} \times \mathbf{D}, \tag{5.2}$$

where 1 and 2 label the media at the two sides the interface [as in Fig. 5.1(c)], $\mathbf{E}$, $\mathbf{H}$, $\mathbf{D}$, $\mathbf{B}$ are the usual electromagnetic fields, $\mathbf{J}_{\rm s}$ and $\rho_{\rm s}$ are the usual surface current and charge densities, respectively, $\hat{\mathbf{n}}$ is the unit vector normal to the interface pointing towards medium 1, and $\mathbf{v}$ is the velocity of the interface. Note that these conditions, as expected, reduce to the stationary boundary conditions for $\mathbf{v} = 0$, viz., $\hat{\mathbf{n}} \times (\mathbf{E}_2 - \mathbf{E}_1) = 0$, $\hat{\mathbf{n}} \times (\mathbf{H}_2 - \mathbf{H}_1) = \mathbf{J}_{\rm s}$, $\hat{\mathbf{n}} \cdot (\mathbf{D}_2 - \mathbf{D}_1) = \rho_{\rm s}$ and $\hat{\mathbf{n}} \cdot (\mathbf{B}_2 - \mathbf{B}_1) = 0$.

The fields in Eq. (5.2) may decomposed into tangential and normal components with respect to the interface. The tangential components are

$$\mathbf{E}^*_{\tan} = \mathbf{E}_{\tan} + \mathbf{v} \times \mathbf{B} - (\hat{\mathbf{n}} \cdot (\mathbf{v} \times \mathbf{B}))\hat{\mathbf{n}} \quad \text{and} \quad \mathbf{H}^*_{\tan} = \mathbf{H}_{\tan} - \mathbf{v} \times \mathbf{D} - (\hat{\mathbf{n}} \cdot (\mathbf{v} \times \mathbf{D}))\hat{\mathbf{n}}, \tag{5.3a}$$

while the normal components are

$$\mathbf{E}^*_{\text{norm}} = \mathbf{E}_{\text{norm}} + (\hat{\mathbf{n}} \cdot (\mathbf{v} \times \mathbf{B}))\hat{\mathbf{n}} \quad \text{and} \quad \mathbf{H}^*_{\text{norm}} = \mathbf{H}_{\text{norm}} + (\hat{\mathbf{n}} \cdot (\mathbf{v} \times \mathbf{D}))\hat{\mathbf{n}}. \tag{5.3b}$$

In the case where the interface is perpendicular to the direction of motion, i.e., $\mathbf{n}\|\mathbf{v}$, the right-most terms in the right hand sides of Eqs. (5.3a) and Eqs. (5.3b) vanish. This is the scenario that is represented in Fig. 5.1 and that will be assumed in the sequel of the paper[2]. The paper will further assume non-conducting interfaces, and hence $\mathbf{J}_\text{s} = \rho_\text{s} = 0$ in Eq. (5.1).

The dynamic boundary conditions (5.1) differ from the static or stationary boundary equations only insofar as they involve the auxiliary fields $\mathbf{E}^*_{1,2}$ and $\mathbf{H}^*_{1,2}$ instead of the fields $\mathbf{E}_{1,2}$ and $\mathbf{H}_{1,2}$, whose tangential components include velocity-dependent extra terms [Eq. (5.3a)]. This observation suggests the generalization of the standard Yee cell [148] to a Yee cell with correspondingly modified $\mathbf{E}_{\tan}$ and $\mathbf{H}_{\tan}$ fields, without alteration of the conventional electric and magnetic field staggering arrangement. The result is shown in Fig. 5.2, for a pair of generalized Yee cells separated by a moving interface. The so-defined generalized Yee cell straightforwardly allows to satisfy the field continuity conditions at a moving interface, i.e., Eqs. (5.1a) and (5.1b), by having the field components E^*_x, E^*_y and H_z uniquely defined at the permittivity interface of Fig. 5.2 (or H^*_x, H^*_y and E_z in the case of a corresponding magnetic interface).

This simple generalization of the Yee cell is the core idea of the paper. This idea might a priori appear to be trivial, but it is not so trivial insofar as it implies a *mixture of physical and unphysical fields*, namely, as seen in Eqs. (5.1) and (5.3), the physical fields $\mathbf{D}$, $\mathbf{B}$, $\mathbf{E}_\text{norm}$ and $\mathbf{H}_\text{norm}$ and the unphysical fields $\mathbf{E}^*_{\tan}$ and $\mathbf{H}^*_{\tan}$, which will also imply unphysical mixed-field electromagnetic equations. This strange situation is somewhat reminiscent to the unphysical anisotropic media appearing in Bérenger's Perfect Matched Layers (PMLs) [151] and, as the PMLs, it does not pose any fundamental problem. The corresponding unphysical Maxwell's equations constitutive relations, which will be derived and discretized in Sec. 5.4 for establishing the generalized FDTD update equations, are mathematical mappings of the physical Maxwell's equations via the simple changes of variable in Eqs. (5.3), and the physical fields $\mathbf{E}$ and $\mathbf{H}$ can be found anytime from the auxiliary fields by simply inverting

[2] If we had $\mathbf{n}\nparallel\mathbf{v}$, the interface would be slanted with respect to the motion direction. Related problems were treated analytically in [149, 150]

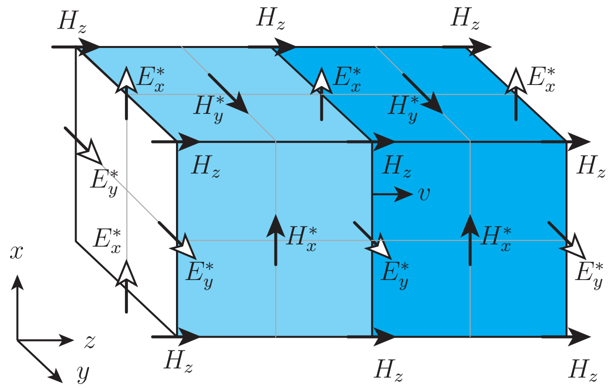

Figure 5.2 Pair of generalized Yee cells, separated by a moving interface [Fig. 5.1(a)], with the generalization consisting in the substitution of the tangential physical fields $\mathbf{E}$ and $\mathbf{H}$ by the corresponding tangential auxiliary fields $\mathbf{E}^*$ and $\mathbf{H}^*$ in Eq. (5.2).

these relations.

5.4 Generalized Scheme

In this section, we shall derive the generalized FDTD scheme corresponding to the generalized Yee cell established in Sec. 5.3. This scheme must, of course, model the physics of the problem, and hence follow the usual Maxwell-Faraday and Maxwell-Ampère equations,

$$\frac{\partial \mathbf{B}}{\partial t} = -\nabla \times \mathbf{E} \quad \text{and} \quad \frac{\partial \mathbf{D}}{\partial t} = \nabla \times \mathbf{H}, \tag{5.4}$$

as well as the general constitutive relations,

$$\mathbf{D} = \overline{\overline{\epsilon}}(\mathbf{r} - \mathbf{v}t) \cdot \mathbf{E} + \overline{\overline{\xi}}(\mathbf{r} - \mathbf{v}t) \cdot \mathbf{H} \quad \text{and} \quad \mathbf{B} = \overline{\overline{\zeta}}(\mathbf{r} - \mathbf{v}t) \cdot \mathbf{E} + \overline{\overline{\mu}}(\mathbf{r} - \mathbf{v}t) \cdot \mathbf{H}, \tag{5.5}$$

whose bianisotropic form [115] pertains to moving matter[3] and which reduce to simple homoisotropic relations $\left(\overline{\overline{\epsilon}} = \epsilon,\ \overline{\overline{\mu}} = \mu,\ \overline{\overline{\xi}} = \overline{\overline{\zeta}} = 0\right)$ in the case of moving modulation [36,94,96]. In order to apply the generalized Yee cell established in Sec. 5.3, we must express the fields $\mathbf{E}$ and $\mathbf{H}$ in Eqs. (5.4) and (5.5) in terms of the fields $\mathbf{E}^*$ and $\mathbf{H}^*$ using Eq. (5.2). This results into the mixed-field Maxwell's equations

$$\frac{\partial \mathbf{B}}{\partial t} = -\nabla \times \mathbf{E}^* + \nabla \times (\mathbf{v} \times \mathbf{B}), \tag{5.7a}$$

$$\frac{\partial \mathbf{D}}{\partial t} = \nabla \times \mathbf{H}^* + \nabla \times (\mathbf{v} \times \mathbf{D}), \tag{5.7b}$$

and constitutive relations

$$\mathbf{D} = \overline{\overline{\epsilon}}(\mathbf{r} - \mathbf{v}t) \cdot (\mathbf{E}^* - \mathbf{v} \times \mathbf{B}) + \overline{\overline{\xi}}(\mathbf{r} - \mathbf{v}t) \cdot (\mathbf{H}^* + \mathbf{v} \times \mathbf{D}), \tag{5.8a}$$

$$\mathbf{B} = \overline{\overline{\zeta}}(\mathbf{r} - \mathbf{v}t) \cdot (\mathbf{E}^* - \mathbf{v} \times \mathbf{B}) + \overline{\overline{\mu}}(\mathbf{r} - \mathbf{v}t) \cdot (\mathbf{H}^* + \mathbf{v} \times \mathbf{D}). \tag{5.8b}$$

From this point, we shall restrict our developments, for the sake of simplicity and without any loss of generality, to structures that are i) based on moving modulation (as opposed to moving matter), ii) one-dimensional (1D) and iii) illuminated by a plane wave propagating in the direction of the modulation (i.e., normal to the interface(s)). Using a Cartesian coordinate system with z corresponding to the direction of the modulation, the non-zero field components reduce to E_x and H_y and Eqs. (5.7) and (5.8) become then

$$\frac{\partial B_y}{\partial t} = -\frac{\partial E_x^*}{\partial z} - v\frac{\partial B_y}{\partial z}, \tag{5.9a}$$

$$\frac{\partial D_x}{\partial t} = -\frac{\partial H_y^*}{\partial z} - v\frac{\partial D_x}{\partial z}, \tag{5.9b}$$

and

$$D_x = \epsilon(z - vt)\left(E_x^* + vB_y\right), \tag{5.10a}$$

[3]In this case, for motion in the z direction ($\mathbf{v} = v\hat{\mathbf{z}}$), the tensors in Eq. (5.5) are [115]

$$\overline{\overline{\epsilon}} = \epsilon' \begin{bmatrix} \alpha & 0 & 0 \\ 0 & \alpha & 0 \\ 0 & 0 & 1 \end{bmatrix}, \quad \overline{\overline{\mu}} = \mu' \begin{bmatrix} \alpha & 0 & 0 \\ 0 & \alpha & 0 \\ 0 & 0 & 1 \end{bmatrix}, \quad \overline{\overline{\xi}} = \begin{bmatrix} 0 & \chi/c & 0 \\ -\chi/c & 0 & 0 \\ 0 & 0 & 0 \end{bmatrix}, \quad \overline{\overline{\zeta}} = \overline{\overline{\xi}}^T,$$

with

$$\alpha = \frac{1-\beta^2}{1-\beta^2 n'^2}, \qquad \chi = \beta\frac{1-n'^2}{1-\beta^2 n'^2}, \qquad \beta = v/c \qquad \text{and} \qquad n'/c = \sqrt{\epsilon'\mu'},$$

where ϵ' and μ' are constant scalars that represent the permittivity and permeability of the medium at rest ($v = 0$), which is assumed to be isotropic, nondispersive and linear.

$$B_y = \mu(z - vt)\left(H_y^* + vD_x\right), \tag{5.10b}$$

where we have used the fact that the mapping (5.2) preserves the polarization in the 1D case[4], so that only the star field components E_x^* and H_y^*, corresponding to E_x and H_y, are involved,

We can now proceed to the discretization of Eqs. (5.9) and (5.10). The static ($v = 0$) parts can be discretized in the usual fashion [145], which yields

$$B_y|_{k+\frac{1}{2}}^{n} = B_y|_{k+\frac{1}{2}}^{n-1} - S\left(E_x^*|_{k+1}^{n-\frac{1}{2}} - E_x^*|_{k}^{n-\frac{1}{2}}\right) - v\Delta t\frac{\partial B_y}{\partial z}, \tag{5.11a}$$

$$D_x|_{k}^{n+\frac{1}{2}} = D_x|_{k}^{n-\frac{1}{2}} - S\left(H_y^*|_{k+\frac{1}{2}}^{n} - H_y^*|_{k-\frac{1}{2}}^{n}\right) - v\Delta t\frac{\partial D_x}{\partial z}, \tag{5.11b}$$

and

$$E_x^*|_{k}^{n+\frac{1}{2}} = \frac{D_x|_{k}^{n+\frac{1}{2}}}{\epsilon|_{k}^{n+\frac{1}{2}}} - vB_y, \tag{5.11c}$$

$$H_y^*|_{k+\frac{1}{2}}^{n} = \frac{B_y|_{k+\frac{1}{2}}^{n}}{\mu|_{k+\frac{1}{2}}^{n}} - vD_x, \tag{5.11d}$$

where $S = \Delta t/\Delta z$.

In contrast, the dynamic ($v \neq 0$) terms, which have not been discretized yet in Eqs. (5.11), require a special treatment for the numerical stability and minimal dispersion of the overall scheme. We empirically found that the discretization choices given in Tab. 5.1 are appropriate in these regards. Note that these schemes are different for positive velocities, i.e., $\mathbf{v}\|\hat{\mathbf{z}}$ or $v > 0$ and negative velocities, $\mathbf{v}\| - \hat{\mathbf{z}}$ or $v < 0$.

Figure 5.3 shows the stencil of the overall proposed generalized FDTD scheme, which provides a handy pictorial representation of Eqs. (5.11) with Eqs. (5.12)-(5.15).

5.5 Stability

In this section, we demonstrate the stability of the generalized scheme presented in Sec. 5.4 using von Neumann's approach [152]. This approach consists in inserting plane-wave test

[4]To show this, we insert $\mathbf{B} = -\int (\nabla \times \mathbf{E})\,\mathrm{d}t$, from (5.4), into (5.2), which yields, using the vectorial identity $\mathbf{A} \times (\nabla \times \mathbf{B}) = \nabla(\mathbf{A} \cdot \mathbf{B}) - (\mathbf{A} \cdot \nabla)\mathbf{B} - (\mathbf{B} \cdot \nabla)\mathbf{A} - \mathbf{B} \times (\nabla \times \mathbf{A})$,

$$\mathbf{E}^* = \mathbf{E} - \int (\mathbf{v} \times (\nabla \times \mathbf{E}))\,\mathrm{d}t = \mathbf{E} - \int (\nabla(\mathbf{v} \cdot \mathbf{E}) - (\mathbf{v} \cdot \nabla)\mathbf{E} - (\mathbf{E} \cdot \nabla)\mathbf{v} - \mathbf{E} \times (\nabla \times \mathbf{v}))\,\mathrm{d}t.$$

The last two last terms in the last expression both vanish in the assumed regime of constant velocity. Given $\mathbf{E} = E_x\hat{\mathbf{x}}$ and $\mathbf{v} = v\hat{\mathbf{z}}$, the term with $\mathbf{v} \cdot \mathbf{E}$ also vanishes since $\mathbf{v} \perp \mathbf{E}$. Finally, the term $(\mathbf{v} \cdot \nabla)\mathbf{E}$ reduces to $\hat{\mathbf{x}}\partial E_x/\partial z$ and is hence parallel to $\mathbf{E}$. Thus, $\mathbf{E}^*\|\mathbf{E}$. It may be similarly shown that $\mathbf{H}^* \parallel \mathbf{H}$.

Positive velocity ($v > 0$)		Negative velocity ($v < 0$)	
$\dfrac{\partial B_y}{\partial z} = \dfrac{B_y\vert_{k+\frac{1}{2}}^{n-1} - B_y\vert_{k-\frac{1}{2}}^{n-1}}{\Delta z}$	(5.12a)	$\dfrac{\partial B_y}{\partial z} = \dfrac{B_y\vert_{k+\frac{3}{2}}^{n-1} - B_y\vert_{k+\frac{1}{2}}^{n-1}}{\Delta z}$	(5.12b)
$\dfrac{\partial D_x}{\partial z} = \dfrac{D_x\vert_{k}^{n-1/2} - D_x\vert_{k-1}^{n-1/2}}{\Delta z}$	(5.13a)	$\dfrac{\partial D_x}{\partial z} = \dfrac{D_x\vert_{k+1}^{n-1/2} - D_x\vert_{k}^{n-1/2}}{\Delta z}$	(5.13b)
$B_y = \dfrac{B_y\vert_{k-1/2}^{n} + B_y\vert_{k-3/2}^{n}}{2}$	(5.14a)	$B_y = \dfrac{B_y\vert_{k+3/2}^{n} + B_y\vert_{k+1/2}^{n}}{2}$	(5.14b)
$D_x = \dfrac{D_x\vert_{k+1}^{n-1/2} + D_x\vert_{k}^{n-1/2}}{2}$	(5.15a)	$D_x = \dfrac{D_x\vert_{k+1}^{n-1/2} + D_x\vert_{k}^{n-1/2}}{2}$	(5.15b)

Table 5.1 Discretization of the dynamic terms in Eqs. (5.11).

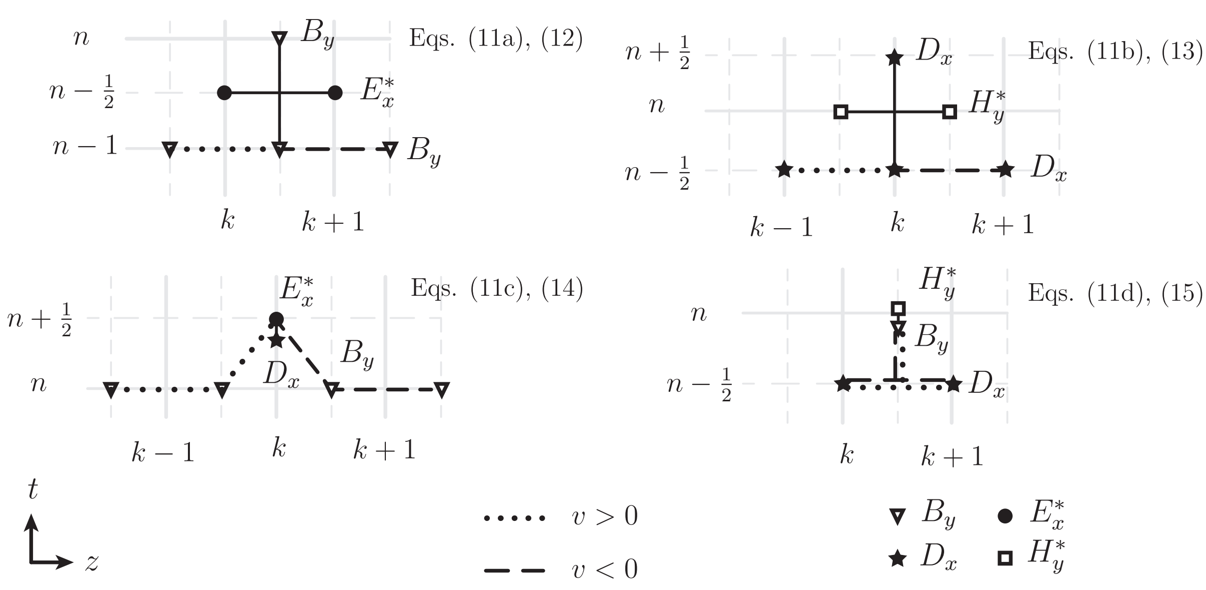

Figure 5.3 FDTD stencil corresponding to the FDTD scheme in Eqs. (5.11) with Eqs. (5.12)-(5.15).

fields with the form

$$\Psi|_k^n = \Psi_0 \xi^k \zeta^n, \quad \text{where} \quad \xi = e^{ik_z\Delta z} \quad \text{and} \quad \zeta = e^{-\alpha\Delta t} \tag{5.14}$$

into the update equations and determining the condition under which the $\zeta(\xi)$ solution of the resulting matrix system is smaller than one – but as close as possible to one to avoid numerical attenuation[5].

Inserting the test fields of the above form into Eqs. (5.11) with Eqs. (5.12)(a)-(5.15)(a) or (5.12)(b)-(5.15)(b), setting the determinant of the matrix associated with the resulting homogeneous system of equations to zero, and finding the ζ roots of the corresponding characteristic polynomial yields (see details in Appendix 5.5)

$$\begin{aligned}\zeta_\pm = &\frac{\xi^{-3}}{4n^2}\left[Sd\xi^4 + 4\left(b - 4S^2\right)\xi^3 + S\left(3\beta n^2 + 2S\right)\xi^2 - \beta n^2 S\xi\right] \\ &\pm \frac{\xi^{-2}}{4n^2}(1-\xi)S\sqrt{\xi^4 d^2 + 4\left(b - 2S^2\right)\xi^3 + 4(n^4\beta^2 - 6n^2 S\beta - 2S^2)\xi^2 - 4\beta^2 n^2 S\xi}\end{aligned}, \tag{5.15}$$

where $\beta = v/c$, $\xi = e^{ik_z\Delta z}$, $b = n^2(4-3\beta S)$ and $d = 2S+\beta n^2$. Setting $\zeta = 1$ in Eq. (5.15) provides the stability threshold of the scheme, with stability achieved for $\zeta < 1$ (and unstability for $\zeta > 1$).

The fact that the stability analysis admits a *double solution*, $\zeta_\pm$ [Eq. (5.15)], may a priori appear suprising, given that ζ solutions are usually unique. However, this can be understood by realizing that waves that are *co-moving and contra-moving* with respect to the modulation see different numerical "landscapes". Specifically, if $v > 0$, then the scheme uses Eq. (5.12a)-(5.15a) [first column in Tab. 5.1] for the dynamic parts, which correspond to the dotted segments (with the dashed segment removed) in Fig. 5.3; the resulting stencils for the first three equations [Eqs. (5.11a)-(5.11c) with Eqs. (5.12a)-(5.14a)] are clearly asymmetric with respect the z direction and therefore, although the stencil for the fourth equation [Eq. (5.11d) with Eq. (5.15a)] is symmetric, the stencil is *overall asymmetric* with respect to z, so that co-moving and contra-moving waves will see different stencils. A similar conclusion holds for the case $v < 0$, so we expect that, for a given choice of the modulation direction, ζ_+ will correspond to one of the two (co-moving or contra-moving) regime, while ζ_- will correspond to the other regime.

The two regimes may be identified by comparing the signs of the spatial and temporal phases

[5]In Eq. (5.14), one must be carefull not to confuse k_z, the z-component of the wavenumber, with k, the spatial index appearing in the FDTD update equations. No related ambiguity should exist in the paper insofar as the two quantities are always distinguishable from each other by the presence or absence of the z subscript.

of the test plane-wave in Eq. (5.14), with the spatial phase and temporal phase residing in ξ and $\zeta_\pm$, respectively. For this purpose, let us consider a specific numerical position and time, say for simplicity $k = 1$ and $n = 1$, and analyze the test plane-wave for the two possible propagation directions. We have, upon writing $\alpha_\pm = \omega_{\mathrm{i}\pm} \pm i\omega_{\mathrm{r}\pm}$ in $\zeta_\pm$ (with $\omega_{\mathrm{i}\pm} > 0$ assuming stability),

$$\begin{aligned}\frac{\Psi|_{k=1}^{n=1}}{\Psi_0} = \xi\zeta_\pm &= e^{ik_z\Delta z-\alpha_\pm\Delta t} = e^{ik_z\Delta z-(\omega_{\mathrm{i}\pm}\pm i\omega_{\mathrm{r}\pm})\Delta t} \\ &= e^{-\omega_{\mathrm{i}\pm}\Delta t}e^{i(k_z\Delta z\mp\omega_{\mathrm{r}\pm}\Delta t)} = e^{-\omega_{\mathrm{i}\pm}\Delta t}e^{ik_z\Delta z}e^{\mp i\omega_{\mathrm{r}\pm}\Delta t} \\ &= e^{ik_z\Delta z}e^{-\omega_{\mathrm{i}\pm}\Delta t}\left[\cos(\omega_{\mathrm{r}\pm}\Delta t) \mp i\sin(\omega_{\mathrm{r}\pm}\Delta t)\right] = \xi\left(\zeta_{\mathrm{r}\pm} \mp i\zeta_{\mathrm{i}\pm}\right).\end{aligned} \tag{5.16}$$

In these relations, the first expression of the second line reveals that the upper sign, which is associated with ζ_+, corresponds to a forward wave, propagating in the $+z$ direction, while the lower sign, which is associated with ζ_-, corresponds to a backward wave, so that ζ_+ and ζ_- respectively correspond to the co-moving and contra-moving regimes for $v > 0$ (and conversely for $v < 0$). Note that the scheme must be stable for both waves, since typical problems involve both of them[6]. The stability criterion should then be taken as that corresponding to the more restrictive of the two ζ solutions.

We shall now show that the $\pm$ signs in Eq. (5.16) correspond to $\pm$ signs in Eq. (5.15). We have to do this numerically because we have not been able to separate the real and imaginary parts of ζ in Eq. (5.15) as we did in Eq. (5.16). Inserting the parameters $S = 0.5$, $\beta = 0.3$, $\epsilon = 4$, $\mu = 1$ and $\Delta z k_z = 2\pi/5$ into Eq. (5.15) yields $\zeta_+ = 0.925 - i0.33$ and $\zeta_- = 0.917 + i0.23$, which is indeed consistent with Eq. (5.16), and hence confirms the consistency of the $\pm$ indices of ζ in Eqs. (5.15) and (5.16). Incidentally, the magnitudes of the ζ's, as apparent in the last equation of Eqs. (5.14), represent the levels of the wave, which are here $|\zeta_+| = 0.98$ and $|\zeta_-| = 0.95$, which reveals that the co-moving wave is less attenuated than the contra-moving wave.

Figure 5.4 plots the attenuation rate $\alpha = \ln(\zeta)/\Delta t$ versus the meshing density $N_\lambda = \lambda_0/\Delta z = 2\pi/(k_z\Delta z) = i2\pi/\ln(\xi)$ obtained by Eq. (5.15) and by FDTD simulations, along with FDTD-simulated space-time field evolutions for two meshing densities, for the case $v > 0$ [corresponding to the stencil with Eqs. (5.12a)-(5.15a)]. The FDTD attenuation results closely match the attenuation results predicted by the analytical stability analysis, with distinct levels corresponding, as expected, to the co-moving and contra-moving regimes. Here, with the choice $v > 0$, the appropriate (more restrictive) criterion corresponds to that for the

[6]This is even true for a simple mismatched moving interface, where the incident and transmitted waves are co-moving and the reflected wave is contra-moving if the incident wave propagates in the direction of the modulation.

co-moving waves (ζ_+), whereby the contra-moving (ζ_-) waves will experience an extra level of numerical attenuation compared to what would be required if they were alone. Symmetrically identical results (not shown) are obtained for the case $v > 0$, corresponding to the stencil with Eqs. (5.12b)-(5.15b).

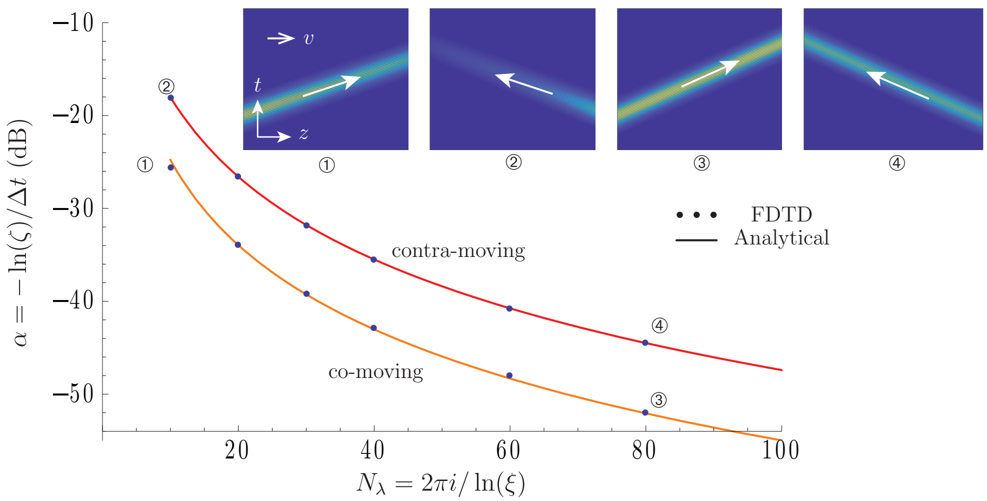

Figure 5.4 Attenuation rate versus meshing density obtained by Eq. (5.15) and by FDTD simulation (taking field ratios at different times), for $S = 0.5$, $v = 0.3c$ ($v > 0$, first column in Tab. 5.1), $\epsilon = 1$ and $\mu = 1$. The insets show FDTD-simulated space-time evolution of a 3λ-wide Gaussian pulse modulated by a harmonic wave of wavelength $\lambda = 2\pi/k_z$ and period $T = 2\pi/\omega$, over a distance of 20λ and time of $45T$, for the mesh densities $N_\lambda = 10$ and $N_\lambda = 80$.

5.6 Illustrative and Validating Examples

Figures 5.5, 5.6, 5.7 and 5.8 provide illustrative and validating examples, corresponding to Figs. 5.1(a), (b), (c) and (d), for the problems of electromagnetic scattering at a moving interface, a moving slab, a moving cystal and a moving gradient, respectively.

In all the cases (Figs. 5.5, 5.6, 5.7 and 5.8) and for all the quantities (incident, reflected and transmitted electric fields, and reflection and transmission coefficients), excellent agreement is observed between the numerical results of the proposed generalized FDTD scheme and the analytical results (given in Appendix C), with minor observable discrepancies in the scattering coefficients, which are explained by the limited bandwidth of the test pulse.

The physics of the dynamic scattering observed in Figs. 5.5, 5.6, 5.7 and 5.8 involves reflection Doppler frequency shifting, transmission index contrast frequency shifting, co-moving attenuation, contra-moving amplification, multiple space-time scattering and space-time stopbands.

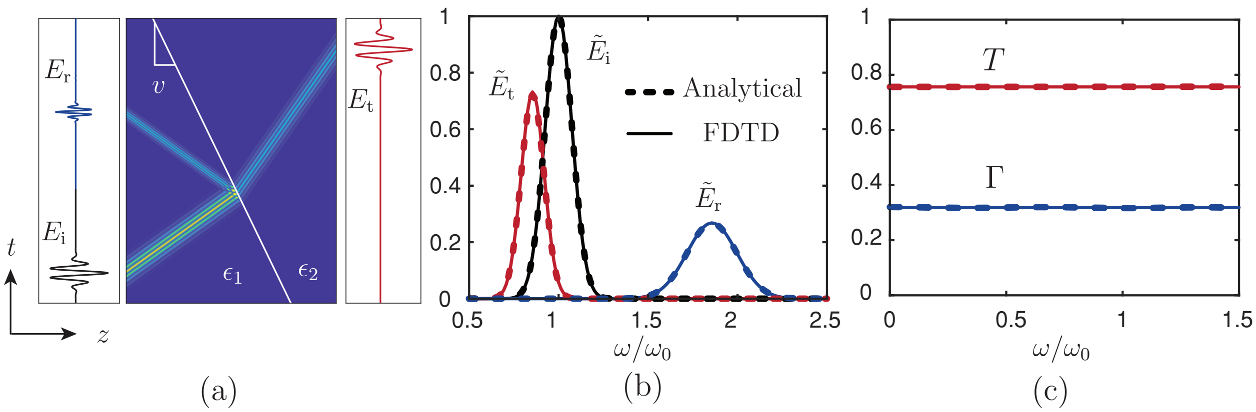

Figure 5.5 Results for a contra-moving interface [Fig. 5.1(a)], for the physical parameters $v = -0.3c$, $\epsilon_1 = 2$, $\epsilon_2 = 4$ and $\mu = 1$, and numerical parameters $S = 0.2$ and $\Delta z = \lambda_0/150$. The analytical solutions are given in Appendix C. (a) Space-time evolution of the electric field for a modulated Gaussian pulse ($E_\mathrm{i} = e^{-i\omega_\mathrm{i}t}e^{-(t/\tau_\mathrm{i})^2}$), obtained by combining spatial waveforms at successive times, with input and output temporal waveforms plotted on the sides. (b) Spectrum of the input and output fields, obtained by Fourier transforming the waveforms sampled at the input and output positions in (a). (c) Transmission and reflection coefficients, obtained by taking the ratios of the Fourier transforms of the appropriate fields for a short (wide-band) incident pulse.

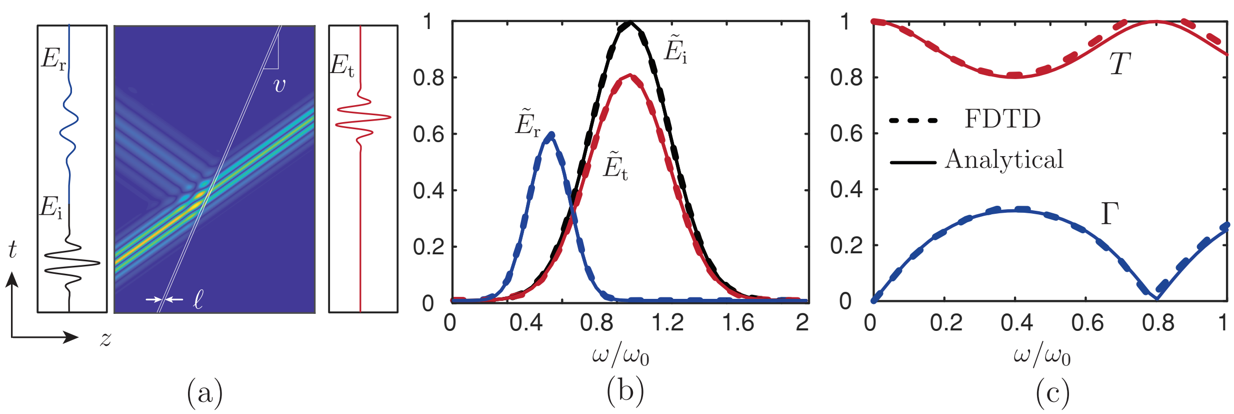

Figure 5.6 Same as in Fig. 5.5 but for a co-moving slab [Fig. 5.1(b)], with velocity $v = 0.3c$, $\epsilon_2 = 4$ and length $\ell = \frac{\lambda_0}{4n_2}\frac{1+n_2\beta}{1-n_1\beta}$, corresponding to a space-time quarter-wave slab [3].

All these effects have been described elsewhere [3,96,97] and are therefore not discussed here.

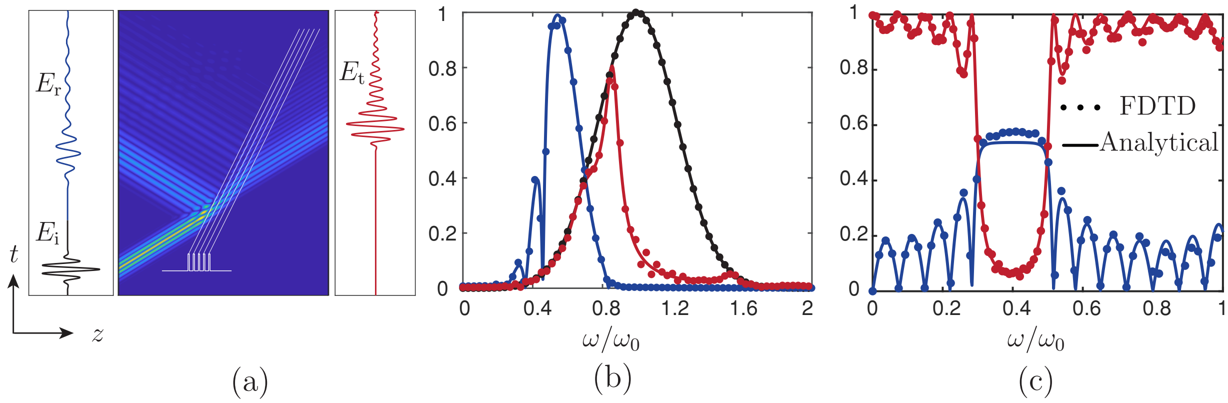

Figure 5.7 Same as in Fig. 5.5 but for a co-moving bilayer crystal [Fig. 5.1(c)], consiting of 5 unit-cells each made of two space-time quarter-wave slabs $\epsilon_1 = 1$, $\epsilon_2 = 4$, $\ell_1 = \frac{\lambda_0}{4n_1}\frac{1+n_1\beta}{1-n_2\beta}$, $\ell_2 = \frac{\lambda_0}{4n_2}\frac{1+n_2\beta}{1-n_1\beta}$,

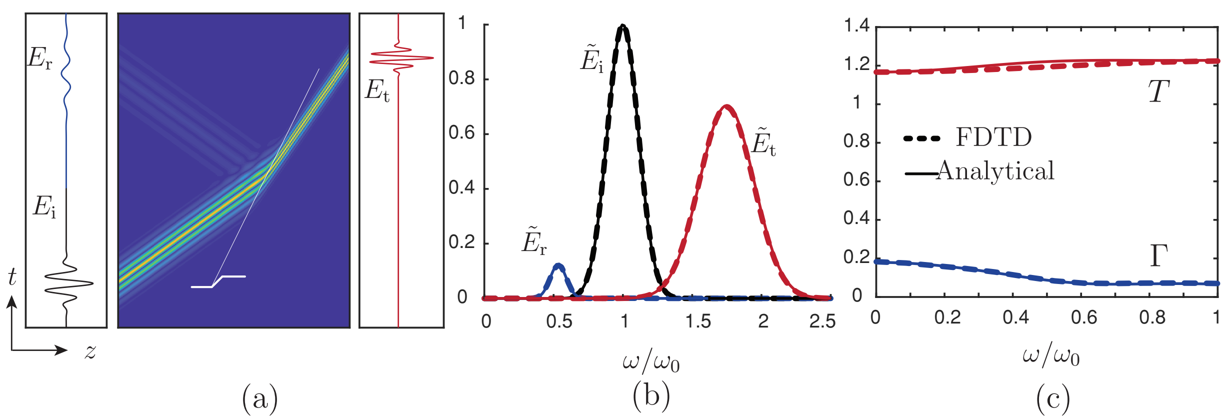

Figure 5.8 Same as in Fig. 5.5 but for a co-moving gradient [Fig. 5.1(d)], corresponding to a linear increase of the permittivity from ϵ_1 to ϵ_2 over a length of $\ell = \lambda_0/2$.

5.7 Conclusion

We have presented a generalized FDTD scheme that can simulate electromagnetic scattering in a great diversity of moving-medium problems. This scheme, using a combination of physical and auxiliary fields to satisfy moving boundary conditions in a natural fashion, is both simple and powerful. It fills an fundamental and important gap in the toolbox of electromagnetic computational techniques and is hence expected to find wide applications, particularly in the emergent area of space-time metamaterials.

CHAPTER 6 CONCLUSION AND RECOMMENDATIONS

6.1 Summary of Contributions

This thesis has presented a few contributions, which we list here in order of appearance

- Impedance diagrams for the estimation of scattering coefficients from moving structures, Sec. 2.5;
- Demonstration of symmetric transmitted waves in interluminal regime, Sec. 2.6;
- Extension of the Stokes principle to spacetime interfaces, Sec. 3.3;
- Bragg-like description of intereference phenomenology, Sec. 3.4;
- Correction of the empty-lattice approximation of the dispersion diagrams, Sec. 3.5;
- Space-time symmetric modelling of space-time modulated crystals, Ch. 4;
- Modification of the finite-difference time-domain scheme which correctly handles moving structures, Ch. 5.

6.2 Future Research

In this section, we identify potential future directions.

6.2.1 Dispersive space-time structures

The structures studied until now exhibited no dispersion. This is satisfactory as long as all incident and scattered wave frequencies are within a frequency range where the medium parameters are relatively constant, i.e. far from any medium resonance. Our work could be extended to dispersive structures in the following ways:

Impedance diagrams for dispersive moving structures– Temporally-dispersive structures that are set in motion exhibit spatial dispersion [68], see for instance App. D for a brief demonstration. This spatial dispersion is reflected in the isofrequency diagrams, but it would be interesting to explore how the it affects the impedance patterns of Ch. 2.

Bragg-like description of unusual gaps– In space-time-modulated periodic dispersive structures, unusual gaps may appear due to the presence of two forward waves having different velocities [153, 154]. Applying a Bragg-like description could help explain the behavior at these unusual gaps.

FDTD for modulated dispersive structures– A generalization of the proposed FDTD method to include temporal dispersion would be be advantageous to model all space-time-modulated dispersive structures.

6.2.2 Interluminal-velocity regime

The interluminal-velocity regime is the most interesting velocity regimes, and the least understood. It corresponds to the regime where the isofrequencies transform from elliptical to hyperbolic, the regime with highest amplification and highest frequency transitions, and the regime where a sharp interface may lead to two transmitted waves instead of one. Once the scattering from a single interluminal interface is elucidated, all the analytical works we presented could be extended to the interluminal regime.

The FDTD generalized scheme presented in Ch. 5 is numerically unstable at interluminal velocities. A future work would be the modification of the stencils so that the numerical instability disappears.

6.2.3 Implementations

Implementations of moving-matter structures would be not only difficult to engineer, they would also theoretically be associated with spontaneous radiation: a stationary charge in a moving dielectric at interluminal velocities would radiate energy through Cherenkov radiation [155], and a bounded moving polarizable medium would lead to spontaneous light emission even in the presence of an infinitesimally small optical field [156].

For these reasons, it is far more practical to implement modulated structures. At radio frequencies, space-time modulations have been successfully implemented on microstrip lines [31, 157, 158] and acousto-optic devices [159]. However in the optical regime, the challenges in achieving high-contrast change and fast variations are much greater [160, 161]. Nevertheless, recent work has demonstrated time modulation at optical frequencies [162]. Undoubtedly, implementing these structures in the optical regime holds significant importance for advancing the field.

REFERENCES

[1] R.-S. Chu and T. Tamir, "Wave propagation and dispersion in space-time periodic media," *Proc. IEEE*, vol. 119, no. 7, pp. 797–806, 1972.

[2] Y. Mazor and A. Alù, "One-way hyperbolic metasurfaces based on synthetic motion," *IEEE Trans. Ant. Propag.*, vol. 68, no. 3, pp. 1739–1747, 2020.

[3] Z.-L. Deck-Léger, N. Chamanara, M. Skorobogatiy, M. Silveirinha, and C. Caloz, "Uniform-velocity spacetime crystals," *Adv. Photonics*, vol. 1, no. 5, pp. 056 002:1–26, 2019.

[4] J. Bradley, "IV. A letter from the Reverend Mr. James Bradley Savilian Professor of Astronomy at Oxford, and FRS to Dr. Edmond Halley Astronom. Reg. &c. giving an account of a new discovered motion of the fix'd stars," *Philos. Trans. Royal Soc.*, vol. 35, no. 406, pp. 637–661, 1729.

[5] A. J. Fresnel, "Sur l'influence du mouvement terrestre dans quelques phénomènes d'optique: Lettre de M. Fresnel à M. Arago," *Ann. Chim. Phys.*, vol. 9, pp. 57–66, 1818.

[6] H. Fizeau, "Sur les hypothèses relatives à l'éther lumineux, et sur une expérience qui parait démontrer que le mouvement des corps change la vitesse avec laquelle la lumière se propage dans leur intérieur," *C.R. Acad. Sci.*, vol. 33, pp. 349–355, 1851.

[7] A. Eden, *The search for Christian Doppler*. Springer-Verlag, 1992, contains a facsimilie with an English translation of Doppler's 1842 treatise "Über das farbige Licht der Doppelsterne und einiger anderer Gestirne des Himmels".

[8] C. Doppler, *Über das farbige Licht der Doppelsterne und einiger anderer Gestirne des Himmels*. Calve, 1842.

[9] A. Einstein, "Zur elektrodynamik bewegter Körper," *Ann. Physik*, vol. 322, no. 10, pp. 891–921, 1905, english translation in [10].

[10] H. A. Lorentz, A. Einstein, H. Minkowski, H. Weyl, and A. Sommerfeld, *The principle of relativity: a collection of original memoirs on the special and general theory of relativity*. Dover Publications, 1952.

[11] H. Minkowski, “Die Grundgleichungen für die elektromagnetischen Vorgänge in bewegten Körpern,” *Nachr. Ges. Wiss. Goettingen, Math.-Phys. Kl.*, pp. 53–111, 1908, english translation in [12].

[12] ——, *Space and Time: Minkowski's Papers on Relativity.* Minkowski Institute Press, 2012, translated by F. Lewertoff and V. Petkov.

[13] Lorentz, “Electromagnetic phenomena in a system moving with any velocity smaller than that of light,” *Proc. K. Ned. Akad. Wet.*, vol. 6, pp. 809–831, 1904.

[14] P. Zeeman, “Fresnel's coefficient for light of different colours (second part),” *Proc. R. Acad. Amsterdam*, vol. 17, no. 445, pp. 743–744, 1915.

[15] C. Yeh, “Reflection and transmission of electromagnetic waves by a moving dielectric medium,” *J. Appl. Phys.*, vol. 36, no. 11, pp. 3513–3517, 1965.

[16] ——, “Reflection and transmission of electromagnetic waves by a moving dielectric slab,” *Phys. Rev.*, vol. 144.

[17] D. Censor, “Scattering of a plane wave at a plane interface separating two moving media,” *Radio Sci.*, vol. 4, no. 11, pp. 1079–1088, 1969.

[18] H. Wang and X. Zhang, “Goos-Hänchen and Imbert-Fedorov shifts of an electromagnetic wave packet by a moving object,” *J. Opt. Soc. Am. B*, vol. 29, no. 6, pp. 1218–1225, 2012.

[19] T. M. Grzegorczyk and J. A. Kong, “Electrodynamics of moving media inducing positive and negative refraction,” *Phys. Rev. B*, vol. 74, pp. 033 102:1–4, 2006.

[20] A. Safari, I. De Leon, M. Mirhosseini, O. S. Magaña-Loaiza, and R. W. Boyd, “Light-drag enhancement by a highly dispersive rubidium vapor,” *Phys. Rev. Lett*, vol. 116, p. 013601, 2016.

[21] P.-C. Kuan, C. Huang, W. S. Chan, S. Kosen, and S.-Y. Lan, “Large Fizeau's light-dragging effect in a moving electromagnetically induced transparent medium,” *Nat. Comm.*, vol. 7, pp. 13 030:1–6, 2016.

[22] J. van Bladel, “Electromagnetic fields in the presence of rotating bodies,” *Proc. IEEE*, vol. 64, no. 3, pp. 301–318, 1976.

[23] ——, *Relativity and Engineering.* Springer Science, 1984.

[24] U. Leonhardt and P. Piwnicki, “Optics of nonuniformly moving media,” *Phys. Rev. A*, vol. 60, no. 6, pp. 4301–4312, 1999.

[25] F. R. Morgenthaler, “Velocity modulation of electromagnetic waves,” *IEEE Trans. Microw. Theory Techn.*, vol. 6, no. 2, pp. 167–172, 1958.

[26] V. Bacot, M. Labousse, A. Eddi, M. Fink, and E. Fort, “Time reversal and holography with spacetime transformations,” *Nat. Phys*, vol. 12, no. 10, pp. 972–977, 2016.

[27] A. B. Shvartsburg, “Optics of nonstationary media,” *Phys.-Uspekhi*, vol. 48, no. 8, pp. 797–823, 2005.

[28] O. Silbiger and Y. Hadad, “Optimization-free approach for analog filter design through spatial and temporal soft switching of the dielectric constant,” *Phys. Rev. Appl.*, vol. 19, no. 1, pp. 014 049:1–6, 2022.

[29] A. Shapere and F. Wilczek, “Classical time crystals,” *Phys. Rev. Lett.*, vol. 109, no. 16, pp. 160 402:1–4, 2012.

[30] J. A. Richards, *Analysis of periodically time-varying systems.* Springer, 1983.

[31] J. R. Zurita-Sánchez, P. Halevi, and J. C. Cervantes-González, “Reflection and transmission of a wave incident on a slab with a time-periodic dielectric function $\epsilon(t)$,” *Phys. Rev. A*, vol. 79, pp. 053 821:1–13, 2009.

[32] T. Koutserimpas and R. Fleury, “Electromagnetic waves in a time periodic medium with step-varying refractive index,” *IEEE Trans. Antennas. Propag.*, vol. 66, no. 10, pp. 5300–5307, 2018.

[33] A. Yariv and P. Yeh, *Optical Waves in Crystals.* John Wiley & Sons, 1984.

[34] L. Ostrovskiĭ and B. Solomin, “Correct formulation of the problem of wave interaction with a moving parameter jump,” *Radiophys. Quantum Electron.*, vol. 10, no. 8, pp. 666–668, 1967.

[35] V. I. Semenova, “Reflection of electromagnetic waves from an ionization front,” *Radiophys. Quantum Electron.*, vol. 10, no. 8, pp. 1077–1086, 1967.

[36] M. Lampe, E. Ott, and J. H. Walker, “Interaction of electromagnetic waves with a moving ionization front,” *Phys. Fluids*, vol. 21, no. 1, pp. 42–54, 1978.

[37] E. S. Cassedy and A. A. Oliner, “Dispersion relations in time-space periodic media: Part I-Stable interactions,” *Proc. IEEE*, vol. 51, no. 10, pp. 1342–1359, 1963.

[38] Z. Yu and S. Fan, "Complete optical isolation created by indirect interband photonic transitions," *Nat. Photon.*, vol. 3, no. 2, pp. 91–94, 2009.

[39] N. Chamanara, S. Taravati, Z.-L. Deck-Léger, and C. Caloz, "Optical isolation based on space-time engineered asymmetric photonic band gaps," *Phys. Rev. B*, vol. 96, no. 15, pp. 155 409:1–12, Oct. 2017.

[40] P. A. Huidobro, E. Galiffi, S. Guenneau, R. V. Craster, and J. B. Pendry, "Fresnel drag in space-time modulated metamaterials," *PNAS*, vol. 116, no. 50, pp. 24 943–24 948, 2019.

[41] N. Chamanara and C. Caloz, "Linear pulse compansion using co-propagating space-time modulation," *arXiv:1810.04129*, 2018.

[42] E. Galiffi, M. G. Silveirinha, P. A. Huidobro, and J. B. Pendry, "Photon localization and Bloch symmetry breaking in luminal gratings," *Phys. Rev. B*, vol. 104, pp. 014 302:1–6, 2021.

[43] L. A. Ostrovskiĭ, "Some "moving boundaries paradoxes" in electrodynamics," *Sov. Phys. Usp.*, vol. 18, no. 6, pp. 452–458, 1975.

[44] P. K. Tien, "Parametric amplification and frequency mixing in propagating circuits," *J. Appl. Phys.*, vol. 29, no. 9, pp. 1347–1357, 1958.

[45] A. Cullen, "A travelling-wave parametric amplifier," *Nature*, vol. 181, no. 4605, pp. 332–332, 1958.

[46] E. S. Cassedy, "Dispersion relations in time-space periodic media: Part II-Unstable interactions," *Proc. IEEE*, vol. 55, no. 7, pp. 1154–1168, 1967.

[47] Z.-L. Deck-Léger, A. Akbarzadeh, and C. Caloz, "Wave deflection and shifted refocusing in a medium modulated by a superluminal rectangular pulse," *Phys. Rev. B*, vol. 97, pp. 104 305:1–7, 2018.

[48] Y. A. Kravtsov, L. A. Ostrovsky, and N. S. Stepanov, "Geometrical optics of inhomogeneous and nonstationary dispersive media," *Proc. IEEE*, vol. 62, no. 11, pp. 1492–1510, 1974.

[49] B. W. Plansinis, W. R. Donaldson, and G. P. Agrawal, "Spectral splitting of optical pulses inside a dispersive medium at a temporal boundary," *IEE J. Quantum Electron.*, vol. 52, no. 1, pp. 6 100 708:1–8, 2016.

[50] M. A. Gaafar, T. Baba, M. Eich, and A. Y. Petrov, "Front-induced transitions," *Nat. Photonics*, vol. 13, no. 11, pp. 737–748, 2019.

[51] K. Lurie and S. Weekes, "Wave propagation and energy exchange in a spatio-temporal material composite with rectangular microstructure," *J. Math. Anal. Appl.*, vol. 314, no. 1, pp. 286–310, 2006.

[52] O. Mattei and G. Milton, "Field patterns: A new type of wave with infinitely degenerate band structure," *EPL*, vol. 120, no. 5, pp. 54 003:1–6, 2018.

[53] N. L. Balazs, "On the solution of the wave equation with moving boundaries," *J. Math. Anal. Appl.*, vol. 3, pp. 472–484, 1961.

[54] A. Bahrami, Z.-L. Deck-Léger, and C. Caloz, "Electrodynamics of metamaterials formed by accelerated modulation," *arXiv:2208.11506 [physics.optics]*, 2022.

[55] T. Koutserimpas and C. Valagiannopoulos, "Electromagnetic fields between moving mirrors: singular waveforms inside doppler cavities," *Opt. Express*, vol. 31, no. 3, pp. 5087–5101, 2023.

[56] J. A. Kong, "Theorems of bianisotropic media," *Proc. IEEE*, vol. 60, pp. 1036–i1046, 1972.

[57] C. Yeh, "Reflection and transmission of electromagnetic waves by a moving dielectric medium," *J. Appl. Phys.*, vol. 36, no. 11, pp. 3513–3517, 1965.

[58] C. S. Tsai and B. A. Auld, "Wave interactions with moving boundaries," *J. Appl. Phys.*, vol. 38, no. 5, pp. 2106–2115, 1967.

[59] B. M. Bolotovskii and S. N. Stolyarov, "Reflection of light from a moving mirror and related problems," *Sov. Phys. Usp.*, vol. 32, no. 9, pp. 813–827, 1989.

[60] J. Vehmas, S. Hrabar, and S. Tretyakov, "Transmission lines emulating moving media," *New J. Phys*, vol. 16, pp. 093 065:1–20, 2014.

[61] P. A. Cherenkov, "Visible emission of clean liquids by action of γ radiation," *Dokl. Akad. Nauk SSSR*, vol. 2, no. 451, 1934.

[62] I. E. Tamm and I. M. Frank, "Coherent radiation of fast electrons in a medium," *Dokl. Akad. Nauk SSSR*, vol. 14, no. 107, 1937.

[63] H. A. Lorentz, *Versuch einer Theorie der elektrischen und optischen Erscheinungen von bewegten Körpern.* Springer, Dordrecht, 1937.

[64] J. A. Kong, *Electromagnetic Wave Theory*, 7th ed. EMW Publishing, 2008.

[65] C. Caloz, A. Alù, S. Tretyakov, D. Sounas, K. Achouri, and Z.-L. Deck-Léger, "Electromagnetic nonreciprocity," *Phys. Rev. Appl.*, vol. 10, no. 4, pp. 047 001:1–26, 2018.

[66] C. Caloz and A. Sihvola, "Electromagnetic chirality, Part I: The microscopic perspective," *IEEE Antennas Propag. Mag.*, vol. 62, pp. 58 – 71, 2020.

[67] ——, "Electromagnetic chirality, Part 2: The macroscopic perspective," *IEEE Antennas Propag. Mag.*, vol. 62, pp. 82–98, 2020.

[68] B. M. Bolotovskii and S. N. Stolyarov, "Current status of the electrodynamics of moving media (infinite media)," *Sov. Phys. Usp.*, vol. 17, no. 6, pp. 875–895, 1975.

[69] W. Pauli, *Theory of Relativity.* Pergamon Press, 1958, sec. 37, p. 114.

[70] Y. Ra'di, V. Asadchy, and S. A. Tretyakov, "Nihility in non-reciprocal bianisotropic media," *EPJ appl. Metamat*, vol. 2, no. 6, pp. 1–4, 2015, see eq.10, which provides the transverse impedance of uniaxial nonreciprocal media.

[71] S. A. Tretyakov and A. A. Sochava, "Reflection and transmission of plane electromagnetic waves in uniaxial bianisotropic materials," *Int. J. Infrared Millim. Waves*, vol. 15, no. 5, pp. 829–856, 1994.

[72] L. B. Felsen and N. Marcuvitz, *Radiation and Scattering of Waves.* Wiley, 2003.

[73] T. A. Morgado and M. G. Silveirinha, "Drift-induced unidirectional graphene plasmons," *ACS Photonics*, vol. 5, pp. 4253–4258, 2018.

[74] D. Correas-Serrano and J. S. Gomez-Diaz, "Nonreciprocal and collimated surface plasmons in drift-biased graphene metasurfaces," *Phys. Rev. B*, vol. 100, pp. 081 410–1:6, 2019.

[75] N. Ashcroft and N. Mermin, *Introduction to Solid State Physics.* Saunders, Philadelphia, 1976.

[76] J. D. Joannopoulos, S. G. Johnson, J. N. Winn, and R. D. Meade, *Photonic crystals: Molding the flow of light.* Princeton University Press, 2011.

[77] B. E. A. Saleh and M. C. Teich, *Fundamentals of Photonics.* Wiley, 2007, Chap. 7.

[78] W. H. Bragg and W. L. Bragg, "The reflection of X-rays by crystals," *Proc. R. Soc. Lond. A.*, vol. 88, no. 605, pp. 428–438, 1913.

[79] D. Holberg and K. Kunz, “Parametric properties of fields in a slab of time-varying permittivity,” *IEEE Trans. Antennas. Propag.*, vol. 14, no. 2, pp. 183–194, 1966.

[80] R. Fante, “Transmission of electromagnetic waves into time-varying media,” *IEEE Trans. Antennas. Propag.*, vol. 19, no. 3, pp. 417–424, 1971.

[81] A. Kamal, “A parametric device as a nonreciprocal element,” *Proc. IRE*, vol. 48, no. 8, pp. 1424–1430, 1960.

[82] L. Baldwin, “Nonreciprocal parametric amplifier circuits,” *Proc. IRE*, vol. 49, no. 6, pp. 1075–1075, 1961.

[83] J. Vila, R. K. Pal, M. Ruzzene, and G. Trainiti, “A Bloch-based procedure for dispersion analysis of lattices with periodic time-varying properties,” *J. Sound Vib.*, vol. 406, pp. 363–377, 2017.

[84] E. Lustig, Y. Sharabi, and M. Segev, “Topological aspects of photonic time crystals,” *Optica*, vol. 5, no. 11, pp. 1390–1395, 2018.

[85] K. Giergiel, A. Dauphin, M. Lewenstein, J. Zakrzewski, and K. Sacha, “Topological time crystals,” *New J. Phys.*, vol. 21, no. 11, pp. 052 003:1–11, 2018.

[86] D. K. Kalluri, *Electromagnetics of Time Varying Complex Media: Frequency and Polarization Transformer.* CRC Press, 2010.

[87] A. Shlivinski and Y. Hadad, “Beyond the Bode-Fano bound: Wideband impedance matching for short pulses using temporal switching of transmission-line parameters,” *Phys. Rev. Lett.*, vol. 121, no. 20, pp. 204 301:1–6, 2018.

[88] M. Mirmoosa, G. Ptitcyn, V. Asadchy, and S. Tretyakov, “Time-varying reactive elements for extreme accumulation of electromagnetic energy,” *Phys. Rev. Appl.*, vol. 11, no. 1, pp. 014 024:1–10, 2019.

[89] M. Skorobogatiy and J. D. Joannopoulos, “Rigid vibrations of a photonic crystal and induced interband transitions,” *Phys. Rev. B*, vol. 61, no. 8, p. 5293, 2000.

[90] ——, “Photon modes in photonic crystals undergoing rigid vibrations and rotations,” *Phys. Rev. B*, vol. 61, no. 23, p. 15554, 2000.

[91] H. Qu, Z.-L. Deck-Léger, C. Caloz, and M. Skorobogatiy, “Frequency generation in moving photonic crystals,” *J. Opt. Soc. Am. B*, vol. 33, no. 8, pp. 1616–1626, 2016.

[92] D.-W. Wang, H.-T. Zhou, M.-J. Guo, J.-X. Zhang, J. Evers, and S.-Y. Zhu, "Optical diode made from a moving photonic crystal," *Phys. Rev. Lett.*, vol. 110, no. 9, p. 093901, 2013.

[93] J. Ramasastry, "Wave interaction with moving boundaries," *Electron. Lett*, vol. 11, no. 3, pp. 479–481, 1967.

[94] C. Tsai and B. Auld, "Wave interactions with moving boundaries," *J. Appl. Phys.*, vol. 38, no. 5, pp. 2106–2115, 1967.

[95] A. M. Shaltout, V. M. Shalaev, and M. L. Brongersma, "Spatiotemporal light control with active metasurfaces," *Science*, vol. 364, no. 6441, pp. 1–10, 2019.

[96] C. Caloz and Z.-L. Deck-Léger, "Spacetime metamaterials, part I: General concepts," *IEEE Trans. Antennas Propag.*, vol. 68, no. 3, pp. 1569–1582, 2020, part I: General concepts.

[97] ——, "Spacetime metamaterials, part II: Theory and applications," *IEEE Trans. Antennas Propag.*, vol. 68, no. 3, pp. 1583–1598, 2020, part II: Theory and Applications.

[98] K. Lurie, D. Onofrei, and S. Weekes, "Mathematical analysis of the waves propagation through a rectangular material structure in space–time," *J. Math. Anal. Appl.*, vol. 355, no. 1, pp. 180–194, 2009.

[99] G. Milton and O. Mattei, "Field patterns: A new mathematical object," *Proc. R. Soc. A*, vol. 473, no. 2198, pp. 20 160 819:1–26, 2017.

[100] O. Mattei and G. Milton, "Field patterns without blow up," *New J. Phys.*, vol. 19, no. 9, pp. 093 022:1–16, 2017.

[101] J. R. Pierce, "Use of the principles of conservation of energy and momentum in connection with the operation of wave-type parametric amplifiers," *J. Appl. Phys.*, vol. 30, no. 9, pp. 1341–1346, 1959.

[102] A. Bahabad, M. M. Murnane, and H. C. Kapteyn, "Quasi-phase-matching of momentum and energy in nonlinear optical processes," *Nat. Photonics*, vol. 4, no. 8, p. 570, 2010.

[103] S. Taravati, N. Chamanara, and C. Caloz, "Nonreciprocal electromagnetic scattering from a periodically space-time modulated slab and application to a quasisonic isolator," *Phys. Rev. B*, vol. 96, no. 16, pp. 165 144:1–11, 2017.

[104] N. Chamanara, S. Taravati, Z.-L. Deck-Léger, and C. Caloz, "Optical isolation based on space-time engineered asymmetric photonic band gaps," *Phys. Rev. B*, vol. 96, no. 15, pp. 155 409:1–12, 2017.

[105] C. Caloz and A. Alù, "Guest editorial special cluster on magnetless nonreciprocity in electromagnetics," *IEEE Antennas Wirel. Propag. Lett.*, vol. 17, no. 11, pp. 1931–1937, 2018.

[106] F. Biancalana, A. Amann, A. V. Uskov, and E. P. O'Reilly, "Dynamics of light propagation in spatiotemporal dielectric structures," *Phys. Rev. E*, vol. 75, no. 4, pp. 046 607:1–12, 2007.

[107] L. Felsen and G. M. Whitman, "Wave propagation in time-varying media," *IEEE Trans. Antennas. Propag.*, vol. 18, no. 2, pp. 242–253, 1970.

[108] J. D. Jackson, *Classical electrodynamics.* Wiley, 1999.

[109] L.-Q. Shui, Z.-F. Yue, Y.-S. Liu, Q.-C. Liu, and J.-J. Guo, "One-dimensional linear elastic waves at moving property interface," *Wave Motion*, vol. 51, no. 7, pp. 1179–1192, 2014.

[110] Z.-L. Deck-Léger and C. Caloz, "Scattering at interluminal interface," in *2019 IEEE AP-S Int. Antennas Propag.* IEEE, 2018, pp. 165–166.

[111] H. Lorentz, "Electromagnetic phenomena in a system moving with any velocity smaller than that of light," in *Collected Papers.* Springer, 1937, pp. 172–197.

[112] W. Pauli, *Theory of Relativity.* Courier Corporation, 1981.

[113] A. Einstein, "Zur elektrodynamik bewegter Körper," *Ann. Physik*, vol. 322, no. 10, pp. 891–921, 1905, reprinted in [10].

[114] M. Laue, "Die Mitführung des Lichtes durch bewegte Köper nach dem Relativitätsprinzip," *Ann. d. Phys*, vol. 29, no. 7, pp. 077 405:1–4, 1907.

[115] J. A. Kong, *Electromagnetic Wave Theory*, 7th ed. EMW Publication, 2008.

[116] G. Stokes, *On the perfect Blackness of the Central Spot in Newton's Rings, and on the Verification of Fresnel's Formula for the intensities of Reflected and Reflacted Rays*, ser. Cambridge Library Collection - Mathematics. Cambridge University Press, 2009, vol. 2, p. 89–103.

[117] M. Born and E. Wolf, *Principles of optics.* Pergamon, 1980.

[118] D. R. Smith and D. Schurig, "Electromagnetic wave propagation in media with indefinite permittivity and permeability tensors," *Phys. Rev. Lett.*, vol. 90, no. 7, pp. 077 405:1–4, 2003.

[119] S. Seshadri, "Asymptotic theory of mode coupling in a space-time periodic medium-Part I: Stable interactions," *Proc. IEEE*, vol. 65, no. 7, pp. 996–1004, 1977.

[120] S. Elnaggar and G. Milford, "Controlling nonreciprocity using enhanced Brillouin scattering," *IEEE Trans. Ant. Prop.*, vol. 66, no. 7, pp. 3500–3511, 2018.

[121] S. Seshadri, "Asymptotic theory of mode coupling in a space-time periodic medium-Part II: Unstable interactions," *Proc. IEEE*, vol. 65, no. 10, pp. 1459–1469, 1977.

[122] F. Abelès, "La théorie générale des couches minces," *J. Ph. Radium*, vol. 11, no. 7, pp. 307–309, 1950.

[123] S. Longhi, "$\mathcal{PT}$-symmetric laser absorber," *Phys. Rev. A*, vol. 82, pp. 031 801:1–4, 2010.

[124] M. Skorobogatiy and J. Yang, *Fundamentals of photonic crystal guiding.* Cambridge University Press, 2009.

[125] N. Ashcroft and D. Mermin, *Solid State Physics.* Hartcourt College Publishers, 1976.

[126] C. Caloz, Z.-L. Deck-Léger, A. Bahrami, O. C. Vincente, and Z. Li, "Generalized space-time engineered modulation (GSTEM) metamaterials: A global and extended perspective." *IEEE Antennas Propag. Mag.*, 2022.

[127] J. Pendry, E. Galiffi, and P. Huidobro, "Gain in time-dependent media – a new mechanism," *Optica*, vol. 8, no. 5, pp. 636–637, 2021.

[128] J. Park and B. Min, "Spatiotemporal plane wave expansion method for arbitrary space–time periodic photonic media," *Opt. Lett.*, vol. 46, pp. 484–487, 2021.

[129] W. C. Röntgen, "Ueber die durch Bewegung eines im homogenen electrischen Felde befindlichen Dielectricums hervorgerufene electrodynamische Kraft," *Annalen der Physik*, vol. 271, no. 10, pp. 264–270, 1888, explained in [163].

[130] D. Cheng and J. A. Kong, "Time-harmonic fields in source-free bianisotropic media," *J. Appl. Phys*, vol. 39, no. 12, pp. 5792–5796, 1968.

[131] E. Galiffi, R. Tirole, S. Yin, H. Li, S. Vezzoli, P. A. Huidobro, M. G. Silveirinha, R. Sapienza, A. Alù, and J. B. Pendry, "Photonics of time-varying media," *Adv. Photon.*, vol. 4, no. 1, p. 014002, 2022.

[132] K. S. Kunz, "Plane electromagnetic waves in moving media and reflections from moving interfaces," *J. Appl. Phys.*, vol. 51, no. 2, pp. 873–884, 1980.

[133] F. Bloch, "Über die quantenmechanik der elektronen in kristallgittern," *Zeitschrift für physik*, vol. 52, no. 7-8, pp. 555–600, 1929.

[134] G. Floquet, "Sur les équations différentielles linéaires," *Ann. Sci. Éc. Norm. Supér.*, vol. 12, no. 1883, pp. 47–88, 1883.

[135] J. W. Strutt, "On the constant of magnetic rotation of light in bisulphide of carbon," *Phil. Trans. R. Soc.*, vol. 176, p. 343–366, 1885.

[136] H. Minkowski, "Die grundgleichungen für die elektromagnetischen vorgänge in bewegten körpern," *Nachrichten von der Gesellschaft der Wissenschaften zu Göttingen, Mathematisch-Physikalische Klasse*, vol. 1908, pp. 53–111, 1908.

[137] N. Chamanara, Y. Vahabzadeh, and C. Caloz, "Simultaneous control of the spatial and temporal spectra of light with space-time varying metasurfaces," *IEEE Trans. Antennas Propag.*, vol. 67, no. 4, pp. 2430–2441, Apr. 2019.

[138] Y. Sharabi, A. Dikopoltsev, E. Lustig, Y. Lumer, and M. Segev, "Spatiotemporal photonic crystals," *Optica*, vol. 9, no. 6, pp. 585–592, 2022.

[139] F. Harfoush, A. Taflove, and G. A. Kriegsmann, "Numerical implementation of relativistic electromagnetic boundary conditions in a laboratory-frame grid," *J. Comput. Phys.*, vol. 89, no. 1, pp. 80–94, 1990.

[140] ——, "A numerical technique for analyzing electromagnetic wave scattering from moving surfaces in one and two dimensions," *IEEE Trans. Ant. Propag.*, vol. 37, no. 1, pp. 55–63, 1989.

[141] H. Iwamatsu and M. Kuroda, "Over set grid generation method coupled with FDTD method while considering the Doppler effect," *IEEJ Trans. Fundam. Mater.*, vol. 129, no. 10, pp. 699–703, 2009.

[142] K. Zheng, Z. Mu, H. Luo, and G. Wei, "Electromagnetic properties from moving dielectric in high speed with Lorentz-FDTD," *IEEE Ant. Propag. Lett.*, vol. 15, pp. 934–937, 2016.

[143] Y. Zhao and S. Chaimool, "Relativistic finite-difference time-domain analysis of high-speed moving metamaterials," *Sci. Rep.*, vol. 8, pp. 7686:1–12, 2018.

[144] W. F. Ames, *Numerical Methods for Partial Differential Equations.* Academic Press, 1977.

[145] A. Taflove and S. C. Hagness, *Computational Electrodynamics: The Finite-Domain Time-Domain Method*, 2nd ed. Artech House, 2000.

[146] P. A. Huidobro, E. Galiffi, S. Guenneau, R. V. Craster, and J. B. Pendry, "Fresnel drag in space-time modulated metamaterials," *PNAS*, vol. 116, no. 50, pp. 24 943–24 948, 2019.

[147] Z. Li, X. Ma, A. Bahrami, Z.-L. Deck-Léger, and C. Caloz, "Generalized total internal reflection at dynamic interfaces," *Phys. Rev. B*, vol. 107, no. 11, pp. 115 129:1–8, 2016.

[148] K. Yee, "Numerical solution of initial boundary value problems involving Maxwell's equations in isotropic media," *IEEE Trans. Antennas Propag.*, vol. 14, no. 3, pp. 302–307, 1966.

[149] T. Shiozawa and K. Hazama, "General solution to the problem of reflection and transmission by a moving dielectric medium," *Radio Sci.*, vol. 3, no. 6, pp. 569–575, 1968.

[150] D. Censor, "Scattering of a plane wave at a plane interface separating two moving media," *Radio Sci.*, vol. 4, no. 11, pp. 1079–1088, 1969.

[151] J.-P. Berenger, "A perfectly matched layer for the absorption of electromagnetic waves," *J. Comput. Phys.*, vol. 114, pp. 185–200, 1993.

[152] J. von Neumann and R. D. Richtmyer, "A method for the numerical calculation of hydrodynamic shocks," *J. Appl. Phys.*, vol. 21, no. 3, pp. 232–237, 1950.

[153] P. Sturrock, "Kinematics of growing waves," *Phys. Rev.*, vol. 112, no. 5, pp. 1488–1503, 1958.

[154] N. Chamanara, Z.-L. Deck-Léger, C. Caloz, and D. Kalluri, "Unusual electromagnetic modes in space-time modulated dispersion-engineered media," *Phys. Rev. A*, vol. 97, no. 6, pp. 063 829:1–9, 2018.

[155] J. A. Kong, "Charged particles in bianisotropic media," *Radio Sci.*, vol. 6, no. 11, pp. 1015–1019, 1971.

[156] M. G. Silveirinha, "Optical instabilities adn spontaneous light emission by polarizable moving matter," *Phys. Rev. X*, vol. 4, no. 3, pp. 031 013:1–14, 2014.

[157] J. Ran, Y. Zhang, X. Chen, K. Fang, J. Zhao, Y. Sun, and H. Chen, "Realizing tunable inverse and normal Doppler shifts in reconfigurable RF metamaterials," *Sci. Rep.*, vol. 5, no. 1, pp. 11 659:1–8, 2015.

[158] S. Taravati and C. Caloz, "Mixer-duplexer-antenna leaky-wave system based on periodic space-time modulation," *IEEE Trans. Antennas Propag.*, vol. 65, no. 2, pp. 442–452, 2017.

[159] W. Rhodes, "Acousto-optic signal processing: Convolution and correlation," *Proc. IEEE*, vol. 69, no. 1, pp. 65–79, 1981.

[160] J. B. Khurgin, "Energy and power requirements for alteration of the refractive index," *arXiv:2308.16011[physics]*, 2003.

[161] Z. Hayran, J. B. Khurgin, and F. Monticone, "$\hbar\omega$ versus $\hbar\underline{\mathrm{k}}$: dispersion and energy constraints on time-varying photonic materials and time crystals," *Opt. Mat.*, vol. 12, no. 10, pp. 3904–3917, 2022.

[162] E. Lustig, O. Segla, S. Saha, E. Bordo, S. N. Chowdhury, Y. Sharabi, A. Fleisher, A. Boltasserva, O. Cohen, V. M. Shalaev, and M. Segev, "Time-refraction optics with single cycle modulation," *Nanophotonics*, vol. 10, no. 8, pp. 1077–1086, 2023.

[163] A. Sommerfeld, *Optics-Lectures on Theoretical Physics, Vol. 4.* Academic Press, New York, 1957, Sec.7.

[164] H. Gruenberg and P. Daly, "Waveguides containing moving dispersive media," *IEEE Trans. Antennas Propag.*, vol. MTT-15, no. 11, pp. 743–744, 1967.

[165] H. Berger and J. W. E. Griemsmann, "Guided waves in moving dispersive media, Part II: Relativistic velocities," *IEEE Trans. Antennas Propag.*, vol. MTT-16, no. 1, pp. 16–20, 1968.

[166] P. K. Jain, D. Singh, P. N. Gupta, and S. K. Tolpadi, "Dispersion relations for parallel-plane waveguide containing transversely magnetized uniaxial and warm plasma in relative motion," *IEEE Trans. Antennas Propag.*, vol. 21, pp. 743–744, 1973.

[167] U. Leonhardt and P. Piwnicki, "Relativistic effects of light in moving media with extremely low group velocity," *Phys. Rev. Lett.*, vol. 84, no. 5, pp. 822–825, 2000.

APPENDIX A APPENDIX FOR CHAPTER 3

A.1 Bianisotropy, Wave Impedance and Wave Velocity in the Moving Frame

We derive here the constitutive relations for homogeneous isotropic media as seen in a moving frame. Figure A.1 represents a modulated spacetime interface, from the viewpoint of the laboratory frame in Fig. A.1(a) and from the viewpoint of the moving frame in Fig. A.1(b). In Fig. A.1(a), the interface of the spacetime modulation moves to the right but its constitutive particles have vertical trajectories, i.e. appear stationary. In Fig. A.1(b), the interface appears stationary, but the particles appear in motion, moving to the left.

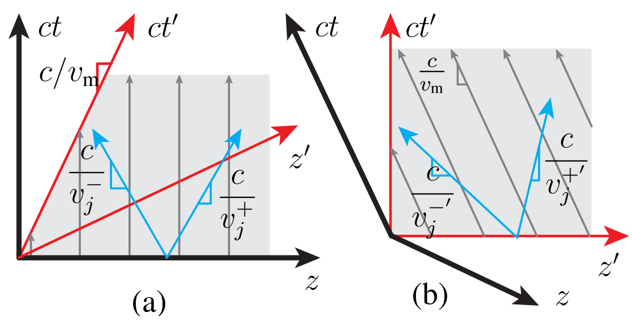

Figure A.1 Spacetime interface represented in two inertial frames. The arrows represent the trajectories of the media particles. In both (a) and (b), the interfaces of the spacetime variation are parallel to the ct' axis and the media trajectories are parallel to the ct axis. (a) Laboratory frame viewpoint. Media appears at rest. wave velocity is independent of direction: $v_j^+ = v_j^-$ (b) Moving frame viewpoint. Media appears to be moving in $-z$ direction. Wave velocities are direction dependent: $v_j^+ \neq v_j^-$, with $|v_j^-| > |v_j^+|$.

We first write the constitutive relations of the bulk stationary medium in the laboratory frame

$$D_{xj} = \epsilon_j E_{xj}, \tag{A.1a}$$

$$B_{yj} = \mu_j H_{yj}. \tag{A.1b}$$

Applying the Lorentz transformations (3.13) to these relations yields

$$D'_{xj} - \frac{v_\mathrm{f}}{c^2} H'_{yj} = \epsilon_j \left(E'_{xj} - v_\mathrm{f} B'_{yj} \right) \tag{A.2a}$$

and

$$B'_{yj} - \frac{v_\mathrm{f}}{c^2} E'_{xj} = \mu_j \left(H'_{yj} - v_\mathrm{f} D'_{xj} \right). \tag{A.2b}$$

Solving (A.2a) and (A.2b) for D'_y and B'_x, we obtain the constitutive relations

$$\begin{aligned} D'_{xj} &= \epsilon_j \frac{1 - v_\mathrm{f}^2/c^2}{1 - v_\mathrm{f}^2/v_j^2} E'_{xj} + \frac{v_\mathrm{f}}{c^2} \frac{1 - c^2/v_j^2}{1 - v_\mathrm{f}^2/v_j^2} H'_{yj} \\ &= \epsilon'_j E'_{xj} + \chi'_j H'_{yj}, \end{aligned} \tag{A.3a}$$

and

$$\begin{aligned} B'_{yj} &= \mu_j \frac{1 - v_\mathrm{f}^2/c^2}{1 - v_\mathrm{f}^2/v_j^2} H'_{yj} + \frac{v_\mathrm{f}}{c^2} \frac{1 - c^2/v_j^2}{1 - v_\mathrm{f}^2/v_j^2} E'_{xj} \\ &= \mu'_j H'_{yj} + \chi'_j E'_{xj}. \end{aligned} \tag{A.3b}$$

where v_j is the velocity of light in the medium in the laboratory frame, $v_j = 1/\sqrt{\epsilon_j \mu_j}$. These equations reveal that the medium is biisotropic in the moving frame, since the magneto-electric coupling terms are scalar, and, more specifically, a Tellegen medium, since the there is a unique variable χ_j for both the electro-magnetic and the magneto-electric coupling terms. More generally, moving volumes appear bianisotropic in the moving frame. Indeed, the media does not transform the same way in the directions parallel and perpendicular to the motion of the medium.

We next calculate the wave impedance and the wave velocity of moving isotropic media. We first write the Maxwell curl equations for a plane monochromatic wave,

$$\omega'_j D'_{xj} = k'_j H'_{yj}, \qquad \omega'_j B'_{yj} = k'_j E'_{xj}. \tag{A.4}$$

Dividing the left equation of (A.4) by the right equation of (A.4), we find

$$\frac{D'_{xj}}{H'_{yj}} = \frac{B'_{yj}}{E'_{xj}}. \tag{A.5}$$

Inserting the constitutive relations (A.3b) into (A.5), we find the impedance η'_j, defined as the ratio of the E and H fields:

$$\eta'_j = \frac{E'_{xj}}{H'_{yj}} = \sqrt{\frac{\mu'_j}{\epsilon'_j}} = \sqrt{\frac{\mu_j}{\epsilon_j}} = \eta_j, \tag{A.6}$$

where the third equality comes from the definitions of μ', ϵ' in (A.3a) and (A.3b). We thus conclude from (A.6) that the impedance is invariant under a change of frames.

The wave velocity, defined as $v_j^{\pm'} = \omega_j'/k_j'$, is found from (A.4) as

$$v_j^{\pm'} = \frac{\omega_j'}{k_j'} = \frac{H_{yj}'}{D_{xj}'} = \frac{E_{xj}'}{B_{yj}'}. \tag{A.7}$$

inserting (A.6) and (A.3) into (A.7) yields

$$v_j^{\pm'} = \frac{H_{yj}'}{D_{xj}'} = \frac{1}{\epsilon_j'\eta_j' + \chi_j'} = \frac{v_j^{\pm} + v_\mathrm{f}}{1 + v_j^{\pm} v_\mathrm{f}/c^2}. \tag{A.8}$$

Comparing this result with the addition law of velocities provided in (3.7b), we see a sign difference of v_f, due to the fact that for a positive modulation velocity, $v_\mathrm{m} > 0$, the medium appears to be moving in the $-z'$ direction in the moving frame, as drawn in Fig. A.1(b).

A.2 Alternative Derivation of the Continuity Conditions

We start with one-dimensional Maxwell equations,

$$\frac{\partial E_x}{\partial z} = -\frac{\partial B_y}{\partial t} = -\frac{\partial \mu(z - v_\mathrm{m}t) H_y}{\partial t}, \tag{A.9a}$$

$$\frac{\partial H_y}{\partial z} = -\frac{\partial D_x}{\partial t} = -\frac{\partial \epsilon(z - v_\mathrm{m}t) E_x}{\partial t}, \tag{A.9b}$$

and apply the following coordinate transformation:

$$z' = z - v_\mathrm{m} t, \qquad t' = t. \tag{A.10}$$

This does not correspond to a Lorentz transformation, and therefore does not lead to invariance. The partial derivatives of (A.9) are found as

$$\frac{\partial}{\partial z} = \frac{\partial}{\partial z'}\frac{\partial z'}{\partial z} + \frac{\partial}{\partial t'}\frac{\partial t'}{\partial z} = \frac{\partial}{\partial z'}, \tag{A.11a}$$

$$\frac{\partial}{\partial t} = \frac{\partial}{\partial t'}\frac{\partial t'}{\partial t} + \frac{\partial}{\partial z'}\frac{\partial z'}{\partial t} = \frac{\partial}{\partial t'} - v_\mathrm{m}\frac{\partial}{\partial z'}. \tag{A.11b}$$

Substituting these relations into (A.9) yields

$$\frac{\partial E_x}{\partial z'} = -\left(\frac{\partial}{\partial t'} - v_\mathrm{m}\frac{\partial}{\partial z'}\right)\mu(z')H_y, \tag{A.12a}$$

$$\frac{\partial H_y}{\partial z'} = -\left(\frac{\partial}{\partial t'} - v_{\mathrm{m}}\frac{\partial}{\partial z'}\right)\epsilon(z')E_x. \tag{A.12b}$$

Rearranging (A.12), we find

$$\frac{\partial}{\partial z'}\left(E_x - v_{\mathrm{m}}\mu(z')H_y\right) = -\frac{\partial}{\partial t'}\mu(z')H_y, \tag{A.13a}$$

$$\frac{\partial}{\partial z'}\left(H_y - v_{\mathrm{m}}\epsilon(z')E_x\right) = -\frac{\partial}{\partial t'}\epsilon(z')E_x. \tag{A.13b}$$

Inspecting these equations, we can deduce the continuity conditions by reasoning ad absurbdum: if the arguments of the $\partial z'$ derivative on the left-hand side in (A.13), $E_x + v_{\mathrm{m}}\mu(z')H_y$ or $H_y + v_{\mathrm{m}}\epsilon(z')E_x$, vary as a step function, then the right-hand side would be an impulse function, which is unphysical. Therefore, quantities $E_x + v_{\mathrm{m}}\mu(z')H_y$ and $H_y + v_{\mathrm{m}}\epsilon(z')E_x$, or $E_x + v_{\mathrm{m}}B_y$ and $H_y + v_{\mathrm{m}}D_x$, must be continuous at the interface. We can see that in the limiting case when $v_{\mathrm{m}} = 0$, the quantities E_x, H_y are continuous, as expected. In the limiting case $v_{\mathrm{m}} = \infty$, the quantities D_x, B_y are continuous, as reported in [25].

A.3 Travel Length or Duration across the Unit Cell of the Crystal

Consider Fig. A.2. Each graph involves two triangles, one with slope n_j and the other with slope c/v_{m}.

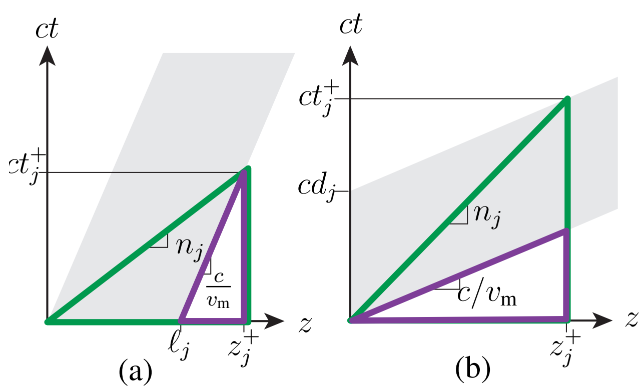

Figure A.2 Graphical derivation of the travel length or duration across the unit cell of the crystal. (a) Subluminal regime (length). (b) Superluminal regime (duration).

In the subluminal case, represented in Fig. A.2(a), we have

$$n_j = \frac{ct_j^+}{z_j^+}, \qquad \frac{c}{v_{\mathrm{m}}} = \frac{ct_j^+}{z_j^+ - \ell_j}. \tag{A.14}$$

Isolating z_j^+ in both relations,

$$z_j^+ = \frac{ct_j^+}{n_j}, \qquad z_j^+ = \ell_j + ct_j^+ \frac{v_\mathrm{m}}{c}, \tag{A.15}$$

and equating these results yields

$$\frac{ct_j^+}{n_j} = \ell_j + ct_j^+ \frac{v_\mathrm{m}}{c}, \qquad t_j^+ = \frac{\ell_j n_j/c}{1 - v_\mathrm{m} n_j/c}. \tag{A.16}$$

Similarly, in superluminal case, represented in Fig. A.2(b), we have

$$n_j = \frac{ct_j^+}{z_j^+}, \qquad \frac{c}{v_\mathrm{m}} = \frac{ct_j^+ - cd_j}{z_j^+}. \tag{A.17}$$

Isolating ct_j^+ in both relations,

$$ct_j^+ = z_j^+ n_j, \qquad ct_j^+ = \frac{c}{v_\mathrm{m}} z_j^+ + cd_j. \tag{A.18}$$

and equating these results yields

$$z_j^+ n_j = \frac{c}{v_\mathrm{m}} z_j^+ + cd_j, \qquad z_j^+ = \frac{cd_j}{n_j - c/v_\mathrm{m}}. \tag{A.19}$$

A.4 Unit-cell Matrix Symmetry

We deduce the properties of the unit-cell transfer matrix,

$$\begin{bmatrix} \psi_\mathrm{out}^+ \\ \psi_\mathrm{out}^- \end{bmatrix} = [M_\mathrm{B}] \begin{bmatrix} \psi_\mathrm{in}^+ \\ \psi_\mathrm{in}^- \end{bmatrix}, \tag{A.20}$$

by applying a spacetime symmetry argument, with the help of Fig. A.3. The initial problem of a spacetime slab is represented in the top left panel of the figure. A time reversal and a space reversal are successively applied to this problem, resulting in the bottom right panel, which retrieves the initial problem. We therefore expect the matrix relating the fields on the left to the fields on the right of the slab to be the same for the space-time reversed problem and for the initial problem. According to the bottom right panel of Fig. A.3,

$$\begin{bmatrix} \psi_\mathrm{in}^{+*} \\ \psi_\mathrm{in}^{-*} \end{bmatrix} = [M_\mathrm{B}] \begin{bmatrix} \psi_\mathrm{out}^{+*} \\ \psi_\mathrm{out}^{-*} \end{bmatrix}. \tag{A.21}$$

Taking the complex conjugate of this relation, and multiplying the resulting equation by the inverse of M_{B}^* reveals the following property:

$$[M_{\mathrm{B}}^*]^{-1} = M_{\mathrm{B}}, \tag{A.22}$$

or, in terms of the matrix elements,

$$\begin{bmatrix} a & b \\ c & d \end{bmatrix} = \frac{1}{\det[M]} \begin{bmatrix} d^* & -b^* \\ -c^* & a^* \end{bmatrix}. \tag{A.23}$$

Since for spacetime slab, $\det[M_{\mathrm{B}}] = \mathrm{e}^{i\Delta\phi}$ (see Sec. 3.5,

$$a\mathrm{e}^{i\Delta\phi} = d^*, \tag{A.24}$$

$$b\mathrm{e}^{i\Delta\phi} = -b^*, \qquad c\mathrm{e}^{i\Delta\phi} = -c^* \tag{A.25}$$

which is consistent with [123] and with (3.79) of Sec. 3.5.

A.5 Frequency Centers for Parallel Truncation

Here, we calculate the incident frequencies and wavenumbers aligned with the bandgaps in the case of a co-moving truncation. Figure A.4 provides the graphical construction, with the dispersion of the incident medium of refractive index n_0 and the dispersion diagram of the spacetime crystals.

We start with the subluminal case. We first deduce $\omega_{\mathrm{e_g}}$, which is found from Fig. A.4(a) to satisfy

$$\omega_{\mathrm{e_g}} = \omega_{0,-1}^{\mathrm{c}} - v_{\mathrm{m}} k_{0,-1}^{\mathrm{c}} = (v_{\mathrm{av}}^+ - v_{\mathrm{m}}) \frac{v_{\mathrm{m}} + v_{\mathrm{av}}^-}{v_{\mathrm{av}}^+ + v_{\mathrm{av}}^-} k_{\mathrm{B}}, \tag{A.26a}$$

where the expressions for the bandgap centers of (3.65) in the paper were used. The incident frequencies aligned with the center of the bandgap, $\omega_{i_{\mathrm{g}}}$, are expressed as a function of $\omega_{\mathrm{e_g}}$ as

$$\omega_{i_{\mathrm{g}}} = \frac{v_{\mathrm{i}}}{v_{\mathrm{i}} - v_{\mathrm{m}}} \omega_{\mathrm{e_g}}. \tag{A.26b}$$

Similarly, in the superluminal case, $k_{\mathrm{e_g}}$ is found from Fig. A.4(b) as

$$k_{\mathrm{e_g}} = k_{0,-1}^{\mathrm{c}} - \frac{\omega_{0,-1}^{\mathrm{c}}}{v_{\mathrm{m}}} = \left(\frac{1}{v_{\mathrm{av}}^+} - \frac{1}{v_{\mathrm{m}}}\right) \frac{v_{\mathrm{av}}^+}{v_{\mathrm{m}}} \frac{v_{\mathrm{av}}^- + v_{\mathrm{m}}}{v_{\mathrm{av}}^- + v_{\mathrm{av}}^+} \omega_{\mathrm{B}}, \tag{A.27a}$$

where the bandgap center expressions of (3.67) in the paper were used for the second equality. The incident wavenumbers aligned with the center of the bandgap, $k_{i_{\mathrm{g}}}$, are expressed as a

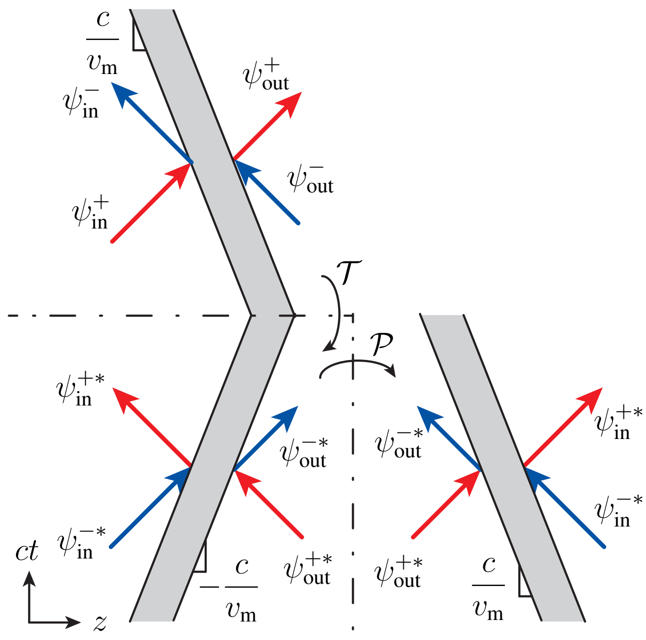

Figure A.3 Successive application of time reversal ($\mathcal{T}$) and space reversal ($\mathcal{P}$).

function of k_{e_g} as

$$k_{i_g} = \frac{v_m}{v_m - v_i} k_{e_g}. \tag{A.27b}$$

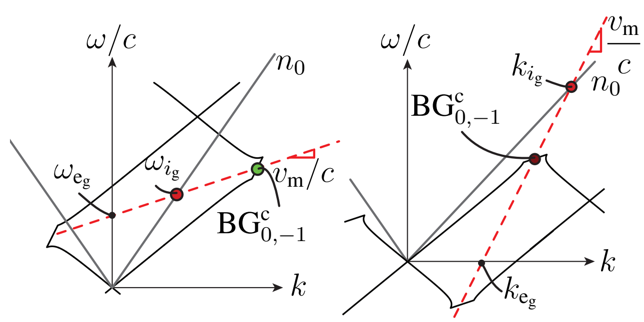

Figure A.4 Construction to find the frequencies aligned with the bandgaps. (a) Subluminal regime. (b) Superluminal regime

APPENDIX B APPENDIX FOR CHAPTER 4

B.1 Interface Matrix

The boundary conditions at an interface moving in the direction z at the velocity v, read, in the case of s-polarization [23],

$$E_{y1} - vB_{x1} = E_{y2} - vB_{x2}\big|_{z-vt=0}\,, \tag{B.1a}$$

$$H_{x1} - vD_{y1} = H_{x2} - vD_{y2}\big|_{z-vt=0}\,. \tag{B.1b}$$

Inserting forward (+) and backward (−) plane waves with the fields $E_{yn}^{\pm} = E_n^{\pm}$, $D_{yn}^{\pm} = \epsilon_n E_n^{\pm}$, $H_{xn}^{\pm} = B_{xn}^{\pm}/\mu_n$ and $cB_{xn}^{\pm} = \pm n_n E_n^{\pm}\cos\theta$ (with $n = 1, 2$) into these equations yields

$$\begin{aligned} &E_1^{+}(1-\beta n_1\cos\theta_1^{+}) + E_1^{-}(1+\beta n_1\cos\theta_1^{-}) \\ &\quad= E_2^{+}(1-\beta n_2\cos\theta_2^{+}) + E_2^{-}(1+\beta n_2\cos\theta_2^{-}), \end{aligned} \tag{B.2a}$$

$$\begin{aligned} &E_1^{+}(\cos\theta_1^{+}-\beta n_1)/\eta_1 - E_1^{-}(\cos\theta_1^{-}+\beta n_1)/\eta_1 \\ &\quad= E_2^{+}(\cos\theta_2^{+}-\beta n_2)/\eta_2 - E_2^{-}(\cos\theta_2^{-}+\beta n_2)/\eta_2, \end{aligned} \tag{B.2b}$$

where we used $n_n = c\sqrt{\epsilon_n\mu_n}$ and $\eta_n = \sqrt{\mu_n/\epsilon_n}$. More compactly, these equations read

$$\begin{bmatrix} f_1^{+} & f_1^{-} \\ g_1^{+} & -g_1^{-} \end{bmatrix} \begin{bmatrix} E_1^{+} \\ E_1^{-} \end{bmatrix} = \begin{bmatrix} f_2^{+} & f_2^{-} \\ g_2^{+} & -g_2^{-} \end{bmatrix} \begin{bmatrix} E_2^{+} \\ E_2^{-} \end{bmatrix}. \tag{B.3}$$

Isolating the column vector E_2 gives then Eqs. (4.6).

B.2 Empty-Lattice Approximation

The empty-lattice (or infinitesimal-perturbation) approximation is obtained by letting the refractive index and impedance contrast tend to zero, which corresponds to setting $A = 1$ in (4.12e). This transforms the spatial relation (4.15) into

$$\begin{aligned} \cos(k_z^{\pm}\ell \mp \Delta\phi^{\mathrm{s}}/2) &= \cos\frac{\Sigma\phi_i^{\mathrm{s}}}{2}\cos\frac{\Sigma\phi_j^{\mathrm{s}}}{2} - \sin\frac{\Sigma\phi_i^{\mathrm{s}}}{2}\sin\frac{\Sigma\phi_j^{\mathrm{s}}}{2} \\ &= \cos(\Sigma\phi_i^{\mathrm{s}}/2 + \Sigma\phi_j^{\mathrm{s}}/2) \end{aligned} \tag{B.4}$$

Setting the arguments of the first and last terms of this equation to be equal, isolating $k_z^{\pm}$ in the resulting relation, and substituting next (4.12d), yields

$$k_z^{\pm} = \left(\Sigma\phi_i^{\mathrm{s}} + \Sigma\phi_j^{\mathrm{s}} \pm \Delta\phi^{\mathrm{s}}\right)/(2\ell) = \left(k_{zi}^{\pm}\ell_i + k_{zj}^{\pm}\ell_j\right)/(2\ell). \tag{B.5}$$

Similarly, the temporal relation (4.18) transforms to

$$\omega^{\pm} = \left(\omega_i^{\pm} d_i + \omega_j^{\pm} d_j\right)/(2d). \tag{B.6}$$

Combining Eqs. (B.5) and (B.6) yields the empty-lattice approximation

$$\frac{n_{\mathrm{av}}^{\pm}}{c} = \left(\frac{k_{zi}^{\pm}\ell_i + k_{zj}^{\pm}\ell_j}{\omega_i^{\pm} d_i + \omega_j^{\pm} d_j}\right)\frac{d}{\ell}. \tag{B.7}$$

APPENDIX C APPENDIX FOR CHAPTER 5

C.1 Stability Calculation

This section derives the stability condition for the generalized FDTD scheme, presented in Sec. 5.4, using von Neumann's approach [152]. We will therefore replace everywhere the electromagnetic fields by their plane-wave test counterpart, $\Psi|_k^n = \Psi_0\zeta^n e^{ik_z k\Delta z}$, with $\zeta = e^{-\alpha\Delta t}$. In addition, we will use the convenient parameter $S = \Delta t/\Delta z$ wherever appropriate.

We shall restrict our derivations to the positive-velocity regime ($v > 0$), whose dynamic part corresponds to the first column of Tab. 5.1. The negative-velocity derivations ($v < 0$), whose dynamic part corresponds to the second column of Tab. 5.1, can easily be obtained upon following similar steps.

Using the plane-wave test field substitution in Eqs. (5.11a) and (5.12a), and dividing the resulting expression by ζ^n and $e^{ik_z k\Delta z}$ yields

$$B_{y0}e^{ik_z\Delta z/2} = B_{y0}e^{ik_z\Delta z/2}\zeta^{-1} - SE^*_{x0}\zeta^{-1/2}e^{ik_z\Delta z/2}\left(e^{ik_z\Delta z/2} - e^{-ik_z\Delta z/2}\right) - vSB_{y0}\zeta^{-1}\left(e^{ik_z\Delta z/2} - e^{-ik_z\Delta z/2}\right), \quad \text{(C.1)}$$

which may be alternatively written, upon multiplying by $\zeta e^{-ik_z\Delta z/2}$, forming sines, grouping terms and transferring everything to the left hand-side of the equality, as

$$E^*_{x0}\zeta^{1/2}2iS\sin(k_z\Delta z/2) + B_0\left(\zeta - 1 + ve^{-ik_z\Delta z/2}2iS\sin(k_z\Delta z/2)\right) = 0. \quad \text{(C.2)}$$

Similarly, Eq. (5.11b) with Eq. (5.13a) becomes

$$D_{x0}\zeta^{1/2} = D_{x0}\zeta^{-1/2} - SH^*_{y0}\left(e^{ik_z\Delta z/2} - e^{-ik_z\Delta z/2}\right) - vSD_{x0}\zeta^{-1/2}e^{-ik_z\Delta z/2}\left(e^{ik_z\Delta z/2} - e^{-ik_z\Delta z/2}\right), \quad \text{(C.3)}$$

or, multiplying by $\zeta^{1/2}$, and doing the same next operations as for the previous equation,

$$D_{x0}\left(\zeta - 1 + 2iSve^{-ik_z\Delta z/2}\sin(k_z\Delta z/2)\right) + H^*_{y0}\zeta^{1/2}2iS\sin(k_z\Delta z/2) = 0. \quad \text{(C.4)}$$

Next, Eq. (5.11c) with (5.14a) becomes, after factoring out $e^{-ik_z\Delta z}$ from the last two terms to form a cosine,

$$E^*_{x0}\zeta^{1/2} = D_{x0}\zeta^{1/2}/\epsilon - \frac{v}{2}B_{y0}e^{-ik_z\Delta z}(e^{ik_z\Delta z/2} + e^{-ik_z\Delta z/2}), \tag{C.5}$$

or, multiplying by $\epsilon\zeta^{-1/2}$, forming cosines, etc.,

$$D_{x0} - \epsilon E^*_{x0} - \epsilon v B_{y0}\zeta^{-1/2}e^{-ik_z\Delta z}\cos(k_z\Delta z/2) = 0. \tag{C.6}$$

Finally, Eq. (5.11d) with (5.15a) becomes, after factoring out $e^{-ik_z\Delta z/2}$ from the last terms to form a cosine,

$$H^*_{y0}e^{ik_z\Delta z/2} = B_{y0}e^{ik_z\Delta z/2}/\mu - \frac{v}{2}\zeta^{-1/2}e^{ik_z\Delta z/2}D_{x0}(e^{ik_z\Delta z/2} + e^{-ik_z\Delta z/2}), \tag{C.7}$$

or, multiplying by $-\mu e^{-ik_z\Delta z/2}$, etc.,

$$B_{y0} - \mu H^*_{y0} - \mu v\zeta^{-1/2}D_{x0}\cos(k_z\Delta z/2) = 0. \tag{C.8}$$

Equations (C.2), (C.4), (C.6) and (C.8) form a system of equations that can be put in the matrix form

$$\begin{bmatrix} A & 0 & 0 & B+vC \\ 0 & A & B+vC & 0 \\ -\epsilon & 0 & 1 & -\epsilon v D e^{-ik_z\Delta z} \\ 0 & -\mu & -\mu v D & 1 \end{bmatrix} \begin{bmatrix} E^*_{x0} \\ H^*_{y0} \\ D_{x0} \\ B_{y0} \end{bmatrix} = 0, \tag{C.9}$$

where

$$A = 2i\zeta^{1/2}S\sin(k_z\Delta z/2), \tag{C.10a}$$

$$B = \zeta - 1, \tag{C.10b}$$

$$C = 2iSe^{-ik_z\Delta z/2}\sin(k_z\Delta z/2), \tag{C.10c}$$

$$D = \zeta^{-1/2}\cos(k_z\Delta z/2). \tag{C.10d}$$

Setting the determinant of this homogeneous system to zero to find a nontrivial solution for ζ leads to the characteristic polynomial

$$\begin{aligned} &\zeta^2 + \frac{\zeta}{2n^2}\Big(4S^2 - n^2(4-3\beta S) - 4S(S+n^2\beta)\cos(k_z\Delta z)\Big) \\ &\quad + \frac{\zeta S\beta}{2}\left(\cos(2k_z\Delta z) + 2i\sin(k_z\Delta z) - i\sin(2k_z\Delta z)\right) \\ &\quad + e^{-ik_z\Delta z}[1 - S\beta(1-\cos(k_z\Delta z))][S\beta + (S\beta-1)\cos(k_z\Delta z) - i\sin(k_z\Delta z)] = 0. \end{aligned} \tag{C.11}$$

This is a polynominal of the second order in ζ whose solution is given by Eq. (5.15). The corresponding polynomial and solutions turn out to be exactly identical for the negative-velocity regime, although the related derivation involves distinct equations.

C.2 Analytical Solutions

This section provides analytical solutions that are used for validation of the illustrative examples given in Sec. 5.6. The solutions in Secs. C and C are closed-form solutions for the canonical problems of an interface and a slab, corresponding to Figs. 5.1(a) and 5.1(b), respectively, while the solutions in Sec. C are transfer-matrix method solutions for the more complex problems of a bilayer crystal and a gradient, corresponding to Figs. 5.1(c) 5.1(d), respectively.

C.2.1 General Formulas

In all cases, the incident field is a modulated Gaussian pulse, with temporal and spectral profiles

$$\psi_\mathrm{i}(t) = e^{-i\omega_\mathrm{i}t}e^{-(t/\tau_\mathrm{i})^2} \quad \text{and} \quad \tilde{\psi}_\mathrm{i}(\omega) = \frac{\tau_\mathrm{i}}{4\sqrt{\pi}}e^{\tau_\mathrm{i}^2(\omega-\omega_\mathrm{i})/4}, \tag{C.12}$$

where τ_i is the full-width at half-maximum duration divided by $2\sqrt{\ln 2}$ and ω_i is the modulation frequency. The spectra of the reflected and transmitted pulses are obtained as

$$\tilde{\psi}_\mathrm{t,r}(\omega) = \{T(a_\mathrm{t}\omega), \Gamma(a_\mathrm{r}\omega)\}\frac{\tau_\mathrm{i}}{4\sqrt{\pi}a_\mathrm{t,r}}e^{\tau_\mathrm{i}^2(\omega-a_\mathrm{t,r}\omega_\mathrm{i})^2/(4a_\mathrm{t,r})}, \tag{C.13}$$

where T and Γ are the transmission and reflection coefficients, and $a_\mathrm{t,r}$ are the transmission and reflection compression or expansion factors. This factors are given by

$$a_\mathrm{t} = \frac{1-n_\mathrm{in}v/c}{1-n_\mathrm{out}v/c} \quad \text{and} \quad a_\mathrm{r} = \frac{1-n_\mathrm{in}v/c}{1+n_\mathrm{in}v/c}, \tag{C.14}$$

where n_in is the refractive index of the medium in which the incident and reflected waves propagate, and n_out is the refractive index of the medium in which the transmitted wave propagates[1].

C.2.2 Interface

The scattering coefficients for a modulated interface are found by applying the continuity conditions (5.1a) and (5.1b). They read [3, 58, 97], assuming wave incidence from medium

[1] The equations (C.13) and (C.14) may be derived by combining results in [3,97] for monochromatic waves; they do not seem to have been published explicitely anywhere so far.

1 towards medium 2,

$$T_{21} = \frac{2\eta_2}{\eta_1+\eta_2}\frac{1-n_1v/c}{1-n_2v/c} \quad \text{and} \quad \Gamma_{121} = \frac{\eta_2-\eta_1}{\eta_1+\eta_2}\frac{1-n_1v/c}{1+n_1v/c}, \tag{C.15}$$

while the formulas for the reverse propagation direction are obtained by a simnple interchange of the subscripts. Note that the scattering coefficients here independent of the frequency.

C.2.3 Slab

The scattering coefficients for a modulated slab may be found, as for a stationnary slab, either by the multiple-reflection method or the boundary-value method [163]. This results in the scattering coefficients [3]

$$T = \frac{T_{21}T_{12}e^{-i\omega_2^+ n_2\ell}}{1-\Gamma_{212}\Gamma_{212}^- e^{-i(\omega_2^+ + \omega_2^-)n_2\ell}} \quad \text{and} \quad \Gamma = \Gamma_{121}\frac{1-e^{-i(\omega_2^+ + \omega_2^-)n_2\ell}}{1-\Gamma_{212}\Gamma_{212}^- e^{i(\omega_2^+ + \omega_2^-)n_2\ell}}. \tag{C.16}$$

These relations imply different frequencies for waves propagating forward (ω_2^+) and backward (ω_2^-), namely

$$\omega_2^+ = \frac{1-n_1v/c}{1-n_2v/c}\omega_\mathrm{i} \quad \text{and} \quad \omega_2^- = \frac{1-n_1v/c}{1+n_2v/c}\omega_\mathrm{i}, \tag{C.17}$$

where T_{21} and Γ_{121} are provided in Eq. (C.15), T_{12} and Γ_{121} are obtained by interchanging 1 and 2 in Eq. (C.15), and Γ_{212}^- is obtained by interchanging 1 and 2 and changing the sign of v in Γ_{121} (C.15).

C.2.4 Transfer-Matrix Method

The transfer-matrix method [3, 94, 106] allows to compute electromagnetic scattering for any traveling-wave modulation profile with uniform (space-time) slabs in the frequency domain[2]. This is even true for a smooth gradient modulation profile, which can be approximated as a succession of subwavelength interfaces with constant parameters.

The transfer-matrix method [3, 94, 106] models interfaces by the discontinuity matrix

$$I_{mn} = \frac{1}{t_{nm}^-}\begin{bmatrix} t_{mn}t_{nm}^- - \gamma_{mnm}\gamma_{nmn}^- & \gamma_{mnm}^- \\ -\gamma_{nmn} & 1 \end{bmatrix}, \tag{C.18}$$

[2]Note that, however, the uniform slab and frequency domain requirements of the transfer-matrix methods are very restrictive. The former requirement precludes the simulation of a space-time structures composed of slabs with *finite temporal durations* (and hence invovling space-time corners), which are obviously a basic constraint in practical scenarios. The latter requirement essentially precludes the determination of the spatio-temporal features of the scattered waves because this would imply an extremely complex set of Fourier transformations. In contrast, the proposed generalized FDTD scheme can straightforwardly simulate truncated slabs and exact space-time waveforms.

whose coefficients are given by

$$t_{mn} = \frac{2\eta_m}{\eta_m + \eta_n}\frac{1 - n_n v/c}{1 - n_m v/c} \quad \text{and} \quad \gamma_{nmn} = \frac{\eta_m - \eta_n}{\eta_m + \eta_n}\frac{1 - n_n v/c}{1 - n_n v/c} \tag{C.19}$$

and where the t_{mn}^- and γ_{nmn}^- coefficients are found by inverting the sign of v in (C.19) and the t_{nm} and γ_{nmn} coefficients are found by inverting m and n in (C.19). On the other hand, it models (space-time) slabs by the propagation matrix

$$P_m = \begin{bmatrix} e^{-i\omega_m^+ n_m \Delta z} & 0 \\ 0 & e^{i\omega_m^- n_m \Delta z} \end{bmatrix}, \tag{C.20}$$

where

$$\omega_\mathrm{m}^+ = \frac{1 - n_1 v/c}{1 - n_\mathrm{m} v/c}\omega_1^+, \quad \text{and} \quad \omega_\mathrm{m}^- = \frac{1 - n_1 v/c}{1 + n_m v/c}\omega_1^+ \tag{C.21}$$

are the frequencies of the forward- and backward-propagating waves within a given slab, and Δz is the width of this slab (which is constant under the assumption of uniform discretization).

The transfer matrix of a structure composed of N slabs is then found by taking the product of alternating discontinuity and propagation matrices, viz.,

$$[M]_{N1} = [I_{N,N-1}][P_{N-1}][I_{N-1,N-2}][P_{N-2}]...[P_2][I_{2,1}]. \tag{C.22}$$

Finally, the scattering coefficients can be obtained by converting the transfer matrix into a scattering matrix [117], which yields

$$T = \frac{AD - BC}{D}, \quad \Gamma = \frac{-A}{D}, \tag{C.23}$$

where A, B, C and D are the $(1,1)$, $(1,2)$, $(2,1)$ and $(2,2)$ components of the $[M]_{N1}$ matrix.

APPENDIX D CONFERENCE PROCEEDING: MOTION INDUCED TRANSFORMATION OF THE DISPERSION AND LOSS PROPERTIES OF AN ELECTROMAGNETIC MEDIUM

Motion Induced Transformation of the Dispersion and Loss Properties of an Electromagnetic Medium

Zoé-Lise Deck-Léger and Christophe Caloz

Presented in URSI General Assembly and Scientific Symposium (GASS), Rome, Italy, Sep. 2021, pp. 1–3.

We investigate how the dispersion and loss properties of a medium are altered when the medium is set into motion. Dispersive moving media is shown to give rise to unidirectional propagation in certain frequency ranges. Lossy moving media is shown to be maximally lossy for contra-directional propagation, at the velocity where the real part of the refractive index crosses zero. This work will serve to develop emerging spacetime metamaterials.

D.1 Introduction

Bulk moving media have been abundantly studied since the pioneering works of Fizeau [6] and Minkowski [11]. They have different upstream and downstream velocities, an effect called the Fizeau drag, and are hence nonreciprocal. Moreover, they exhibit a velocity-dependent bianisotropic response that may be radically different from their rest response [56] and exhibit a negative index of refraction at high velocities [19].

Moving dispersive media were first studied by Lorentz, who extended the Fizeau drag formula to include dispersion [63]. His theory was verified experimentally by Zeeman [14]. There were many works modelling moving plasmas in waveguides, including dispersion and loss, in the 1960s [164–166]. More recently, Leonhardt and Piwnicki showed that a dispersive moving medium mimicks a gravitational field [167].

In this work, we first briefly review the Fizeau drag for nondispersive and lossless moving media. We then derive the laboratory-frame dispersion relation of a dispersive moving medium and show that within some frequency range, all the solutions must propagate downstream. We finally calculate the refractive index of a lossy medium as a function of velocity, without any approximation, and find that for co-directional propagation loss decreases, while for contra-directional propagation loss is enhanced, in particular in a specific velocity range.

D.2 Lossless Nondispersive Medium

We start by calculating the refractive index of lossless and nondispersive moving media in the laboratory frame. We will limit ourselves throughout the paper to one-dimensional propagation, with the wave propagating in a direction parallel to the motion of the medium.

The velocity of a wave propagating in a moving medium, v_w, is not the sum of the moving media velocity, v, and the wave velocity in the stationnary medium, v'_w, as suggested by Fizeau [6], but rather reads

$$v_\mathrm{w} = \frac{v'_\mathrm{w} + v}{1 + v'_\mathrm{w} v/c^2}. \tag{D.1}$$

Equation (D.1) is the relativistic velocity addition rule, which is typically derived in the direct space (z, ct) by substituting the Lorentz transformations $z = \gamma(z' + vt')$ and $t = \gamma(t' + v/c^2 z')$, where $\gamma = (1 - v^2/c^2)^{-1/2}$, into the expression of velocity $v_\mathrm{w} = dz/dt$. Here, we rather derive this formula in the inverse space (k, ω/c), so as to avoid the derivative and introduce the methodology for the next sections.

The dispersion relation in the moving frame, where the medium appears stationary, reads

$$k' = \omega' \frac{n'}{c}. \tag{D.2}$$

To transform this relation into the laboratory frame, we use the frequency Lorentz transformations [69]

$$\omega' = \gamma\left(\omega - vk\right), \qquad k' = \gamma\left(k - \frac{v}{c^2}\omega\right). \tag{D.3}$$

Inserting (D.3) into (D.2), we obtain

$$k - \frac{v}{c^2}\omega = \left(\omega - vk\right)\frac{n'}{c}, \tag{D.4}$$

whose resolution for k provides

$$k = \omega\left(\frac{v/c^2 + n'/c}{1 + vn'/c}\right) = \omega\frac{n}{c}. \tag{D.5}$$

Substituting $v_w = c/n$ and $v'_w = c/n'$ into (D.5) and solving for v_w indeed retrieves the relativistic velocity addition (D.1).

D.3 Addition of Temporal Dispersion

We now investigate the effect of velocity on the temporal dispersion. We assume the medium in the moving frame has a Lorentz lossless dispersion, i.e.,

$$n'(\omega') = 1 + \frac{{\omega'_p}^2}{{\omega'_0}^2 - \omega'^2}, \tag{D.6}$$

with ω'_p, ω'_0, the plasma frequency and the resonance frequency. Inserting the frequency Lorentz transformation (D.3) into (D.6), we obtain a dispersion relation in terms of the frequency and wavenumber,

$$n(\omega - vk) = 1 + \frac{{\omega'_p}^2}{{\omega'_0}^2 - \gamma^2 (\omega - vk)^2}. \tag{D.7}$$

Substituting this relation into the dispersion relation (D.2), we obtain the following cubic relation

$$\alpha_3 k^3 + \alpha_2 k^2 + \alpha_1 k + \alpha_0 = 0, \tag{D.8a}$$

with

$$\alpha_3 = -\gamma^2 v^2 (c + v), \tag{D.8b}$$

$$\alpha_2 = \gamma^2 v\omega \left(2c + 3v + v^2/c\right), \tag{D.8c}$$

$$\alpha_1 = v\left({\omega'_0}^2 + {\omega'_p}^2\right) + c{\omega'_0}^2 - \gamma^2\omega^2 \left(2v^2/c - 3v - c\right), \tag{D.8d}$$

$$\alpha_0 = -\omega\left({\omega'_0}^2 + {\omega'_p}^2\right) - v\omega{\omega'_0}^2/c + \gamma^2\omega^3 (1 + v/c). \tag{D.8e}$$

Figure D.1 presents the dispersion diagram of the Lorentz medium. In Fig. D.1(a), the diagram is plotted in the moving frame, where we have the usual Lorentz dispersion relation. In Fig. D.1(b), the diagram is plotted in the laboratory frame, using (D.8). In this laboratory frame, six solutions exist at every frequency, while in the moving frame only two solutions exist at each frequency. Also, in the laboratory frame there are some frequencies where all the solutions have a positive wavenumber k (one such situation is highlighted in Fig. D.1(b)), meaning that at these frequencies, all the waves propagate downstream, with different velocities.

D.4 Addition of Loss

We now calculate the refractive index of a moving nondispersive lossy medium.

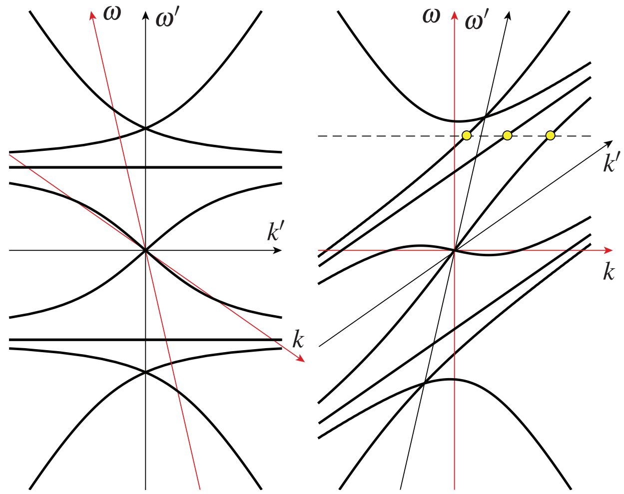

Figure D.1 Dispersion diagram for a Lorentz-dispersive lossless medium. (a) As seen in the moving frame [Eq. D.6]. (b) As seen in the laboratory frame [Eq. D.8]. There are overall six solutions (the three in the continuation of the bottom curves would appear farther at the right of the graph and are not shown here), and these solutions have all a positive wavenumber in some frequency range.

The dispersion relation (D.2) now consists of a complex refractive index, complex wavenumbers and complex frequencies. We apply the Lorentz transformations (D.7) to the dispersion relation (D.2), and write explicitly the real and imaginary parts of each component. This leads to

$$k_r + ik_i - \frac{v}{c^2}(\omega_r + i\omega_i) = \left(\omega_r + i\omega_i - v(k_r + ik_i)\right)(n_r + in_i)/c. \tag{D.9}$$

We separate this equation into real and imaginary parts, and obtain

$$k_r - \frac{v}{c^2}\omega_r = (\omega_r - vk_r)\frac{n_r}{c} - (\omega_i - vk_i)\frac{n_i}{c}, \tag{D.10a}$$

$$k_i - \frac{v}{c^2}\omega_i = (\omega_r - vk_r)\frac{n_i}{c} + (\omega_i - vk_i)\frac{n_r}{c}. \tag{D.10b}$$

To plot the $(\omega,\, k_r)$ and $(\omega,\, k_i)$ curves, we set $\omega_i = 0$. Note that setting $\omega_i' = 0$ in the moving frame, which corresponds to $\omega_i - vk_i = 0$ in the laboratory frame, would yield the incorrect result that $\omega_i \neq 0$ for $k_i \neq 0$.

We solve the system of equations for k_r and k_i, and find

$$k_r = \frac{\omega_r}{c}\frac{(1 + vn_r'/c)(n_r' + v/c) + vn_i'^2/c}{(1 + vn_r'/c)^2 + v^2 n_i'^2/c^2} = \frac{\omega_r}{c}n_r \tag{D.11a}$$

$$k_i = \frac{\omega_r}{c} \frac{n_i' \left(1 - v^2/c^2\right)}{(1 + v n_r'/c)^2 + v^2 {n_i'}^2/c^2} = \frac{\omega_r}{c} n_i, \tag{D.11b}$$

with (D.11a) reducing to (D.5) for $n_i = 0$, as expected.

The refractive indices in (D.11) are plotted in Fig. D.2. For positive velocities, corresponding to co-directional propagation, both the real and imaginary parts of the refractive index decrease gradually, so that the wave's velocity increases and loss decreases. At the limit $v/c = 1$, the medium acts like free space. For contra-directional propagation, loss is highly amplified, with maximal amplification occuring when the real part of the refractive index changes sign. For lossless media, this would occur at $v = -c/n$.

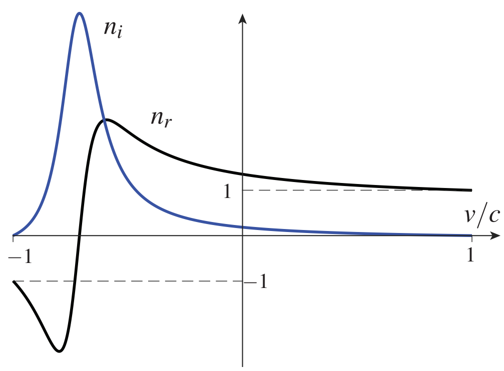

Figure D.2 Refractive index as a function of velocity for a dispersionless lossy moving medium.

D.5 Conclusions

We have addressed the one-dimensional problems of a dispersive moving medium and a lossy moving medium. We found that perfect isolation occurs for certain frequencies in a moving dispersive medium. We also found that loss is maximally amplified near the velocity $v = -c/n$.

This work may help develop emerging spacetime metamaterials [96, 97]

APPENDIX E CONFERENCE PROCEEDING: SCATTERING AT INTERLUMINAL INTERFACE

Scattering at Interluminal Interface

Zoé-Lise Deck-Léger and Christophe Caloz

in IEEE AP-S Int. Antennas Propag., Atlanta, GA, Jul. 2019, pp. 367–368.

Interest for spacetime structures has recently been revived, following developments in metamaterials and ultrafast optics. Such structures essentially consist of successions of space-time interfaces for which the theory is still incomplete, in particular in the regime where the interface velocity lies between the wave velocities in the two media involved. This paper addresses this "interluminal" regime, providing exact scattering solutions for both approaching and receding interfaces. The solutions are verified to be consistent with the transmission matrix perspective and to be continuous at the limits of the subluminal and superluminal regimes.

E.1 Introduction

Spacetime structures, which are characterized by medium parameters that vary in both space and time, possess many interesting and useful properties: they are intrinsically nonreciprocal, due to their time-reversal asymmetry, induce spatial and temporal frequency transformations, provide amplification or attenuation, and support exotic phenomena such as time reversal and anomalous deflections. Combined with recent advances in metamaterial and fabrication technologies, these properties have recently revived the interest in such media.

Medium interfaces constitute the building blocks of spacetime composite structures. The scattering coefficients and frequency transitions occurring at such interfaces are easily found from field continuity conditions, except in the regime where the interface speed is between the wave speeds in the two involved media. No complete exact solution has ever been reported in this "interluminal" regime.

This regime was first identified as problematic in the study of space-time periodic structures in 1963 [37], where it was called the "sonic" regime. Later, the problem of an interface approaching incident light from an electromagnetic rarer medium to an electromagnetic denser medium was solved in [34,43]. This problem was investigated using the finite-difference technique in [106] and an ingenious space-time discretization provided a solution for acoustic waves in [109].

This paper first revisits the solution of [34], and then solves the problem of a receding interface, which was not treated before. The solution is shown to be consistent with the general transfer matrix perspective presented in [106], and to exhibit proper continuity at the limits of the velocity range.

E.2 Interluminal Problems

The interluminal regime corresponds to the velocity range

$$v_2 < |v_\mathrm{m}| < v_1, \tag{E.1}$$

where v_m is the velocity of the interface and $v_{1,2} = c/n_{1,2}$ are the speeds of light in media 1 and 2. Here we shall consider, for simplicity, the case $n_1 < n_2$, with $n_1, n_2 \geq 1$.

Figures 1(a) and (c) present the space-time diagrams of an approaching ($v < 0$) and a receding ($v > 0$) interface of interluminal velocity. A wave incident on the approaching interface generates three scattered waves, while a single scattered wave is produced by three waves incident on the receding interface. These problems are under- and over-determined, respectively, since they involve three and one unknowns, for two continuity conditions [43].

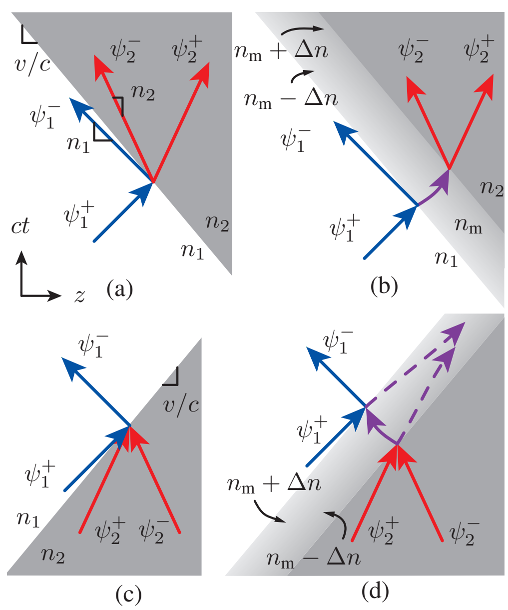

Figure E.1 Scattering from an interluminal interface. (a) Original problem of approaching ($v < 0$) interface. (b) Auxiliary approaching proble.(c) Original problem of receding ($v > 0$) interface. (b) Auxiliary receding problem.

We solve these problems using the auxiliary problems in Fig. 1(b) and Fig. 1(d). In essence, the auxiliary problems avoid the aforementioned indeterminacies by adding a gradient slab at the interfaces. This transforms the problems into successions of purely subluminal and superluminal interfaces, for which analytical solutions are known: the transmission and reflection coefficients for a subluminal ($|v_\mathrm{m}| < v_j$) interface between media i and j are

$$\tau_{ji} = \frac{A_j^+}{A_i^+} = \frac{2n_i}{n_i + n_j}\left(\frac{1 - n_i v_\mathrm{m}/c}{1 - n_j v_\mathrm{m}/c}\right), \tag{E.2a}$$

$$\gamma_{ii}^{i\to j} = \frac{A_i^-}{A_i^+} = \frac{n_i - n_j}{n_i + n_j}\left(\frac{1 - n_i v_\mathrm{m}/c}{1 + n_i v_\mathrm{m}/c}\right), \tag{E.2b}$$

while for the superluminal ($|v_\mathrm{m}| > c/n_i$) case, they are [34]

$$\xi_{ji} = \frac{A_j^+}{A_i^+} = \frac{n_i + n_j}{2n_j}\left(\frac{1 - n_i v_\mathrm{m}/c}{1 - n_j v_\mathrm{m}/c}\right), \tag{E.3a}$$

$$\zeta_{ji} = \frac{A_j^-}{A_i^+} = -\frac{n_i - n_j}{2n_j}\left(\frac{1 - n_i v_\mathrm{m}/c}{1 + n_j v_\mathrm{m}/c}\right), \tag{E.3b}$$

where the reflective superscript $i \to j$ denotes incidence from i towards j.

E.3 Scattering from Approaching Interface

Consider the auxiliary problem of the approaching interface, shown in Fig. E.1(b). The intermediate gradient medium has an average index $n_\mathrm{m} = c/|v_\mathrm{m}|$, varying from $n_\mathrm{m} - \Delta n$ to $n_\mathrm{m} + \Delta n$. The first interface is subluminal, since $|v_\mathrm{m}| < c/(n_\mathrm{m} - \Delta n)$, while the second interface is superluminal, since $|v_\mathrm{m}| > c/(n_\mathrm{m} + \Delta n)$. The total scattering coefficients are obtained by multiplying the coefficients of the first and second interfaces, then letting $\Delta n \to 0$, and finally inserting $v_\mathrm{m}/c = -1/n_\mathrm{m}$, which yields

$$\alpha_{11}^{1\to 2} = \frac{\psi_1^-}{\psi_1^+} = \gamma_{11}^{1\to \mathrm{m}} = -1, \tag{E.4a}$$

$$\beta_{21} = \frac{\psi_2^-}{\psi_1^+} = \zeta_{2\mathrm{m}}\tau_{\mathrm{m}1} = -\frac{n_1}{n_2}, \tag{E.4b}$$

$$\kappa_{21} = \frac{\psi_2^+}{\psi_1^+} = \xi_{2\mathrm{m}}\tau_{\mathrm{m}1} = \frac{n_1}{n_2}. \tag{E.4c}$$

Surprisingly, these coefficients are independent of velocity.

E.4 Scattering from Receding Interface

Consider now the receding-interface auxiliary problem, shown in Fig. 1(c). There can be up to three incident waves, but only one wave can be scattered. Adding the same transition medium as previously, we have again a succession of subluminal and superluminal problems. Using the same procedure as above, we obtain

$$\alpha_{11}^{1\to 2} = \frac{\psi_1^-}{\psi_1^+} = \gamma_{11}^{1\to \mathrm{m}} = -\left(\frac{1 - v_\mathrm{m} n_1/c}{1 + v_\mathrm{m} n_1/c}\right)^2 , \tag{E.5a}$$

$$\beta_{12} = \frac{\psi_1^-}{\psi_2^+} = \bar{\tau}_{1\mathrm{m}} \zeta_{\mathrm{m}2} = \left(\frac{1 - v_\mathrm{m} n_2/c}{1 + v_\mathrm{m} n_1/c}\right)^2 , \tag{E.5b}$$

$$\kappa_{12} = \frac{\psi_1^-}{\psi_2^-} = \bar{\tau}_{1\mathrm{m}} \bar{\xi}_{\mathrm{m}2} = \left(\frac{1 + v_\mathrm{m} n_2/c}{1 + v_\mathrm{m} n_1/c}\right)^2 , \tag{E.5c}$$

where $\bar{\tau} = \tau(-v_\mathrm{m})$ and $\bar{\xi} = \xi(-v_\mathrm{m})$. Note the two purple dashed lines never escape from the transition region, and therefore do not enter into the calculation of the coefficients.

E.5 Verification

We now check whether our results are consistent with the transfer matrix of a spatiotemporal interface [106], which relates the fields on both sides of the interface:

$$\begin{bmatrix} \psi_i^+ \\ \psi_i^- \end{bmatrix} = \begin{bmatrix} \dfrac{n_j + n_i}{2n_i} \dfrac{1 + n_j v_\mathrm{m}}{1 + n_i v_\mathrm{m}} & \dfrac{n_j - n_i}{2n_i} \dfrac{1 - n_j v_\mathrm{m}}{1 + n_i v_\mathrm{m}} \\ \dfrac{n_j - n_i}{2n_i} \dfrac{1 + n_j v_\mathrm{m}}{1 - n_i v_\mathrm{m}} & \dfrac{n_j + n_i}{2n_i} \dfrac{1 - n_j v_\mathrm{m}}{1 - n_i v_\mathrm{m}} \end{bmatrix} \begin{bmatrix} \psi_j^+ \\ \psi_j^- \end{bmatrix} . \tag{E.6}$$

Reading out the field relationship from Fig. 1(c) and replacing the fields in medium 1 using (E.6) yields

$$\begin{aligned} \kappa_{12}\psi_2^+ + \beta_{12}\psi_2^- &= \psi_1^- - \alpha_{11}^{1\to 2}\psi_1^+ \\ &= \left(t_{12}^{21} - \alpha_{11}^{1\to 2} t_{12}^{11}\right)\psi_2^+ + \left(t_{12}^{22} - \alpha_{11}^{1\to 2} t_{12}^{12}\right)\psi_2^- , \end{aligned} \tag{E.7}$$

where t_{12}^{nm} corresponds to the transfer matrix element of the n^{th} row and m^{th} column. We find our results are consistent with this transfer matrix, since inserting $\alpha_{11}^{1\to 2}$ (E.5a) and the transfer matrix elements of (E.6) into the right side of (E.7) retrieves the coefficients κ_{12} (E.5b) and β_{12} (E.5c).

To further verify our results, the scattering coefficients are plotted in Fig. E.2 across the entire velocity range. It is comforting to see the parameters exhibit no discontinuity at the different regime limits.

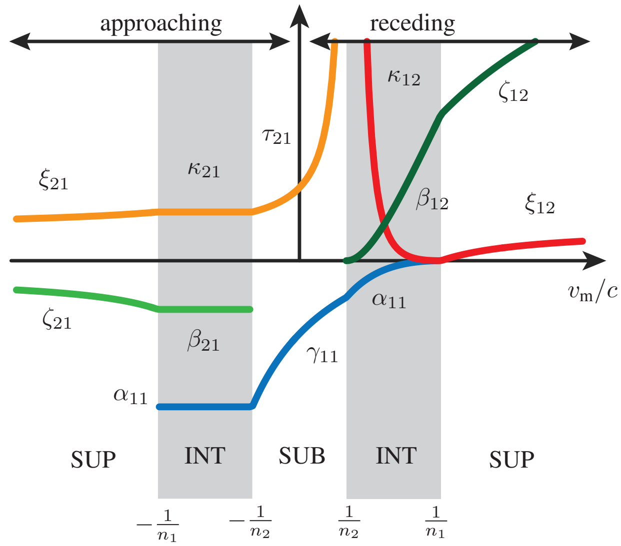

Figure E.2 Scattering coefficients [Eqs. (E.2), (E.3), (E.4) and (E.5)] across the entire velocity range, which includes the approaching and receding subluminal (SUB), interluminal (INT) and superluminal (SUP) regimes.